Conditional Moment Closure for Non-Premixed Turbulent Combustion

by

IK SOO KIM

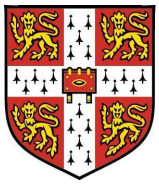

A dissertation submitted to the

University of Cambridge for the degree of

Doctor of Philosophy

22nd December 2004

St. Edmund's college

Declaration

This dissertation is the result of my own work and includes nothing which is the outcome of work done in collaboration except where specifically indicated in the text. No part of this dissertation has already been, or is being concurrently submitted for any other degree, diploma or qualification.

This dissertation contain approximately 29,200 words and 80 figures.

.....

IK SOO KIM

22nd December 2004

Dedicated to my parents, Young Dal Kim and Chun Hee Kim,

to my wife, Eun Ha Kang.

Preface

The research described in this thesis was performed form October 2001 to December 2004 and has been supervised by Dr. Epaminondas Mastorakos. He deserves my sincerest thanks for his warm interest, useful suggestions, and constructive criticisms on the work and on this thesis, and for his efforts to obtain the financial support that made my stay at the University of Cambridge. My gratitude is deeper than I express for Dr. Epaminondas Mastorakos's long effort to teach me how scientific research should be done. It needs a lot of work from my part, but I must try to ensure that his efforts were not wasted.

Friends in the lab, I would like to thank for sharing useful information and encouraging me, A. Meacock, C. Markides, B. Haberman, E. Richardson, G. De Paola, S-W. Park and C-W. Lee.

On a personal level, I must thank my family including my wife's family for their support. I would not have made this work without them.

Abstract

The simulation of non-premixed turbulent combustion is challenging and the numerical understanding of turbulent combustion has not yet been fully developed. One of the advanced computational models for turbulent combustion, the Conditional Moment Closure (CMC), is tested on various problems such as an attached jet flame, lifted jet flames and opposed jet flames.

Validation of sub-models in CMC by comparison with DNS shows that the beta PDF for the mixture fraction and the linear model for the conditional velocity are the most accurate compared with the DNS. The Girimaji model for the conditional scalar dissipation rate gives better predictions in homogeneous mixtures and the AMC model is better in inhomogeneous mixtures when used with the beta PDF. The Gradient diffusion model for conditional fluxes provides good agreement in inhomogeneous cases, but not in homogenous.

A stiff/nonstiff solver that can solve large systems of ODE's, VODPK, allows transformation of the PDE's into a set of ODE's. The VODPK solver is used to avoid the splitting errors between physical and mixture fraction spaces. Various discretisation methods of the CMC equations in physical space are examined. The Upwind scheme (UDS) gives large numerical diffusion, while the Central difference scheme (CDS) gives small numerical diffusion, but unrealistic oscillations also occur. The CMC equations are not

solved if the mixture fraction PDF is below a certain value and the conditional scalar dissipation is set to zero at these conditions. Two methods of interfacing between the CFD grid and the CMC grid, one using values from the exact physical location of the CMC grid node and another by integrating over a group of CFD nodes after weighting by the mixture fraction PDF, give very similar results.

The CFD package 'FLUENT' is used to provide the flow field, especially the mixture fraction and its fluctuations, however some standard model constants should be changed to capture accurately the flow field as compared with experiments. The modified model constants are mainly the Schmidt number Sc, the unconditional scalar dissipation rate constant C_D and the turbulent dissipation rate constant $C_{\varepsilon 2}$ that appear in various equations in the $k-\varepsilon$ and the Reynolds stress models.

The results in flames with existence of local extinction showed that the first order CMC should not be used where conditional fluctuations of scalars are large, as expected. Significant variations of the conditional averages across the jet are found and hence a higher dimensional CMC should be used. The first order two-dimensional CMC provides good agreement with experiment in turbulent lifted hydrogen flame. The flame stabilises at a height where the scalar dissipation rate is well below the quenching value, consistent with experimental data. Further analysis of the CMC temperature equation is made and we conclude that the spatial transport terms play a major role in stabilisation. The hysteresis behaviour of turbulent lifted flames is also observed. The extinction limit in the turbulent counterflow flame is mainly controlled by the magnitude of the scalar dissipation rate and the

spatial transport terms are small, except near the extinction velocity. The region over which the conditional scalar dissipation rate equals the quenching value increases in size while extinction is approached. During this event, the spatial transport term becomes important. The extinction velocity is found to be much higher than the experimental value, but the trend of increasing extinction velocity with air dilution of the fuel stream is captured very well.

Contents

List of Figures

List of Tables

Chapter 1

Introduction

Combustion is known as a reaction between fuel and oxidizer to generate heat and power which provide us with a more convenient life such as a moving vehicle, boilers and electricity. However, pollutant by combustion is a major environmental problem that directly relates to health hazards. Therefore, understanding of turbulent flames is needed to decrease pollution and this is a real challenge. Computer simulations are now a truly important research tool to support the theory of combustion and understand phenomena from experiments. It is hoped that theory, experiment and simulation can allow a better control and understanding of combustion.

This thesis deals with a mathematical model and an associated computational code for non-premixed combustion, a very common type of flame that occurs in diesel engines, industrial furnaces and other applications.

1.1 Objectives

In this thesis, the Conditional Moment Closure (CMC) for non-premixed turbulent combustion is explored in depth and the first order CMC is examined in applications such as an attached turbulent jet flame with localised extinction, lifted turbulent jets and turbulent counterflow flames. This work emphasizes flame stabilisation mechanisms, flame extinction and the limitations of using first order CMC, topics that have not been studied enough with CMC up to now. A detailed review of previous work on these topics will be given in later Chapters.

Many sub-models of the CMC equations have been provided in the literature, but have not yet been fully validated. Hence, comparisons with DNS data in homogeneous and inhomogeneous mixtures is used to find out which of these sub-models applies in different applications. The problems of numerical implementation of the CMC equations are also examined.

An application of the attached turbulent flame stabilized by a pilot, where local extinction exists with large conditional fluctuations provides the limit of the first order CMC. Stabilisation mechanisms are supported and explored in the turbulent lifted flame and good agreement with experiment is found. The analysis of CMC equation terms offers the numerical understanding of the stabilisation mechanisms at the flame base. Extinction phenomena by excess of conditional scalar dissipation rate are obtained in the turbulent counterflow flames. The trend of the extinction by the first order CMC are examined.

1.2 Overview

This Chapter provides a review of the governing equations and some common strategies for turbulent combustion modelling, which puts CMC in context.

In Chapter 2, the derivation of the Conditional Moment Closure, sub-models validations with DNS data, and the numerical implementation of the CMC equations are presented.

In Chapter 3, an attached piloted natural gas jet diffusion flame is examined and the discrepancies between the first order CMC and experiments due to local extinction are revealed. However, the overall reasonable structure captured suggests that the implementation of CMC code is free of programming errors.

Flame stabilisation mechanisms are studied in Chapter 4 for turbulent hydrogen lifted jet flames by analysing the role of the CMC equations, which provides an improved understanding.

In Chapter 5, turbulent counterflow flames are used to study flame extinction by excess of the conditional scalar dissipation rate. The first order CMC gives the right trend of the extinction limits although accurate sub-models are needed for the conditional scalar dissipation rate.

Finally, the work is summarised in Chapter 6 and proposals for future work are given.

1.3 Balance equations

In this section, the fundamental knowledge for turbulent diffusion flames is summarised and reviewed. The basic equations and properties of turbulent flow will be visited firstly to derive the modelling strategies and the turbulence and combustion interaction will be followed.

In the following, the classical Navier-Stokes, species and energy transport equations will be presented following Turns (2000), Pope (2000), Tennekes and Lumley (1972), Peters (2000) and Williams (1985).

1.3.1 Instantaneous balance equations

1.3.1.1 Mass

$$\frac{\partial \rho}{\partial t} + \frac{\partial (\rho u_j)}{\partial x_j} = 0 \tag{1.1}$$

1.3.1.2 Momentum

$$\frac{\partial (\rho u_i)}{\partial t} + \frac{\partial (\rho u_i u_j)}{\partial x_j} = -\frac{\partial p}{\partial x_i} + \frac{\partial \tau_{ij}}{\partial x_j} + F_i \tag{1.2}$$

where τ_{ij} is the viscous force tensor and F_i represents a body force in the i-th coordinate direction. In practical situations of combustion, all fluids are assumed to be Newtonian and the viscous stress tensor is:

$$\tau_{ij} = \mu \left(\frac{\partial u_i}{\partial x_j} + \frac{\partial u_j}{\partial x_i} \right) - \frac{2}{3} \mu \delta_{ij} \left(\frac{\partial u_k}{\partial x_k} \right) \tag{1.3}$$

where μ is the molecular viscosity which depends on the fluid. The Kronecker

delta is δ_{ij}=1 if $i = j$, 0 otherwise.

1.3.1.3 Species

$$\frac{\partial(\rho Y_\alpha)}{\partial t} + \frac{\partial(\rho u_j Y_\alpha)}{\partial x_j} = -\frac{\partial \mathcal{J}_j^\alpha}{\partial x_j} + \omega_\alpha \qquad (\alpha = 1, 2, ..., n) \tag{1.4}$$

where n is the number of species, $\mathcal{J}_j^\alpha$ is the molecular diffusive flux of the species α in the j-th coordinate direction, ω_α is the mass reaction rate of this species per unit volume, and Y_α is the mass fraction of species α.

The diffusive flux, $\mathcal{J}_j^\alpha$, can be approximated by:

$$\mathcal{J}_j^\alpha = -\frac{\mu}{Sc_\alpha}\frac{\partial Y_\alpha}{\partial x_j} = -\rho \mathcal{D}_\alpha \frac{\partial Y_\alpha}{\partial x_j} \tag{1.5}$$

where Sc_α is the Schmidt number of the species α, defined as:

$$Sc_\alpha = \frac{\mu}{\rho \mathcal{D}_\alpha} \tag{1.6}$$

where $\mathcal{D}_\alpha$ is the molecular diffusivity of the species α relative to other species. For simplicity, all mass diffusivities, $\mathcal{D}$, are assumed to be proportional to the thermal diffusivity and the Lewis numbers, Le, are constant:

$$\mathcal{D} = \frac{\lambda}{\rho c_p}\,, \qquad Le_\alpha = \frac{\lambda}{\rho c_p \mathcal{D}_\alpha} = \frac{\mathcal{D}}{\mathcal{D}_\alpha} \tag{1.7}$$

In these equations λ is the thermal conductivity and c_p is the heat capacity at constant pressure of the mixture.

If there are n possible species in the system of chemical reactions, then

the i-th chemical reaction is:

$$\sum_{\alpha=1}^{n} \nu'_{\alpha i} X_\alpha \underset{\kappa_{bi}}{\overset{\kappa_{fi}}{\rightleftarrows}} \sum_{\alpha=1}^{n} \nu''_{\alpha i} X_\alpha \tag{1.8}$$

where X_α is the chemical symbol for species α and $\nu'_{\alpha i}$ and $\nu''_{\alpha i}$ are the stoichiometric coefficients on the reactants and products side of the reaction. The chemical source term ω_α, which is the mass of species α produced per unit volume and unit time is:

$$\omega_\alpha = MW_\alpha \sum_{i=1}^{l} \nu_{\alpha i} q_i \tag{1.9}$$

with the rate of reaction q_i in a chemical mechanism containing l chemical reactions:

$$q_i = \kappa_{fi} \prod_{\alpha=1}^{n} \left(\frac{\rho Y_\alpha}{MW_\alpha} \right)^{\nu'_{\alpha i}} - \kappa_{bi} \prod_{\alpha=1}^{n} \left(\frac{\rho Y_\alpha}{MW_\alpha} \right)^{\nu''_{\alpha i}} \tag{1.10}$$

where MW_α is the molecular weight of species α and $\nu_{\alpha i} = \nu''_{\alpha i} - \nu'_{\alpha i}$. The Arrhenius rate κ is $\kappa = A_0 T^\beta \exp(-E_a/RT)$ where A_0 represents the frequency factor, β is the temperature exponents, and E_a is the activation energy. The subscript fi and bi represent forward and backward direction of i-th chemical reaction respectively.

1.3.1.4 Energy

In a mixture, the enthalpy h is the mass-weighted sum of the specific enthalpies h_α :

$$h = \sum_{\alpha=1}^{n} Y_\alpha h_\alpha \tag{1.11}$$

and the same applies for the mixture specific heat capacity :

$$c_p = \sum_{\alpha=1}^{n} Y_\alpha (c_p)_\alpha \tag{1.12}$$

The absolute enthalpy of an ideal gas h_α depends on the temperature through:

$$h_\alpha = (h_0)_\alpha + \int_{T_0}^{T} (c_p)_\alpha dT \tag{1.13}$$

The enthalpy balance equation is:

$$\frac{\partial(\rho h)}{\partial t} + \frac{\partial(\rho u_j h)}{\partial x_j} = \frac{\partial p}{\partial t} + \frac{\partial(u_j p)}{\partial x_j} - \frac{\partial \mathcal{J}_j^h}{\partial x_j} + \frac{\partial(u_i \tau_{ij})}{\partial x_j} + u_j F_j + q_{RAD} \tag{1.14}$$

$u_i \tau_{ij}$ and $u_j F_j$ are the rate of work done by the viscous force and the body force respectively. The local pressure gradient can be neglected in the low Mach number, but is important for acoustic interactions and pressure waves. q_{RAD} represents heat transfer due to radiation. The enthalpy diffusion flux $\mathcal{J}_j^h$ can be defined as:

$$\begin{aligned} \mathcal{J}_j^h &= -\lambda \frac{\partial T}{\partial x_j} + \sum_{\alpha=1}^{n} h_\alpha \mathcal{J}_j^\alpha \\ &= -\frac{\mu}{Pr} \left[\frac{\partial h}{\partial x_j} + \sum_{\alpha=1}^{n} \left(\frac{Pr}{Sc_\alpha} - 1 \right) h_\alpha \frac{\partial Y_\alpha}{\partial x_j} \right] \\ \text{with} \qquad dh &= c_p dT + \sum_{\alpha=1}^{n} h_\alpha dY_\alpha \end{aligned} \tag{1.15}$$

Here Pr is Prandtl number and the Lewis numbers Le (Eq. 1.7):

$$Pr = \left(\frac{\mu c_p}{\lambda} \right) \quad \text{and} \quad Le_\alpha = \left(\frac{Sc_\alpha}{Pr} \right) = \left(\frac{\lambda}{\rho c_p \mathcal{D}_\alpha} \right) \tag{1.16}$$

By assuming unity Lewis number, Eq. (1.15) can be simplified. The energy equation in terms of the static enthalpy takes on a standard convective-diffusive form. In the case of high speed combustion, the energy equation can be introduced in terms of stagnation enthalpy $h_s \equiv h + u_i u_i/2$. However, low speeds are encountered mostly in the problems studied in this thesis.

1.3.2 Reynolds and Favre averaging

The average balance equations for turbulent flames can be obtained by decomposing the instantaneous quantities into mean and fluctuating quantities and describes only the mean flow field. Two methods of averaging, Reynolds and Favre (mass weighted) averaging are commonly used in combustion. These concepts are introduced here as they will be used often later in the thesis.

1.3.2.1 Reynolds averaging

The mean quantity $\bar{Q}$ can be defined in many way depending on the flow conditions (Hinze, 1987; Pope, 2000). Here it is defined as an ensemble average:

$$\bar{Q}(x_i, t) = \frac{1}{N} \sum_{k=1}^{N} Q^k(x_i, t) \tag{1.17}$$

where N is a sample size. The value of a function Q can be decomposed into its mean and the fluctuation:

$$Q(x_i, t) = \bar{Q}(x_i, t) + Q'(x_i, t) \tag{1.18}$$

If Q is averaged, the mean of the fluctuations is zero i.e., $\overline{Q'} = 0$. For example, averaging the mass balance equation leads to:

$$\frac{\partial \bar{\rho}}{\partial t} + \frac{\partial}{\partial x_i}\left(\overline{\rho u_i} + \overline{\rho' u_i'}\right) = 0 \tag{1.19}$$

1.3.2.2 Favre averaging

The previous equation, Eq. (1.19), contains the unclosed velocity and density correlation $\overline{\rho' u_i'}$ which needs explicit modelling. In order to avoid this problem, the Favre (mass weighted) (Favre, 1969) average $\widetilde{Q}$ is introduced:

$$\widetilde{Q} = \frac{\overline{\rho Q}}{\overline{\rho}}, \quad \widetilde{Q''} = \frac{\overline{\rho(Q - \tilde{Q})}}{\overline{\rho}} = 0 \tag{1.20}$$

and any property Q again can be also decomposed into its mean value and the fluctuation:

$$Q(x_i, t) = \widetilde{Q}(x_i, t) + Q''(x_i, t) \tag{1.21}$$

The Favre averaged equations become:

- Mass

$$\frac{\partial \bar{\rho}}{\partial t} + \frac{\partial(\bar{\rho}\tilde{u}_j)}{\partial x_j} = 0 \tag{1.22}$$

- Momentum

$$\frac{\partial(\bar{\rho}\tilde{u}_i)}{\partial t} + \frac{\partial(\bar{\rho}\tilde{u}_i\tilde{u}_j)}{\partial x_j} = -\frac{\partial(\bar{\rho}\widetilde{u_i'' u_j''})}{\partial x_j} - \frac{\partial \bar{p}}{\partial x_i} + \frac{\partial \bar{\tau}_{ij}}{\partial x_j} + \bar{F}_i \tag{1.23}$$

- Species

$$\frac{\partial(\bar{\rho}\tilde{Y}_\alpha)}{\partial t} + \frac{\partial(\bar{\rho}\tilde{u}_j\tilde{Y}_\alpha)}{\partial x_j} = -\frac{\partial(\bar{\rho}\widetilde{u_j''Y_\alpha''})}{\partial x_j} - \frac{\partial\overline{\mathcal{J}_j^k}}{\partial x_j} + \bar{\omega}_\alpha \tag{1.24}$$

- Energy

$$\begin{aligned}\frac{\partial(\bar{\rho}\tilde{h})}{\partial t} + \frac{\partial(\bar{\rho}\tilde{u}_j\tilde{h})}{\partial x_j} &= -\frac{\partial(\bar{\rho}\widetilde{u_j''h''})}{\partial x_j} - \frac{\partial\overline{\mathcal{J}_j^h}}{\partial x_j} \\ &+ \frac{\partial\bar{p}}{\partial t} + \frac{\partial\overline{u_j p}}{\partial x_j} + \frac{\partial\overline{u_i\tau_{ij}}}{\partial x_j} + \overline{u_j F_j} + \bar{q}_{RAD}\end{aligned} \tag{1.25}$$

The Reynolds stresses, $\widetilde{u_i''u_j''}$ and the turbulent fluxes in terms of $\widetilde{u_j''\psi_k''}$, ψ is for any property, appear that represent the process of turbulent diffusion. These quantities are unknown. The proposal of closures for the unknown quantities is known as turbulence modelling. Turbulent combustion modelling is concerned with the closure of the mean chemical reaction rates of species.

1.3.2.3 Mean reaction rate

In Eq. (1.24), the averaged chemical source term appears. If a simple irreversible reaction between fuel (F) and oxidizer (O) is considered, F+O→Product, the instantaneous mass reaction rate of fuel $\omega_{_F}$ is expressed from the Arrhenius law as:

$$\omega_{_F} = A\rho^2 T^b Y_F Y_O \exp\left(-\frac{T_a}{T}\right), \qquad T_a = \frac{E_a}{R} \tag{1.26}$$

where A is a constant, $A = \frac{A_0}{MW_O}$ with the frequency factor A_0 of the Arrhenius rate.

If the reaction rate is decomposed into a mean and a fluctuation:

$$\omega = \bar{\omega} + \omega' = A\bar{\rho}^2(\widetilde{T}^b + T''^b)(\widetilde{Y}_F + Y_F'')(\widetilde{Y}_O + Y_O'') \exp\left(-\frac{T_a}{\widetilde{T} + T''}\right) \quad (1.27)$$

If $T'' \cong 0$:

$$\bar{\omega} = A\bar{\rho}^2\widetilde{T}^b\left(\widetilde{Y}_F\widetilde{Y}_O + \widetilde{Y_F''Y_O''}\right) \exp\left(-\frac{T_a}{\widetilde{T}}\right) \quad (1.28)$$

If $T'' \ncong 0$:

$$\bar{\omega} = A\bar{\rho}^2\widetilde{T}^b\widetilde{Y}_F\widetilde{Y}_O \overline{\exp\left(-\frac{T_a}{\widetilde{T} + T''}\right)} + A\bar{\rho}^2\overline{T''^bY_F''Y_O'' \exp\left(-\frac{T_a}{\widetilde{T} + T''}\right)} \quad (1.29)$$

In Eq. (1.29), the second term is problematic. The use of a Taylor series gives (Veynante and Vervisch, 2002):

$$\begin{aligned} \exp\left(-\frac{T_a}{\tilde{T}}\right) &= \exp\left(-\frac{T_a}{\tilde{T}}\right)\left(1 + \sum_{n=1}^{+\infty} P_n\frac{T''^n}{\tilde{T}_n}\right) \\ T^b &= \tilde{T}^b\left(1 + \sum_{n=1}^{+\infty} Q_n\frac{T''^n}{\tilde{T}_n}\right) \end{aligned} \quad (1.30)$$

where P_n and Q_n are given by:

$$\begin{aligned} P_n &= \sum_{k=1}^{n}(n-k)^{n-k}\frac{(n-1)!}{(n-k)![(k-1)!]^2k}\left(\frac{T_a}{\tilde{T}}\right)^k \\ Q_n &= \frac{b(b+1)\ldots(b+n-1)}{n!} \end{aligned} \quad (1.31)$$

The mean reaction rate, $\bar{\omega}_F$ becomes (Bilger, 1980; Klimenko and Bilger,

1999; Veynante and Vervisch, 2002):

$$\begin{aligned}\bar{\omega}_{_F} &= A\bar{\rho}^2\tilde{T}^b\tilde{Y}_F\tilde{Y}_O\exp\left(-\frac{T_a}{\tilde{T}}\right)\\ &\times \left[1+\frac{\widetilde{Y_F''Y_O''}}{\tilde{Y}_F\tilde{Y}_O}+(P_1Q_1)\left(\frac{\widetilde{Y_F''T''}}{\tilde{Y}_F\tilde{T}}+\frac{\widetilde{Y_O''T''}}{\tilde{Y}_O\tilde{T}}\right)\right.\\ &+ \left.(P_2+Q_2+P_1Q_1)\left(\frac{\widetilde{Y_F''T''^2}}{\tilde{Y}_F\tilde{T}^2}+\frac{\widetilde{Y_O''T''^2}}{\tilde{Y}_O\tilde{T}^2}\right)+\cdots\right] \qquad (1.32)\end{aligned}$$

Eq. (1.32) contains higher order moments; variances and co-variances. The Taylor series expansion converges only for $T''/\widetilde{T} \ll 1$ and in order to achieve accurate results more higher correlations are needed. Eq. (1.32) only represents 1-step irreversible reaction and can not be easily extended to realistic chemical schemes (multi-step and reversible). Turbulent combustion models aim to model $\bar{\omega}_F$. The Conditional Moment Closure that will be introduced in Chapter 2 by-passes the problem of calculating $\bar{\omega}_F$ by performing a conditional average, in the hope that the conditional fluctuations are small enough for the term in brackets in Eq. (1.32) to become negligible. This point will be discussed fully in Chapter 2.

1.4 Turbulence models

The averaged balance equations are not closed until the unknown quantities are specified. Turbulence models provide the information of the Reynolds stresses and the turbulent fluxes. The turbulence models such as eddy viscosity gradient model, k–ε models, and Reynolds stress models and presented briefly in this section. The main reason is to motivate the choices that will

be made in Computational Fluid Dynamics (CFD) solutions in Chapter 3, 4 and 5.

1.4.1 Zero-equation models

These models use the mixing length formula of Prandtl and eddy viscosity formula (Hinze, 1987; Warnatz et al., 2001; Pope, 2000). The Reynolds stress is modelled by :

$$-\overline{u'v'} = \nu_t \frac{\partial \bar{u}}{\partial y} \tag{1.33}$$

where ν_t is the eddy-viscosity. The mixing length hypothesis of Prandtl for a two dimensional boundary layers gives that $\nu_t = l_m^2 \,|\, \partial\bar{u}/\partial y \,|$. However, this model can not be easily extended to other more complicated flows.

1.4.2 One-equation models

In these models, an additional partial differential equation for the turbulent kinetic energy ($k \equiv \widetilde{u_i'' u_i''}/2$) is solved:

$$\frac{Dk}{Dt} = P_k - \varepsilon + \frac{\partial}{\partial x_j}\left[\left(\nu + \frac{\nu_t}{\sigma_k}\right)\frac{\partial k}{\partial x_j}\right] \tag{1.34}$$

and the Reynolds stress may be defined according to the eddy viscosity hypothesis:

$$\widetilde{u_i'' u_j''} = \frac{2}{3}\delta_{ij}\left(k + \nu_t \frac{\partial \tilde{u}_k}{\partial x_k}\right) - \nu_t\left(\frac{\partial \tilde{u}_i}{\partial x_j} + \frac{\partial \tilde{u}_j}{\partial x_i}\right) \tag{1.35}$$

where σ_k is the turbulent Prandtl number for the diffusion of kinetic energy, $P_k = -\widetilde{u_i'' u_j''}\frac{\partial \tilde{u}_i}{\partial x_j}$, $\varepsilon = k^{(3/2)}/l$ and $\nu_t = C_\mu k^{1/2} l$ with $C_\mu = 0.09$. The advantage of these models is that the problem with ν_t becoming zero when the mean

velocity gradients vanishes, a problem with the zero-equation models, does not appear. However, the main weakness is that it is not possible to prescribe the lengthscale in many types of flow.

1.4.3 Two-equation models

In these models, the Reynolds stress is linearly related to the mean rate of strain via an eddy viscosity, and the latter is given by an additional equation. The well-known $k-\varepsilon$ model (Jones and Launder, 1972; Jones and Whitelaw, 1985), in which transport equations are solved for two turbulence quantities, i.e., k and ε, can be derived like a conservation equation:

$$\frac{D\varepsilon}{Dt} = C_{\varepsilon 1}\frac{\varepsilon}{k}P_k - C_{\varepsilon 2}\frac{\varepsilon^2}{k} + \frac{\partial}{\partial x_j}\left[\left(\nu + \frac{\nu_t}{\sigma_\varepsilon}\right)\frac{\partial \varepsilon}{\partial x_j}\right] \tag{1.36}$$

where $\nu_t = C_\mu k^2/\varepsilon$ and the quantities $C_{\varepsilon 1}, C_{\varepsilon 2}$ and σ_ε are constants. $C_{\varepsilon 1} = 1.44, C_{\varepsilon 2} = 1.92$ are standard values. This model is usually of acceptable accuracy for simple flows, but it can be quite inaccurate for complex flows, for example, it can not capture the stabilising/destabilising influence of swirling motions and buoyancy forces. Even for a simple round jet, the constants need to adjust, for example, $C_{\varepsilon 2} = 1.77$ for axi-symmetric round jet is recommended than the standard value of 1.92 (Pope, 2000). In Chapter 3, further tuning of these constants will be performed in order to make CFD solutions agree with experimental data.

1.4.4 Reynolds stress models

In Reynolds stress models, the transport equations are solved for the individual Reynolds stresses and for the dissipation. Consequently, the turbulent viscosity hypothesis is not needed. These models are considered more accurate. The transport equation for the Reynolds stresses and the turbulent fluxes have been reported in Launder et al. (1975) and Speziale et al. (1991). Launder et al. (1975) model provides linear functions of pressure-strain correlation while Speziale et al. (1991) model is quadratically non-linear. In Chou et al. (2004), the model given by Launder et al. (1975) gives better solution in opposed-jet mixing flows. We will use Reynolds stress models in Chapter 3 and Chapter 5.

1.4.5 Dissipation and Scalar Transport

In Eqs. (1.24) and (1.25), another unclosed term, of $\widetilde{u_j''\psi_\alpha''}$, also appears. ψ may represent reactive scalar for the mass fraction of a chemical species or temperature.

The scalar flux can be modelled as:

$$\widetilde{u_j''\psi_\alpha''} = -\mathcal{D}_t \frac{\partial \tilde{\psi}_\alpha}{\partial x_j} , \qquad \mathcal{D}_t = \frac{\nu_t}{Sc_t} \tag{1.37}$$

where Sc_t is a turbulent Schmidt number and $\mathcal{D}_t$ is a turbulent diffusivity. The variance $(\widetilde{\psi''^2})$ can be found by the following transport equation, which can be derived by subtracting Eq. (1.24) from Eq. (1.4) and the mean value

of the molecular diffusive flux is neglected (Peters, 2000; Kuo, 1986):

$$\frac{\partial\bar{\rho}\widetilde{\psi_\alpha''^2}}{\partial t}+\frac{\partial\bar{\rho}\tilde{u}_i\widetilde{\psi_\alpha''^2}}{\partial x_i}=-\frac{\partial}{\partial x_i}\left(\bar{\rho}\widetilde{u_i''\psi_\alpha''^2}\right)+2\bar{\rho}(-\widetilde{u_i''\psi_\alpha''})\left(\frac{\partial\tilde{\psi}_\alpha}{\partial x_i}\right)-\bar{\rho}\tilde{\chi}_\alpha+2\bar{\rho}\widetilde{\psi_\alpha''\omega_\alpha''} \tag{1.38}$$

The terms on the l.h.s. describe the local rate of change and convection. The first term on the r.h.s. is the turbulent transport term, the second one is related to the production of scalar fluctuations and the last term is the covariance of the chemical source term. The molecular diffusivity appears in the dissipation term which is defined by:

$$\tilde{\chi}_\alpha=2\mathcal{D}_\alpha\left(\frac{\partial\widetilde{\psi_\alpha''}}{\partial x_i}\frac{\partial\widetilde{\psi_\alpha''}}{\partial x_i}\right) \tag{1.39}$$

Furthermore, it can be related with an integral time scale which is $\tau_\alpha = \widetilde{\psi_\alpha''^2}/\tilde{\chi}_\alpha$. For non-reacting case, it is often assumed that the scalar timescale is related to the flow time $\tau=\tilde{k}/\tilde{\varepsilon}$ with $\tau=C_D\tau_\alpha$, which leads to:

$$\tilde{\chi}_\alpha=C_D\frac{\tilde{\varepsilon}}{\tilde{k}}\widetilde{\psi_\alpha''^2} \tag{1.40}$$

where C_D is a constant normally taking the value of 2 (Peters, 2000; Béguier et al., 1978). The model of Eq. (1.40) will be referred to often in this thesis, as it gives a very important quantity in CMC modelling. For some flows, especially for situations where the residence time is short relative to the integral time scale, C_D must be much higher than 2 to give the right scalar dissipation (Eswaran and Pope, 1988). This is a crucial point of discussion in Chapter 5.

1.5 Turbulent reacting flows

1.5.1 Statistical properties of turbulent reacting flows

The turbulent flow is a random process. In order to describe the process, probability density functions (PDF) and conditional moments are frequently used and these will be introduced in the following discussion. More details can be found in Pope (1985, 2000) and Peters (2000).

The PDF of a random variable ϕ is denoted by $P(\phi)$, which is the derivative of the distribution function $F(\phi)$, i.e. $P(\phi) \equiv dF(\phi)/d\phi$. The PDF is non-negative and the normalization condition is that $\int_{-\infty}^{\infty} P(\phi)d\phi = 1$. Therefore the average of a statistical quantity $Q(\phi)$ can be denoted by $\langle Q \rangle$ or $\bar{Q}$:

$$\overline{Q} = \langle Q \rangle = \int_{-\infty}^{\infty} Q(\phi)P(\phi)d\phi \tag{1.41}$$

If the random variable is a vector ϕ with n components, the PDF of one variable ϕ_α can be obtained from the joint PDF of ϕ by integration over all variables except itself. It is called the marginal PDF of ϕ_α:

$$P(\phi_\alpha) = \int_{-\infty}^{\infty} ... \int_{-\infty}^{\infty} P(\phi)d\phi_1 ... d\phi_{\alpha-1}d\phi_{\alpha+1} ... d\phi_n \tag{1.42}$$

If Q is a function of ϕ and ξ, the conditional PDF , $P(\phi|\xi = \eta)$, is defined according to Bayes' theorem:

$$P(\phi|\xi = \eta) = \frac{P(\phi, \eta)}{P(\eta)} \tag{1.43}$$

where $P(\phi, \eta)$ is the joint PDF.

The conditional expectation of Q at given η is then defined:

$$\begin{aligned} \langle Q(\phi|\xi=\eta)\rangle &= \int_{-\infty}^{\infty} Q(\phi,\eta)P(\phi|\xi=\eta)d\phi \\ &= \frac{1}{P(\eta)}\int_{-\infty}^{\infty} Q(\phi,\eta)P(\phi,\eta)d\phi \end{aligned} \tag{1.44}$$

The unconditional mean of Q can be obtained by:

$$\bar{Q}(\phi) = \langle Q(\phi)\rangle = \int_{-\infty}^{\infty} Q(\phi|\xi=\eta)P(\eta)d\eta \tag{1.45}$$

If the random variables ϕ and η are independent and since the joint PDF is the product of their marginal PDF's, then $P(\phi,\eta) = P(\phi)P(\eta)$. The distinction between conditional and unconditional averaging is very important in this thesis, since we will be dealing with a model that predicts conditional averages, which are then used to calculate unconditional averages using Eq. (1.45).

1.5.2 Mixture fraction

The mixture fraction is one of most important quantities for describing non-premixed combustion. According to Bilger (1980), the fast-chemistry assumption implies that the instantaneous concentrations species and the temperature are functions only of the conserved scalar and this can drastically simplify the solution of reacting flow problems in the limit of fast chemistry (Kuo, 1986; Turns, 2000).

If we consider a two-stream problem having an inlet of fuel stream and a second inlet with an oxidizer stream, the mixture fraction can be defined as

the ratio of mass of material having its origin in the fuel stream to the mass of mixture. The mixture fraction, which varies between zero and one, may be defined as (Bilger, 1976):

$$\xi = \frac{\beta - \beta_{ox,0}}{\beta_{fu,0} - \beta_{ox,0}} \tag{1.46}$$

where the oxidizer-fuel coupling function, β=$Y_{fu} - Y_{ox}/S$, S is the stoichiometric oxygen to fuel mass ratio[1]. If all diffusivities $\mathcal{D}_\alpha$ are equal to $\mathcal{D}$, the mixture fraction ξ satisfies the balance equation (Eq. 1.4) which has no chemical source term:

$$\frac{\partial \rho\xi}{\partial t} + \frac{\partial \rho u_j \xi}{\partial x_j} = \frac{\partial}{\partial x_j}\left(\rho\mathcal{D}\frac{\partial \xi}{\partial x_j}\right) \tag{1.47}$$

The Favre mean mixture fraction $\widetilde{\xi}$ version of Eq. (1.47) can be found from Eq. (1.24) and the Favre variance of the mixture fraction, $\widetilde{\xi''^2}$, can be obtained from Eq. (1.38) without the chemical source term.

$$\frac{\partial \bar{\rho}\widetilde{\xi}}{\partial t} + \frac{\partial \bar{\rho}\widetilde{u}_j\widetilde{\xi}}{\partial x_j} = -\frac{\partial}{\partial x_j}\left(\bar{\rho}\widetilde{u_j''\xi''}\right) \tag{1.48}$$

$$\frac{\partial \bar{\rho}\widetilde{\xi''^2}}{\partial t} + \frac{\partial \bar{\rho}\widetilde{u}_i\widetilde{\xi''^2}}{\partial x_i} = -\frac{\partial}{\partial x_i}\left(\bar{\rho}\widetilde{u_i''\xi''^2}\right) + 2\bar{\rho}(-\widetilde{u_i''\xi''})\left(\frac{\partial \widetilde{\xi}}{\partial x_i}\right) - \bar{\rho}\widetilde{\chi} \tag{1.49}$$

The molecular diffusivity $\mathcal{D}$ in Eq. (1.47) is much smaller than the turbulent diffusivity $\mathcal{D}_t$ and has therefore been neglected in Eq. (1.48). Since the mixture fraction is a non-reacting scalar, the gradient transport assumption

[1] S=$\nu MW_{ox}/MW_{fu}$, ν are the kmols of oxygen needed to completely oxidize 1kmol of the fuel.

in Eq. (1.37) is used (Peters, 2000). Eq. (1.48) and Eq. (1.49) are necessary to solve in CMC modelling. In this thesis, they will be solved by a CFD package.

1.6 Turbulent combustion models

1.6.1 Eddy-Break-Up and Eddy dissipation

The Eddy-Break-Up model of premixed combustion by Spalding (1971) gives the mean reaction rate in fast chemistry as fully governed by the turbulent dissipation. The turbulent mixing process from the integral down to the molecular scales, the energy cascade (Richardson, 1922), can control the chemical reactions. Hence:

$$\bar{\omega}_{fu} = -\bar{\rho} A \frac{\varepsilon}{k} \sqrt{\overline{Y'^{\,2}_{fu}}} \tag{1.50}$$

In the Eddy-Break-Up model, the reaction occurs when cold reactants mix with hot products. For infinitely fast chemistry, the variance can be modelled as $\overline{Y'^{\,2}_{fu}} \simeq \bar{Y}_{fu}(1 - \bar{Y}_{fu})$. This model tends to overestimate the reaction rate, especially in highly strained regions, where the ε/k is large (Veynante and Vervisch, 2002).

This model has been modified to the Eddy dissipation model for non-premixed combustion by Magnussen and Hjertager (1977) that replaced the variance of the product mass fraction with the mean mass fraction of the

deficient species, for instance fuel for lean or oxygen for rich mixtures :

$$\bar{\omega}_{fu} = -\bar{\rho}A\frac{\varepsilon}{k}\min\left(\bar{Y}_{fu},\ \frac{\bar{Y}_{ox}}{S},\ B\frac{\bar{Y}_P}{1+S}\right) \tag{1.51}$$

where A and B are modelling constants, $\bar{Y}_{fu}, \bar{Y}_{ox}$ and $\bar{Y}_P$ are the mean mass fraction of fuel, oxygen and products respectively. This model is valid for very fast chemistry and the reaction rate is determined by the rate of turbulent mixing i.e. ε/k. It is widely used in commercial CFD codes, but it is difficult to handle finite-rate chemistry (Bai and Fuchs, 1995). Introducing finite-rate chemistry is important so as to be in a position to predict pollutant formation and other phenomena such as extinction. This is one of the main reasons why CMC is studied in this thesis. Other models that can handle finite-rate chemistry are the flamelet and PDF methods, described next.

1.6.2 Laminar flamelet

If the reaction is very fast and the relevant chemical time scale is short compared to the convection-diffusion time scales ($Da \gg 1$), the reaction occurs only in thin layers. These layers are taken as a wrinkled sheet and called flamelets (Peters, 1986). If the thickness of the layers (the reaction zone) is small compared to Kolmogorov length scale, the local behaviour of the flame can be regarded as laminar and the molecular diffusion determines the species transport across these reaction zones (Peters, 2000; Brethouwer, 2000).

The related early models, e.g. the “mixed is burnt” model, assume that fuel and oxidizer react in stoichiometric proportions at the flame sheet at

an infinitely fast reaction that results in an infinitesimally thin sheet (Burke and Schumann, 1928). The chemical equilibrium model has also been used with success (Becker, 1974; Kent and Bilger, 1973; Lockwood and Naguib, 1975), where now chemical equilibrium is assumed. However, this does not include the non-equilibrium effect that the fuel diffuses nearly unreacted to stoichiometric mixture fraction and hence equilibrium models gave bad prediction for the intermediate products (Peters, 1984a). In order to solve the coupling between non-equilibrium chemistry and turbulence, the mixture fraction and the instantaneous scalar dissipation rate, χ is introduced. After a coordinate transformation from spatial coordinate normal to the flamelet to mixture fraction, the reactive-diffusive structure in the vicinity of that surface gives the flamelet model of non-premixed combustion (Peters, 2000; Bray and Peters, 1994; Bilger, 1988) :

$$\rho\frac{\partial\psi_\alpha}{\partial\tau} = \frac{\rho}{Le_\alpha}\frac{\chi}{2}\frac{\partial^2\psi_\alpha}{\partial\xi^2} + \omega_\alpha \text{ with} \quad \chi = 2\mathcal{D}\frac{\partial\xi}{\partial x_i}\frac{\partial\xi}{\partial x_i} \tag{1.52}$$

where τ is Lagrangian time scale (Swaminathan and Bilger, 1999; Peters, 1984a; Klimenko, 2001). Eq. (1.52) is the "flamelet equation" for $Le = 1$. If unsteady effects are neglected, the time derivative vanishes, and the reaction term is balanced by the diffusion term. The scalar dissipation rate, χ, is a very important quantity in the flamelet model for non-premixed turbulent combustion. It represents the inverse of a diffusion time scale and a diffusion in mixture fraction. If Eq. (1.52) is solved as function of $\psi(\xi, \chi)$, and the form of probability density function (PDF) of χ and ξ is known, then the

mean quantity can be computed:

$$\overline{\psi_\alpha} = \int\int \psi_\alpha(\xi,\chi)P(\xi,\chi)d\xi d\chi \tag{1.53}$$

It has been argued by Bilger (2000) that the flamelet model neglects the influence of spatial terms in the equation and the effects of variations in scalar dissipation rate, since the scalar dissipation rate is not constant in whole domain. Veynante and Vervisch (2002) and Peters (1984a) reported that the steady laminar flamelet model is not valid in the presence of local extinction and re-ignition, situations where significant local variations of scalar dissipation rate χ may be present.

1.6.3 Probability Density Function method

Probability Density Function (PDF) represents a very general statistical description of turbulent reacting flows and it is applicable to premixed, non-premixed and partially premixed combustion. The transport equation for the joint PDF of velocities and reactive scalars can be derived from the Navier-Stokes equations and the convection-diffusion equation for the scalar (Pope, 1985, 2000).

$$\frac{\partial(\rho P)}{\partial t} + \frac{\partial(\rho u_j P)}{\partial x_j} + \left(\rho g - \frac{\partial \bar{p}}{\partial x_i}\right)\frac{\partial P}{\partial u_j} + \sum_{k=1}^{n}\frac{\partial}{\partial \psi_k}(w_k P) = \tag{1.54}$$
$$\frac{\partial}{\partial u_j}\left\{\left\langle -\frac{\partial \tau_{ij}}{\partial x_j} + \frac{\partial p'}{\partial x_i} \mid u,\psi \right\rangle P\right\} - \sum_{k=1}^{n}\frac{\partial}{\partial \psi_k}\left\{\left\langle \frac{\partial}{\partial x_j}\left(\rho\mathcal{D}\frac{\partial \psi_k}{\partial x_j}\right) \mid u,\psi \right\rangle P\right\}$$

Eq. (1.54) shows the joint PDF transport equation and it is expressed in conservative form (Peters, 2000; Pope, 1985). The first two terms on the l.h.s. represent the local rate of change and convection of PDF in physical space. The third term is the transport by gravity in velocity space and the mean pressure gradient and the chemical source term follow. The l.h.s. of Eq. (1.54) contains only known terms. However, the r.h.s. terms are unclosed where conditional gradients of quantities appear. The first r.h.s. term is the PDF transport in velocity space by the viscous stresses and fluctuating pressure gradient and the second term represents transport by molecular fluxes in reactive scalar space (molecular mixing). Models are provided for these terms, some of which are similar to the CMC sub-models in Chapter 2. The PDF equations is solved by using the Monte Carlo method. This method treats the turbulent reacting flow as an ensemble of particles so that each particle has its own position and composition and travels in the flow with instantaneous velocity. The particle state is described by its position, velocity and reactive scalars and the particle properties are described by stochastic Lagrangian models. More information can be obtained from Pope (1985, 2000).

Mixing models (IEM, LMSE, MC and EMST (Pope, 2000; Peters, 2000)) in the PDF model are needed to account for mixing by molecular diffusion (micro-mixing), but none of the mixing models includes a physically realistic representation of scalar dissipation rate to capture local extinction and re-ignition problems (Bilger, 2000).

1.7 Conclusions

The fundamental governing equations for reacting flow and turbulence modelling have been described here. Moreover, several concepts of non-premixed combustion models are reviewed.

The models that can incorporate finite-rate chemistry (flamelets and PDF) have found extensive use. However, the flamelet model neglects the influence of convection-diffusion in space and the effects of variations in scalar dissipation rate across the domain. Hence, the flamelet may not be valid in the presence of local extinction and re-ignition. The mixing models for the PDF model involving molecular diffusion have difficulty in predicting the scalar dissipation rate to capture local extinction and re-ignition problems. The computational cost is expected to vary as PDF model > Conditional Moment Closure > flamelet. The Conditional Moment Closure for turbulent diffusion flames, that aims to partly resolve these problems, will be presented in the next Chapter.

Chapter 2

Conditional Moment Closure (CMC) and its numerical solution

This Chapter is organised as follows. Firstly, the CMC equations and the closure hypothesis are presented. Secondly, the sub-models in the CMC are described and validated by comparison with DNS data. The boundary conditions are also discussed. The chapter closes with a description of the numerical methods for the solution of the CMC equations.

2.1 The first order CMC

2.1.1 Main concept

The CMC for non-premixed turbulent combustion modelling has been independently developed by Klimenko (1990) and Bilger (1993) and is one of

the advanced models for turbulent reacting flows. The main concept behind CMC is to find how the reactive scalars (e.g. temperature, species mass fractions) depend on the mixture fraction. There are two different mathematical procedures to derive the CMC model; the joint PDF method by Klimenko (1990) and the decomposition method by Bilger (1993). However, they yield the same form of the CMC equation, which gives substantial credence to the model. CMC can be applied for infinitely fast and finite rate chemistry (Klimenko and Bilger, 1999), hence overcoming the problem of limited range of validity that other closures have met.

In non-premixed problems, the value of concentrations and temperature within the mixing field between fuel and oxidant appear to depend strongly on the local instantaneous value of some variable, such as mixture fraction. If turbulent mixing occurs without significant differential molecular diffusion and running under low Mach number, the mixture fraction contains all the information on the elemental composition and enthalpy (temperature) at any point at any instant in the flow (Bilger, 1989). The CMC model calculates conditional moments at a fixed location within the flow field using modelled transport equations for the conditional moments of the reactive scalars with no assumptions on the small scale structure of reaction zones or on the relative timescale of chemistry and the turbulence. In this chapter, the decomposition method by Bilger (1993) will be used for the derivation.

If the fluctuations of the reactive scalars at a given mixture fraction value are small, the first order CMC can result in accurate predictions in non-premixed turbulent combustion. If the fluctuations of the reactive scalars at a given mixture fraction value are large, then the first order CMC is no

longer applicable and the second order CMC is needed. In this thesis, the first order CMC is only considered and described, but emphasis is put on the spatial dependence of the conditional averages, an aspect of CMC research very little explored so far (Klimenko and Bilger, 1999). The second order CMC remains for future study.

The first order CMC has been applied to wide range of combustion problems in the past and performed successfully for attached turbulent non-premixed jet flames (Roomina and Bilger, 2001; Smith et al., 1992, 1995; Fairweather and Woolley, 2003), autoignition problems (Mastorakos and Wright, 2003; Kim et al., 2000a; Kim and Huh, 2002b), bluff-body flames (Kim et al., 2000b; Kim and Huh, 2002a) and lifted turbulent non-premixed jet flames (Devaud and Bray, 2003; Devaud et al., 2003; Kim and Mastorakos, 2005).

Table 2.1 lists various other CMC works. It is evident that there is a trend towards more complex problems involving finite-rate chemistry.

In the following Section, the first order CMC equations are described.

Reference	Flame type	Dimensionality	Order	Chemistry	Comments
Smith et al. (1992)	attached jet	$1D$	$1st$	12 species H_2	first application in CMC
Fairweather and Woolley (2003)	attached jet	$1D$	$1st$	18 species H_2	poor NO prediction, need higher order
Roomina and Bilger (2001)	piloted jet	$0D$	$1st$	50 species, methanol	$\langle N\|\eta\rangle$ modeling important for NO_x
Mastorakos and Bilger (1998)	autoignition	$0D$	$2nd$	$1-step$	N'' important
Kim et al. (2000b)	bluff-body	$2D$	$1st$	43-step methanol	spatial terms important
Devaud and Bray (2003)	lifted jet	$1D$	$1st$	14-step H_2	axial spatial term important
Kim and Mastorakos (2005)	lifted jet	$2D$	$1st$	28-step H_2	spatial diffusion important before burning
Kim and Huh (2004)	piloted jet	$1D$	$2nd$	4-step	1-step correlation only for $2nd$ order
Kronenburg (2004)	non-premixed	$0D$	double condition by enthalpy	2-step	capture local extinction/ re-ignition

Table 2.1: Some important applications of CMC calculations

2.1.2 Species equation

The CMC transport equations concern the conditional mean of reactive scalars, Q_α. These can be defined as $Q_\alpha(\eta;x,t) \equiv \langle Y_\alpha(x,t)\,|\,\xi(x,t)=\eta\rangle \equiv \langle Y_\alpha(x,t)\,|\,\eta\rangle$, at location x and time t. η is the sample space variable for the mixture fraction. The instantaneous mass fraction, Y can be decomposed into a conditional mean and a fluctuation as:

$$Y_\alpha(x,t) = Q_\alpha\left(\eta;x,t\right) + Y''_\alpha(x,t) \tag{2.1}$$

Conditional averaging $\langle\cdot\mid\eta\rangle$ is applied to Eq. (2.1) and $\langle Y''\mid\eta\rangle = 0$ by definition. The function $Q(\eta;x,t)$ is a non-random function of variables x, t and η. Variable η is a sample space for ξ.

Differentiation of Eq. (2.1) gives (Klimenko and Bilger, 1999):

$$\frac{\partial Y}{\partial t} = \frac{\partial Q}{\partial t} + \frac{\partial Q}{\partial \eta}\frac{\partial \xi}{\partial t} + \frac{\partial Y''}{\partial t} \tag{2.2}$$

$$\frac{\partial Y}{\partial x_i} = \frac{\partial Q}{\partial x_i} + \frac{\partial Q}{\partial \eta}\frac{\partial \xi}{\partial x_i} + \frac{\partial Y''}{\partial x_i} \tag{2.3}$$

The molecular diffusive flux term in Eq. (1.4) can be considered by decomposition of Eq. (2.1):

$$\begin{aligned}\frac{\partial}{\partial x_i}\left(\rho\mathcal{D}\frac{\partial Y}{\partial x_i}\right) \;=\; & \frac{\partial}{\partial x_i}\left(\rho\mathcal{D}\frac{\partial Q}{\partial x_i}\right) + \frac{\partial Q}{\partial \eta}\frac{\partial}{\partial x_i}\left(\rho\mathcal{D}\frac{\partial \xi}{\partial x_i}\right) \\ & + \rho\mathcal{D}\left(\frac{\partial \xi}{\partial x_i}\frac{\partial \xi}{\partial x_i}\right)\frac{\partial^2 Q}{\partial \eta^2} + \rho\mathcal{D}\frac{\partial \xi}{\partial x_i}\left(\frac{\partial}{\partial x_i}\frac{\partial Q}{\partial \eta}\right) \\ & + \frac{\partial}{\partial x_i}\left(\rho\mathcal{D}\frac{\partial Y''}{\partial x_i}\right)\end{aligned} \tag{2.4}$$

The chemical source term can be rewritten in terms of the conditional averages by substituting Eqs. (2.2-2.4) into Eq. (1.4):

$$\begin{aligned}\omega = \rho\mathcal{W} \;=\; & \rho\frac{\partial Q}{\partial t} + \rho u_i\frac{\partial Q}{\partial x_i} - \rho\mathcal{D}\left(\frac{\partial\xi}{\partial x_i}\frac{\partial\xi}{\partial x_i}\right)\frac{\partial^2 Q}{\partial\eta^2} - \frac{\partial}{\partial x_i}\left(\rho\mathcal{D}\frac{\partial Q}{\partial x_i}\right) \\ & -\rho\mathcal{D}\frac{\partial\xi}{\partial x_i}\left(\frac{\partial}{\partial x_i}\frac{\partial Q}{\partial\eta}\right) + \rho\frac{\partial Y''}{\partial t} + \rho u_i\frac{\partial Y''}{\partial x_i} - \frac{\partial}{\partial x_i}\left(\rho\mathcal{D}\frac{\partial Y''}{\partial x_i}\right) \\ & +\frac{\partial Q}{\partial\eta}\left\{\rho\frac{\partial\xi}{\partial t} + \rho u_i\frac{\partial\xi}{\partial x_i} - \frac{\partial}{\partial x_i}\left(\rho\mathcal{D}\frac{\partial\xi}{\partial x_i}\right)\right\} \end{aligned} \tag{2.5}$$

where the chemical reaction rate is ω in kg/m^3s represents mass reaction rate per unit volume. The last term of Eq. (2.5) is zero, noticed by Eq. (1.47). The scalar dissipation term will be denoted as $N \equiv \mathcal{D}\left(\frac{\partial\xi}{\partial x_i}\frac{\partial\xi}{\partial x_i}\right)$ and taking the conditional expectation of Eq. (2.5), conditional on $\xi(x,t) = \eta$, yields:

$$\rho_\eta\frac{\partial Q}{\partial t} + \rho_\eta\langle u_i\,|\,\eta\rangle\frac{\partial Q}{\partial x_i} = \rho_\eta\langle N\,|\,\eta\rangle\frac{\partial^2 Q}{\partial\eta^2} + \rho_\eta\langle\mathcal{W}\,|\,\eta\rangle + e_Q + e_Y \tag{2.6}$$

with

$$e_Q \equiv \left\langle\frac{\partial}{\partial x_i}\left(\rho\mathcal{D}\frac{\partial Q}{\partial x_i}\right) + \rho\mathcal{D}\frac{\partial\xi}{\partial x_i}\left(\frac{\partial}{\partial x_i}\frac{\partial Q}{\partial\eta}\right)\Big|\xi(x,t) = \eta\right\rangle \tag{2.7}$$

$$e_Y \equiv -\left\langle\rho\frac{\partial Y''}{\partial t} + \rho u_i\frac{\partial Y''}{\partial x_i} - \frac{\partial}{\partial x_i}\left(\rho\mathcal{D}\frac{\partial Y''}{\partial x_i}\right)\Big|\xi(x,t) = \eta\right\rangle \tag{2.8}$$

where $\rho_\eta \equiv \langle\rho|\eta\rangle$, the conditional fluctuations of density are neglected. Eq. (2.6) represents the unclosed form of the equation for Q.

2.1.3 Primary closure hypothesis

Several unclosed terms appear in Eq. (2.6). The e_Q and e_Y terms are discussed here, with a discussion of $\langle u_i\,|\,\eta\rangle$ and $\langle N\,|\,\eta\rangle$ in Section 2.2. Bilger

(1993) and Li and Bilger (1993) suggest that for finite Schmidt numbers, all the terms in e_Q are of the order Re^{-1}. Hence the unclosed term e_Q is negligible when the Reynolds number is high and there is no differential diffusion. Now the e_Y term will be discussed.

The mean of conditional fluctuations Y'' has been introduced as $\langle Y''|\eta\rangle = 0$ that results in $\langle Y''\rangle = 0$, but this does not necessarily mean that $\langle \frac{\partial Y''}{\partial t}|\eta\rangle = 0$ and $\langle \frac{\partial Y''}{\partial x_i}|\eta\rangle = 0$. However, the unconditional averages can appear in the derivatives as zero: $\langle \frac{\partial Y''}{\partial t}\rangle = \frac{\partial \langle Y''\rangle}{\partial t} = 0$ and $\langle \frac{\partial Y''}{\partial x_i}\rangle = \frac{\partial \langle Y''\rangle}{\partial x_i} = 0$. If we write the unconditional mean as function of the probability density function and the conditional mean, introduced in Eq. (1.45), we obtain:

$$\begin{aligned}\left\langle \frac{\partial Y''}{\partial t} \right\rangle &= \int \left\langle \frac{\partial Y''}{\partial t} \Big| \eta \right\rangle P(\eta) d\eta = 0 \\ \left\langle \frac{\partial Y''}{\partial x_i} \right\rangle &= \int \left\langle \frac{\partial Y''}{\partial x_i} \Big| \eta \right\rangle P(\eta) d\eta = 0 \end{aligned} \tag{2.9}$$

where the integrals are taken over all η that $0 \leq \eta \leq 1$. The unconditional average value of e_Y is expressed:

$$\begin{aligned} -\int e_Y P(\eta) d\eta &= \left\langle \frac{\partial(\rho Y'')}{\partial t} + \frac{\partial}{\partial x_i}(\rho u_i Y'') - \frac{\partial}{\partial x_i}\left(\rho \mathcal{D} \frac{\partial Y''}{\partial x_i}\right) \right\rangle \\ &= \frac{\partial}{\partial x_i}\left(\langle \rho u_i'' Y'' \rangle\right) = \frac{\partial}{\partial x_i}\left(\int \rho_\eta \langle u_i'' Y'' | \eta \rangle P(\eta) d\eta\right) \\ &= \int \frac{\partial}{\partial x_i}\left(\rho_\eta \langle u_i'' Y'' | \eta \rangle P(\eta)\right) d\eta \end{aligned} \tag{2.10}$$

The conditional fluctuations of density ρ and diffusivity $\mathcal{D}$ are neglected so that $\langle \rho Y''|\eta\rangle = \rho_\eta \langle Y''|\eta\rangle = 0$, hence $\langle \rho Y''\rangle = 0$ and $\langle \rho \mathcal{D} \frac{\partial Y''}{\partial x_i}\rangle = \frac{\partial}{\partial x_i}\langle \rho \mathcal{D} Y''\rangle - \langle Y'' \frac{\partial(\rho \mathcal{D})}{\partial x_i}\rangle = 0$. If the velocity is decomposed as $u_i = \langle u_i|\eta\rangle + u_i''$ and multi-

plied by Y'', then the averaging leads to:

$$\langle u_i Y'' | \eta \rangle = \langle u_i'' Y'' | \eta \rangle \tag{2.11}$$

The closure hypotheses (Eqs. 2.9-2.11) gives that the unclosed term e_Y in the decomposition approach is:

$$e_Y P(\eta) = -\frac{\partial}{\partial x_i}\Big(\rho_\eta \langle u_i'' Y'' | \eta \rangle P(\eta)\Big) \tag{2.12}$$

Finally, the governing equation for conditional moment closure of species, $Q_\alpha \equiv \langle \rho Y_\alpha | \eta \rangle \Big/ \langle \rho | \eta \rangle$ can be rewritten:

$$\begin{aligned} \frac{\partial Q_\alpha}{\partial t} + \langle u_i \,|\, \eta \rangle \frac{\partial Q_\alpha}{\partial x_i} &= \langle N \,|\, \eta \rangle \frac{\partial^2 Q_\alpha}{\partial \eta^2} + \langle \mathcal{W}_\alpha | \eta \rangle \\ &\quad - \frac{1}{\overline{\rho}\widetilde{P}(\eta)} \frac{\partial}{\partial x_i}\Big(\langle u_i'' Y_\alpha'' | \eta \rangle \, \overline{\rho}\widetilde{P}(\eta)\Big) \end{aligned} \tag{2.13}$$

with the Favre averaging:

$$\widetilde{Y_\alpha} = \int_0^1 Q_\alpha(\eta)\widetilde{P}(\eta) d\eta, \qquad \langle \rho \,|\, \eta \rangle P(\eta) = \bar{\rho}\widetilde{P}(\eta) \tag{2.14}$$

where $\bar{\rho}$ is the unconditionally averaged density.

In Eq. (2.13), the first term on r.h.s. corresponds to diffusion in mixture fraction space and is quantified by the scalar dissipation rate. The second term on r.h.s. is the conditional expectation of the chemical source term. The last term on r.h.s and l.h.s represent spatial diffusion and convection respectively. These terms are absent in the flamelet model and this constitutes the main difference between the two methods.

The reaction rate is obtained using the first order CMC closure (Klimenko and Bilger, 1999). This closure can be written as $\langle \mathcal{W}_\alpha | \eta \rangle \simeq \mathcal{W}_\alpha(Q_\alpha, Q_T, \bar{p})$.

2.1.4 Enthalpy and Temperature equation

The enthalpy h is a function of species mass fractions Y_α and temperature which is given by:

$$h = h(Y_1, Y_2, ..., Y_n, T) = \sum_\alpha Y_\alpha \left((h_0)_\alpha + \int_{T_0}^{T} (c_p)_\alpha dT \right) \tag{2.15}$$

where $(h_0)_i$ is the formation enthalpy on a standard state and the following term is the sensible enthalpy. At low Mach number, Eq. (1.14) can take the form:

$$\rho \frac{\partial h}{\partial t} + \rho u_i \frac{\partial h}{\partial x_i} - \frac{\partial}{\partial x_i} \left(\rho \mathcal{D} \frac{\partial h}{\partial x_i} \right) = \frac{\partial p}{\partial t} - \rho \mathcal{W}_{RAD} \tag{2.16}$$

where the $\mathcal{W}_{RAD}$ is the heat loss rate per unit mass due to radiation.

The CMC equation for enthalpy $Q_h \equiv \langle \rho h | \eta \rangle / \langle \rho | \eta \rangle$ can be written as:

$$\begin{aligned} \frac{\partial Q_h}{\partial t} + \langle u_i | \eta \rangle \frac{\partial Q_h}{\partial x_i} &= \langle N | \eta \rangle \frac{\partial^2 Q_h}{\partial \eta^2} - \frac{1}{\bar{\rho} \widetilde{P}(\eta)} \frac{\partial}{\partial x_i} \Big(\langle u_i'' h'' | \eta \rangle \bar{\rho} \widetilde{P}(\eta) \Big) \\ &\quad + \left\langle \frac{1}{\rho} \frac{\partial p}{\partial t} \Big| \eta \right\rangle - \langle \mathcal{W}_{RAD} | \eta \rangle \end{aligned} \tag{2.17}$$

The CMC equation for temperature $Q_T \equiv \langle \rho T | \eta \rangle \Big/ \langle \rho | \eta \rangle$ can then be derived from the enthalpy equation (2.17) (Appendix B):

$$\begin{aligned}\frac{\partial Q_T}{\partial t}+\langle u_i|\eta\rangle\frac{\partial Q_T}{\partial x_i} &= \langle N|\eta\rangle\frac{\partial^2 Q_T}{\partial \eta^2}\\ &+\langle N|\eta\rangle\left[\frac{1}{\langle c_p|\eta\rangle}\left(\frac{\partial\langle c_p|\eta\rangle}{\partial\eta}+\sum_{\alpha=1}^{n}(c_p)_\alpha\frac{\partial Q_\alpha}{\partial\eta}\right)\right]\frac{\partial Q_T}{\partial\eta}\\ &-\frac{1}{\bar\rho\widetilde{P}(\eta)}\frac{\partial}{\partial x_i}\Big(\langle u_i''T''|\eta\rangle\bar\rho\widetilde{P}(\eta)\Big)\\ &+\frac{1}{\langle c_p|\eta\rangle}\left\langle\frac{1}{\rho}\frac{\partial p}{\partial t}\Big|\eta\right\rangle-\frac{\langle\mathcal{W}_h|\eta\rangle}{\langle c_p|\eta\rangle}-\frac{\langle\mathcal{W}_{RAD}|\eta\rangle}{\langle c_p|\eta\rangle}\end{aligned}\qquad(2.18)$$

where the source term in Eq. (2.18), $\mathcal{W}_h$ is given by:

$$\langle\mathcal{W}_h|\eta\rangle=\sum_{\alpha=1}^{n}h_\alpha\langle\mathcal{W}_\alpha|\eta\rangle,\qquad\langle\mathcal{W}_\alpha|\eta\rangle\simeq\mathcal{W}_\alpha(Q_\alpha,\,Q_T,\,\bar p)\qquad(2.19)$$

where $\mathcal{W}_\alpha$ is coming from the chemical mechanism in which n species appear and h_α is the enthalpy of species α. The chemical reaction rates $\mathcal{W}_\alpha$ can be found from detailed chemical or reduced chemical mechanisms and evaluated from the CHEMKIN-II package (Kee et al., 1989). In Eq. (2.18), the second term in the l.h.s. and the third term of the r.h.s represent the spatial convection and the spatial diffusion. The first and second term of r.h.s. is for molecular mixing or molecular diffusion in mixture fraction, the fourth term is pressure work and the last two terms are for the chemistry and radiation. The radiation term has not been included in this thesis. Including radiation can be done with a model described in Klimenko and Bilger (1999) although only influences on NO, large on undiluted jet and small on diluted jet, in a preliminary simulation of CMC and PDF method were reported by Barlow et al. (1999). In Chapter 3 to 5, the relative magnitudes of these terms for

various problems will be discussed.

Sub-models for the conditional velocity $\langle u_i|\eta\rangle$, the conditional diffusion fluxes $\langle u_i''\phi''|\eta\rangle$ and the conditional scalar dissipation rate $\langle N|\eta\rangle$ must be provided and are discussed in the next Section, where a comparison with DNS is also given to provide a validation of the various models used for these quantities.

2.2 Validation of sub-models for the unclosed terms

Although the primary unclosed terms for e_Q and e_Y are described in the previous Section, sub-models for the remaining unclosed terms should be developed. In the following Section, various models for the presumed PDF $P(\eta)$, the conditional velocity $\langle u|\eta\rangle$, the conditional scalar dissipation rate $\langle N|\eta\rangle$ and the conditional fluxes $\langle u''\phi''|\eta\rangle$ are compared with DNS. The simulations were performed with an incompressible three dimensional code named FERGUS (Cant, 2002). The initial conditions for the velocity field correspond to isotropic turbulence without mean flow and there is no forcing, which means that the turbulence is decaying. The DNS simulation was aimed at studying autoignition and used an one step n-Heptane mechanism (Lowe et al., 2002). The stoichiometric mixture fraction was 0.0622. For the inhomogeneous case, the averages of the three dimensional DNS data have been taken over a "slab" along the x direction, i.e. a slab consists of y and z space and then averaged due to the homogeneity in y and z direction. For the homogeneous case, all

data in the domain are averaged as one set of data.

Figure 2.1 (a) shows a "sandwich" case for inhomogeneous mixture, i.e. fuel (300K) is located between hot air (1200K) with Re=175. Figure 2.1 (b) is a "spectrum" case for homogenous mixture of fuel and air with Re=100 with assuming unity Lewis number. In the DNS, the Re number is defined based on the computational domain size, turbulence r.m.s. velocity and kinematic viscosity of cold reactants. In this case, the initial mixture fraction was distributed in space by inverting a spectrum in a method similar to the one used to calculate the initial random velocity field. Clipping at ξ=0 and 1 was used and various means ($\tilde{\xi}$) and initial variances were tested.

The flow field information of mixture fraction and turbulent time scale (k/ε) can be seen in Figures 2.2 and 2.3. Figure 2.2 shows the distributions of the mean and r.m.s. of the mixture fraction. Figure 2.2 (a) shows that the maximum mean mixture fraction is decaying and Figure 2.2 (b) that the fluctuation of mixture fraction is spreading wider as time increases. Figure 2.3 presents the mean mixture fraction and the r.m.s. versus time. As expected, the mean mixture fraction does not change and the fluctuation of mixture fraction is decaying as time increases. The turbulent time scale is fairly constant.

2.2.1 Probability Density Function (PDF)

The Probability Density Function (PDF) of the mixture fraction is usually modelled by two methods: Clipped Gaussian PDF and beta PDF. These PDF models are a function of mean mixture fraction $\widetilde{\xi}$ and mixture fraction

r.m.s. $\widetilde{\xi''}$ and are valid only for bimodal mixtures, which is fine for our purposes since the mixture fraction ξ is limited $0 \leq \xi \leq 1$. In this Section, the beta PDF and Clipped Gaussian PDF are validated against our DNS data.

Clipped Gaussian PDF :

Clipped Gaussian PDF considers the distribution of tails outside the boundaries (η=0 and 1) and clips the tails as delta function. The use of Clipped Gaussian PDF and its formula in CMC simulations can be found in Devaud et al. (2003), Cleary and Kent (2003) and Klimenko and Bilger (1999):

$$\begin{aligned} P(\eta) &= \gamma_1\delta(\eta) + (1-\gamma_1-\gamma_2)P_t(\eta) + \gamma_2\delta(1-\eta) \qquad (2.20)\\ P_t(\eta) &= G(\eta)/I_g \\ G(\eta) &\equiv \frac{1}{\sqrt{2\pi\widetilde{\xi''^2}}} exp\left(-\frac{(\eta-\tilde{\xi})^2}{2\widetilde{\xi''^2}}\right) \\ I_g &= \int_0^1 G(\eta)d\eta \\ \gamma_1 &= \int_{-\infty}^0 G(\eta)d\eta \;\; ; \quad \gamma_2 = \int_1^\infty G(\eta)d\eta \end{aligned}$$

where $\delta(x)$ represents the Dirac delta function and γ_1 and γ_2 are the strengths of the delta function at η=0 and η=1 respectively.

beta PDF :

Girimaji (1991) compared the beta PDF with two-scalar mixing data from DNS and concluded that the beta PDF can capture all of the important features of the transition PDFs. The PDF becomes a uniform distribution when the variance is 1/12. Liu et al. (2002) showed that accurate numerical

integration of the beta PDF affected the solution.

The beta PDF is more commonly used in CMC. The idea of the beta PDF is that a random variable Θ of all possible values lies between some finite interval $[\Theta^-, \Theta^+]$. The beta PDF is defined as : $P(\Theta) = \frac{1}{\beta(a,b)}(\Theta - \Theta^-)^{a-1}(\Theta^+ - \Theta)^{b-1}(\Theta^+ - \Theta^-)^{1-a-b}$, with $a = \frac{\langle\Theta\rangle - \Theta^-}{\Theta - \Theta^-}\left(\frac{(\langle\Theta\rangle - \Theta^-)(\Theta^+ - \langle\Theta\rangle)}{\langle\Theta'^2\rangle} - 1\right)$, $b = \frac{\Theta^+ - \langle\Theta\rangle}{\langle\Theta\rangle - \Theta^-}a$ (Cha and Pitsch (2002); Klimenko and Bilger (1999)). Considerations of the boundaries and of the method of integration for beta PDF is also presented in Liu et al. (2002). If the random variable is the mixture fraction, the beta PDF is given by:

$$\begin{aligned} P(\eta) &= \frac{\eta^{r-1}(1-\eta)^{s-1}}{I_b} \\ I_b &\equiv \int_0^1 \eta^{r-1}(1-\eta)^{s-1}d\eta = \frac{\Gamma(r)\Gamma(s)}{\Gamma(r+s)} \\ r &= \tilde{\xi}\left(\tilde{\xi}\frac{1-\tilde{\xi}}{\widetilde{\xi''^2}} - 1\right) \quad ; \quad s = r\frac{1-\tilde{\xi}}{\tilde{\xi}} \end{aligned} \tag{2.21}$$

where $\Gamma(x)$ is the Gamma function.

Both $\widetilde{\xi}$ and $\widetilde{\xi''^2}$ are positive quantities and the limit of the mixture fraction variance is (Klimenko and Bilger, 1999):

$$0 < \widetilde{\xi''^2} < \tilde{\xi}(1-\tilde{\xi}) \tag{2.22}$$

Eq. (2.22) should be checked before Eq. (2.21) is used.

In Figure 2.4 (a), the delta function is evident at relatively high mixture fraction r.m.s. $\widetilde{\xi''}$ and the Clipped Gaussian PDF can capture it accurately in the homogeneous case. Figure 2.4 (b) shows that the two PDF models

are in small difference and are both in excellent agreement with the DNS as the mixture fraction r.m.s. is getting smaller. When the r.m.s. becomes small, Figure 2.4 (c) shows that the Clipped Gaussian PDF produces delta function at η=0 and the overall shape is not acceptable compared with DNS. The beta PDF seems in better agreement. In Figure 2.5 (a), the Clipped Gaussian PDF produces the delta function at the boundaries ($\eta = 0$ and 1) but the DNS data shows no delta function. The beta PDF is closer to the DNS. Figure 2.5 (b) shows that the Clipped Gaussian PDF tends to generate delta function at the boundary ($\eta = 0$), while the beta PDF again gives very good agreement with DNS.

Hence, we conclude that the beta PDF is more accurate than the Clipped Gaussian PDF for both homogeneous and inhomogeneous cases. When the r.m.s. of mixture fraction is relatively small, the two PDF models give similar results.

2.2.2 Conditional velocity

The conditional velocity, $\langle u_i|\eta\rangle$, appears in the CMC equation as a convective term. Here, we consider two different models: the *Linear model* (Klimenko and Bilger, 1999; Swaminathan and Bilger, 2001; Li and Bilger, 1993) and the *PDF gradient model* (Colucci et al., 1998; Bilger, 2000; Swaminathan and Bilger, 2001).

Li and Bilger (1993) analysed experimental data that shows a linear relationship of the conditional velocity in mixture fraction space, but the linear model produced errors where $|\eta - \tilde{\xi}|$ was large. Swaminathan and Bilger

(2001) analysed three different conditional velocity models (linear model, PDF gradient model and PDF model) with DNS. The linear model and the PDF gradient model showed good agreement with DNS. The PDF model gives poor results and needs bigger data set in mixture fraction to capture the right trend. The linear model and PDF gradient model will be only presented in this Section.

Linear model :

$$\begin{aligned} \langle u_i|\eta\rangle &= \tilde{u_i} + \frac{\widetilde{u_i''\xi''}}{\widetilde{\xi''^2}}\left(\eta - \tilde{\xi}\right) \\ \widetilde{u_i''\xi''} &= -\mathcal{D}_t \frac{\partial\tilde{\xi}}{\partial x_i} \end{aligned} \tag{2.23}$$

PDF gradient model :

$$\langle u_i|\eta\rangle = \tilde{u_i} - \mathcal{D}_t \frac{\partial \ln\left(\tilde{P}(\eta)\right)}{\partial x_i} \tag{2.24}$$

Figure 2.6 (a) and Figure 2.7 (a) show that the two models capture the general trend well. As the mixture fraction r.m.s. and the gradient of PDF decreases, the linear model becomes more accurate, as seen in Figure 2.6 (b). In the inhomogeneous case, Figure 2.7 (b) shows that the linear model is better than the gradient model. The use of different presumed PDF shapes affects significantly the results from the gradient model and using the beta PDF seems more accurate. The corresponding PDFs can be found in Figure 2.4 and Figure 2.5 or on Figure 2.6. In Figure 2.6 (b) and Figure 2.7 (b), the error is large when $|\,\eta - \tilde{\xi}\,|$ is large, also found in Li and Bilger (1993).

Hence, the PDF gradient model of conditional velocity can be used for inhomogeneous flows with the right PDF, but it is difficult to use in homogenous cases. The linear model of the conditional velocity can be more accurate in both homogeneous and inhomogeneous cases based on results presented above.

2.2.3 Conditional scalar dissipation

The magnitude of molecular mixing or diffusion in mixture fraction space is determined by the conditional scalar dissipation rate. The conditional scalar dissipation rate plays a very important role in CMC, especially near the reaction zone where $\partial^2 Q_\alpha / \partial \eta^2$ is significant (Li and Bilger, 1993; Klimenko and Bilger, 1999). We consider two different methods: *Amplitude Mapping Closure (AMC) model* (O'Brien and Jiang, 1991) and the *Girimaji model* (Girimaji, 1992).

Mell et al. (1994) performed an evaluation of the conditional scalar dissipation models with DNS in homogeneous turbulence. The analysis shows that the Amplitude Mapping Closure (AMC) model provides excellent data predictions. He and Rubinstein (2003) concluded that the AMC model was incorrect in terms of its asymptotic behaviour for unsymmetric binary mixing (i.e. shifting the peak to the corresponding mean mixture fraction) and suggested a mapping closure approximation (MCA) model from the AMC model. The MCA model showed success in limited cases and a time-dependent function appeared which has not been developed successfully. Devaud et al. (2004) suggested a new method for the conditional scalar dissipation rate

derived from the PDF transport equation and presented very good agreement with inhomogeneous DNS data and also presented the discrepancies of the Girimaji model. There was no time to implement this model here and its use in CMC remains for future study.

The AMC model requires that the extrema of the mixture fraction are always present at unity and zero, hence, some unmixed fluid to be present. The Girimaji model is for homogeneous flows and based on the use of beta PDF for mixture fraction (Girimaji, 1992; Devaud et al., 2004).

Amplitude Mapping Closure (AMC) model

$$\begin{aligned} \frac{\langle N|\eta\rangle}{\langle N\rangle} &= \frac{G(\eta)}{\int_0^1 G(\eta)\tilde{P}(\eta)d\eta} \\ G(\eta) &= \exp\left(-2\left[\mathrm{erf}^{-1}\left(2\eta-1\right)\right]^2\right) \\ \langle N\rangle &= \frac{\tilde{\chi}}{2} \end{aligned} \tag{2.25}$$

where erf is error function.

Girimaji model :

$$\begin{aligned} \frac{\langle N|\eta\rangle}{\langle N\rangle} &= -2\frac{\tilde{\xi}(1-\tilde{\xi})}{\left(\widetilde{\xi''^2}\right)^2}\frac{I(\xi)}{\tilde{P}(\eta)} \\ I(\eta) &= \int_0^\eta \left(\tilde{\xi}\left(\ln\eta'-G_1\right)+(1-\eta')\left[\ln(1-\eta')-G_2\right]\right)\tilde{P}(\eta')(\eta-\eta')d\eta' \\ G_1 &= \int_0^1 \ln(\eta)\tilde{P}(\eta)d\eta \\ G_2 &= \int_0^1 \ln(1-\eta)\tilde{P}(\eta)d\eta \\ \langle N\rangle &= \frac{\tilde{\chi}}{2} \end{aligned} \tag{2.26}$$

The unconditional Favre mean scalar dissipation rate, $\tilde{\chi} = C_D \tilde{\varepsilon}/\tilde{k}\ \widetilde{\xi''^2}$, can be obtained from the conventional equality of the timescales for the velocity and the mixture fraction. Béguier et al. (1978) suggests C_D =2.

In Figure 2.8, the Girimaji model is accurate in all conditions. The AMC model also gives good agreement at the mean mixture fraction. The corresponding PDFs can be found in Figure 2.4 and Figure 2.5 or in the insert of Figure 2.8 and Figure 2.9. The data suggest that the Girimaji model is better at homogenous flows.

In inhomogeneous flows (Figure 2.9), the Girimaji model tends to over predict the conditional scalar dissipation rate. The AMC model using Clipped Gaussian PDF gives under predictions due to the PDF not being accurate. The AMC model with beta PDF gives the most accurate results in the inhomogeneous case.

Devaud et al. (2004) present a better conditional scalar dissipation rate modelling. Arguing the problems of AMC and Girimaji models, they say that AMC needs unmixed fluid that can be a significant constraint in later stages of mixing and that the Girimaji model is valid only for homogenous flows and hence may not be valid in shear layers. They show better prediction of the conditional scalar dissipation rate, but this model is not presented here because of the difficulty of solving the PDF transport equation. The model must be studied further.

2.2.4 Other sub-models

The conditional fluxes are modelled by gradient diffusion :

$$\langle u_i'' Y_\alpha'' | \eta \rangle = -\mathcal{D}_t \frac{\partial Q_\alpha}{\partial x_i} \quad , \qquad \langle u_i'' T'' | \eta \rangle = -\mathcal{D}_t \frac{\partial Q_T}{\partial x_i} \tag{2.27}$$

Figure 2.10 shows the case of homogeneous mixture for the comparison the conditional fluxes gradient diffusion model with DNS. Validation of the conditional fluxes with homogeneous data (i.e. $\frac{\partial \widetilde{T}}{\partial x_i} = 0$) is not serious test, but it gives useful information. Figure 2.10 (a), (b) and (c), (d) represent the conditional fluxes by species and temperature respectively. In Figure 2.10 (a) and (b), the gradient diffusion model is accurate at relatively high mixture fraction r.m.s., while as the r.m.s. is decreasing, it produces large errors where $|\eta - \tilde{\xi}|$ is large in Figure 2.10 (c) and (d). Figure 2.11 shows that the gradient diffusion model for species and temperature fluxes captures very well the DNS trend in the inhomogeneous case. Figure 2.11 (d) shows the temperature flux and shows differences between the model and DNS if $\eta > 0.1$, where the DNS data is also scattered widely. Figure 2.12 shows the instantaneous temperature profiles with iso-lines of the instantaneous mixture fraction and normalised scalar dissipation rate by its mean scalar dissipation rate. Local ignition around the stoichiometry mixture fraction (ξ_{st}=0.0622) with low scalar dissipation rate and unburnt regions around $\xi = 0.2$ with high scalar dissipation rate are observed and this results in the wide scatter plot of the conditional flux (Figure 2.11).

The other remaining sub-models in the CMC equation are taken as:

$$\begin{aligned}
\left\langle \frac{1}{\rho}\frac{\partial p}{\partial t}\Big|\eta \right\rangle &= \frac{1}{\langle\rho|\eta\rangle}\frac{\partial \bar{p}}{\partial t} \\
\langle c_p|\eta\rangle &= \sum_{\alpha=1}^{N}(c_p)_\alpha Q_\alpha \\
\langle\rho|\eta\rangle &= \frac{\bar{p}MW_\eta}{RQ_T}\,, \qquad MW_\eta = \left(\sum_{\alpha=1}^{N}\frac{Q_\alpha}{MW_\alpha}\right)^{-1}
\end{aligned} \tag{2.28}$$

where MW_α is the molecular weight of species α and R is the universal gas constant. The thermodynamic quantities are obtained from CHEMKIN-II (Kee et al., 1989). The pressure related term is related to rapid global expansion or compression in the combustor such as piston motion in a diesel engine. It is not used further in this thesis, as we will be treating constant pressure flames.

2.3 Boundary conditions

Boundary conditions on computational simulation are very important, especially the interactions with walls in combustion problems such as furnaces and engines. In this Section, the content is fully based on Mastorakos and Bilger (2001).

2.3.1 Boundary conditions at the wall for species

If there is no reaction at the wall, the second term on the l.h.s. and the last term in Eq. (2.13) must be zero because of the divergence of the conditional flux of the species normal to the wall. The flux normal to the wall has two

terms. The first is the convection by velocity components normal to wall, $\langle u_i \,|\, \eta \rangle$ and this conditional velocity components should be zero at the wall. At the outer part of wall layer region, the mixture fraction flux is constant at zero across the wall layers: $\overline{u_i' \xi'} = \int_0^1 \langle u_i \mid \eta \rangle (\eta - \tilde{\xi}) P(\eta) d\eta$ in the outer part of layer. It shows that the conditional velocity term should be zero at the outer edge of the layer. Therefore, the velocity must be zero at all mixture fractions at the wall. $\langle u_i'' Y_\alpha'' \,|\, \eta \rangle$ represents the conditional turbulent flux. This flux should also be zero at the wall. If the gradient modelling is employed:

$$\langle u_i'' Y_\alpha'' \,|\, \eta \rangle = -\mathcal{D}_t \frac{\partial Q_\alpha}{\partial x_i} \tag{2.29}$$

Hence $\partial Q_\alpha / \partial x_i = 0$ normal to wall. However, the gradient modelling is not always valid and counter-gradient fluxes may be present (Frank et al., 1999). Mastorakos and Bilger (2001) include in the modelling that the quenching of the reactions at the wall is represented by extra terms for some of the products of radical recombination reactions, which come from setting the radicals as zero at the wall, $Q_\alpha = 0$, where α is the number of species. More details can be seen in Mastorakos and Bilger (2001).

2.3.2 Enthalpy and temperature

The wall is treated as having a reasonably high transverse conduction and high thermal inertia. The wall temperature would be a smooth function of transverse distance and time and would not respond to the short fluctuations of temperature from mixture fraction and enthalpy fluctuations. The

conditional temperature is hence :

$$\langle T \,|\, \eta \rangle = \widetilde{T}_{wall} \tag{2.30}$$

The boundary condition for Q_h in Eq. (2.17) can be obtained from Eq. (2.30).

In second order CMC, boundary conditions for the second-order quantities are needed. The previous boundary condition for the first order CMC can be applied for the variance and covariance terms and may be zero, because no fluctuations of species can be present at the wall.

2.4 Numerical aspects

In this Section, the way of solving the CMC equations is presented. Solvers, interface between CFD and CMC and discretisation methods are discussed.

2.4.1 ODE solvers

The CMC equation is a number of PDE equations and it is stiff due to the chemical reactions. The system size depends on the spatial space, mixture fraction space and the number of scalars. For example, in a 20×20 spatial domain, 100 mixture fraction nodes and 25 species, we have 1,000,000 variables and this results in a very large set of data. Therefore, the PDE equations can be transferred into a number of ODE equations and one of stiff ODE solvers can be used, or a fractional step method can be used.

The ODE solvers solves stiff and nonstiff systems of the form $dy/dt =$

$f(t, y)$ and the solvers used here are LSODE (Hindmarsh, 1983), VODPK (Byrne, 1992) and CHEMEQII (Mott and Oran, 2000). Figure 2.13 shows the comparison of the solvers with GRI-v3 (Smith et al., 1999) mechanism in a homogenous CMC code (i.e. no spatial dependence).

In Figure 2.13, LSODE has a lot of starting cost and CHEMEQII is the fastest among them. Although CHEMEQII gives very fast iteration, it needs generation and destruction of the chemical reaction rates and shows instability dependent on chemistry and other unknown factors, which are under research. CHEMEQII requires attention to use. It also can not handle large systems of ODEs (Richardson, 2004). VODPK is an implicit solver based on backward difference formulae and can handle very large systems of ODEs because it uses iterative methods for large matrix computations.

The elliptic CMC equations (Eqs. 2.13 and 2.18) have spatial and mixture fraction spaces. If the equations are solved by fractional steps between the physical and chemical processes (Devaud and Bray, 2003; Kim et al., 2000a; Kim and Huh, 2002b; Kim et al., 2000b), splitting errors can be introduced. The VODPK solver, because it can be used in very large systems, can be used for the full CMC equations without splitting. Hence, VODPK is main solver of CMC in this thesis without operator splitting. VODPK has also been used in DNS simulations (Frouzakis et al., 2002) and CMC modelling of heptane autoignition (Mastorakos and Wright, 2003) and lifted jet flames (Kim and Mastorakos, 2005).

2.4.2 Discretisation schemes

The CMC equations are discretised by finite differences in physical and mixture fraction space. Upwind differences (UDS) or central differences (CDS) blended by UDS are used for the convection term and central differences (CDS) for the diffusion term. Figure 2.14 shows an one dimensional CMC calculation with only the convection term active (i.e. no diffusion in the spatial and the mixture fraction space and no chemical reaction). The boundary conditions at $\eta=0$ and $\eta=1$ are specified according to the air and fuel composition and temperature. All other spatial boundaries treats as specifically given conditions such as inlet, outlet, wall...etc. in the CMC calculation.

Initially, a step temperature profile is given moving along the x direction in time. UDS and CDS show artificial diffusion compared to the exact solution. Large artificial diffusion is observed in UDS. CDS gives a more accurate profile and produces less artificial diffusion, but the solution has oscillations. The blended CDS by UDS profiles is tested and this provides a solution more stable than CDS and more accurate than UDS. The accuracy can be increased by refined grid spacing or by increasing the number of nodes, as shown in Figure 2.14.

The discretisation schemes are compared with an analytical solution for a convection-diffusion problem (Farlow, 1993) :

$$\phi(x,t) = \mathrm{erfc}\left(\frac{x-Ut}{2\sqrt{\mathcal{D}t}}\right) \tag{2.31}$$

where erfc is complementary error function. Fitting Eq. (2.31) to the calculated profiles results in an estimate for $\mathcal{D}$ which can be thought of as and

estimate of the magnitude of numerical diffusion. Figure 2.15 (a) shows the numerical diffusion coefficient by the convection discretisation using UDS and CDS. The UDS produces large numerical diffusion, while CDS produces less. The numerical diffusion increases with increased the grid spacing Δx and increases linearly by increasing velocity shown in Figure 2.15 (b). These results are important because they show that, if the spatial gradients of the conditional averages, are large, refined CMC grids are needed or the solution can suffer from numerical diffusion.

Figure 2.16 shows a typical example of flame propagation, where a hot region was initialised and the flame then expanded in the x-direction. All terms in the CMC equation are now active and this numerical experiment aims to demonstrate the nature of solution, obtained with the different discretisation schemes. The flow field is a constant velocity in the x-direction and details are given in Table 2.2. The mean mixture fraction $\tilde{\xi} = 0.0594$,

	Flow field	Species	Mass fraction
Mean velocity, U	10 m/s	CH_4	92.45 %
u'	0.1 m/s	CO_2	1.30 %
ℓ_{turb}	0.02 m	N_2	6.25 %
t_{turb}	0.02 s		Mixture fraction
k	1.5 m^2/s^2	$\widetilde{\xi}_{stoichiometry}$	0.0594
ε	91 m^2/s^3		
$\mathcal{D}_{turb}$	0.002 m^2/s		

Table 2.2: Initial conditions for the discretisation schemes.

the mixture fraction r.m.s. $\widetilde{\xi''} = 0.005$ and grid spacing $\Delta x = 0.008m$ are set. The blended CDS by UDS still produce the oscillation. The calculation of the 50% blended CDS can not perform further time steps because large

oscillations are produced. In the thesis, the UDS is used for the stability and the CMC calculation contains the numerical diffusion error because of UDS. The increase of computing grid nodes (or refinement of grids) or the use of higher order scheme is needed to reduce the numerical diffusion. The conditional mean quantities showed (Klimenko and Bilger, 1999) a slower variation in space than the unconditional averages and thus, one can opt for a coarse grid to calculate the conditional averages. However, the grid independence of the solution has not been checked in this work.

2.4.3 PDF calculation

The beta PDF seems to be the most accurate presumed PDF compared with the DNS. The problem of the beta PDF is that if the Gamma function $\Gamma(x)$ is zero (i.e. $I_b = 0$) in Eq. (2.21), $P(\eta) = 0$ everywhere in the mixture fraction space or delta function is set at the mean mixture fraction. I_b is a function of mean mixture fraction and its r.m.s.. I_b becomes zero when the mixture fraction r.m.s. is very small or the mean mixture fraction is at the boundaries (i.e. η=0 and 1). The beta PDF becomes singular when the function I_b is zero. If the above conditions occur in the beta PDF, then the Clipped Gaussian PDF is used in the CMC code. Figure 2.17 shows that the Clipped Gaussian PDF can capture the DNS very well at the critical condition ($I_b \approx 0$) of the beta PDF, which suggests that the transition from the beta PDF to the Clipped Gaussian PDF as $\widetilde{\xi''} \rightarrow 0$ is smooth.

2.4.4 Conditional scalar dissipation and other limits

The AMC and the Girimaji model for the conditional scalar dissipation rate have numerical errors when critical conditions are encountered. We have experienced that the CMC solver can not proceed when $\langle N|\eta\rangle_{max} > 1\times10^{+8}$. The AMC model is used when $0.001 < \tilde{\xi} < 0.999$ and $\widetilde{\xi''} \geq 1\times10^{-4}$ and the Girimaji model is used when $\widetilde{\xi''} \geq 1\times10^{-5}$ and $P(\eta)$ is very small, otherwise we set $\langle N|\eta\rangle = 0$. The limits have been established by trial and error. The same condition of the conditional scalar dissipation rate is applied to the spatial convection and diffusion terms.

Devaud and Bray (2003) suggests that the cut-off values are used in the CMC calculation when the PDF is $P(\eta) \leq 10^{-20}$. The cut-off limit is based on the fact that the rich mixture fraction zones are physically unrealizable and do not contribute significantly to any unconditional mean statistics.

Figure 2.18 shows the comparison of the CMC temperature equation terms (Eq. 2.18) and presents two different cut-off cases: a cut-off if $P(\eta) \leq 10^{-20}$ and a cut-off on the spatial terms. The conditional scalar dissipation rate is already limited by the presumed PDF, the mean mixture fraction and the mixture fraction r.m.s. in mixture fraction space. If the cut-off by PDF is imposed again on the CMC values then some information may be lost. The reaction rate and the molecular diffusion is allowed to propagate in mixture fraction space, but the quantity should not contribute to the unconditional averages. The test case is a lifted H_2 jet (Kim and Mastorakos, 2005). Figure 2.18 (a) is close to the lift-off height and the two limit methods give small differences (the cut-off occurs around $\eta = 0.35$ by the PDF limit). Further

downstream, the differences are bigger in molecular diffusion and convection, but smaller in diffusion. The chemistry reaction terms are the same as in Figure 2.18 (b). Figure 2.19 shows that the conditional temperature shows very small differences around $\eta = 0.3$ and a similar small difference in the unconditional averages is expected. If there are no cut-off limit in the mixture fraction space or the physical space, unexpected flame propagation is observed in the lifted flames. The flame always propagates upstream and results in an attached flame even in very high velocity with no cut-off limits. Hence, we conclude that the CMC equation should not be solved when the PDF$\rightarrow$ 0. The present strategy of (i) setting $\langle N|\eta\rangle = 0$ and (ii) not including the spatial transport terms if PDF$\rightarrow$0 seems to go around this problem.

2.4.5 Interface between CFD grid and CMC grid

A coarse spatial grid can be used in CMC since the conditional mean quantities have weaker spatial dependence than unconditional quantities (Klimenko and Bilger (1999)). The interface between a fine CFD grid and a coarse grid CMC is shown in Figure 2.20. The black colour thin line represents a fine grid CFD and the red colour thick line shows the coarse CMC grid.

A commercial CFD code 'FLUENT' is used and the flow information such as $\tilde{u}_i$, $\tilde{\xi}$, $\widetilde{\xi''^2}$, $\mathcal{D}_t$, $\tilde{\chi}$ must be provided so that $\langle u_i|\eta\rangle$, $\langle u_i''\phi''|\eta\rangle$ and $\langle N|\eta\rangle$ are available at the coarse CMC grid. Two methods are used to input the CFD quantities into the CMC code. In the first, the above quantities are taken from the CFD grid (with interpolation if necessary) at the exact physical location of the CMC grid node. In the second, a spatial average over the

CFD cells surrounding the CMC node is calculated including a weighting by $\tilde{P}(\eta)$:

$$\phi^*_{CMC} = \frac{\oint_{CFD} \phi P(\eta) dV}{\oint_{CFD} P(\eta) dV} \tag{2.32}$$

where ϕ denotes the conditional velocity, turbulent flux or scalar dissipation rate. This local integration procedure has the correct limiting behaviour for large volumes, i.e. recovers the homogeneous CMC of Klimenko and Bilger (1999), and reduces to the first, more straightforward, method if the CMC and the CFD grids are identical. Figure 2.21 shows the comparison between the two methods to take the CMC value from CFD. The test case is a lifted H_2 jet (Kim and Mastorakos, 2005) at the lift-off height that will be described in Chapter 4. Figure 2.21 (a) shows the radial profiles of mean species mole fractions and Figure 2.21 (b) shows a balance of terms in mixture fraction space of the CMC temperature equation in Eq.(2.18). Very small differences between these two methods are observed, which is also a manifestation of the relatively fine grids used here and of the particular flow condition where the conditional averages were not varying a lot in space.

2.5 Conclusions

In this chapter, the CMC equations, validation of sub-models and numerical methods have been presented. In the validation of sub-models part, Table 2.3 summarizes the most accurate models: the beta PDF for the mixture fraction and the linear model for the conditional velocity are the most accurate compared with the DNS. The beta PDF can not apply when the Gamma

function (I_b) approaches zero and then the Clipped Gaussian PDF is used. The linear model for the conditional velocity shows discrepancies where $|\eta - \tilde{\xi}|$ is large. The Girimaji model for the conditional scalar dissipation rate shows better predictions in homogeneous mixtures and the AMC model is better in inhomogeneous mixture with beta PDF. The gradient diffusion model for the conditional fluxes gives good agreements in inhomogeneous case, but not in homogenous.

For the ODE solvers, three different stiff/nonstiff solvers have been presented. VODPK is chosen as the main solver for CMC in this research because it allows transformation of the PDE's into a set of ODE's which can avoid the splitting errors. Finite difference discretisation methods (UDS and CDS) in physical and mixture fraction space are used. Numerical diffusion is large in UDS and small in CDS, however, the CDS generates unrealistic oscillations. The calculation limit by PDF proposed by Devaud and Bray (2003), seems to be too steep and cuts off information in mixture fraction space. Limiting conditions on the conditional scalar dissipation rate in mixture fraction space and on the spatial space are used and produce similar effect. Hence, we do not solve the CMC equation if $\widetilde{\xi} \leq 0.001$, $\widetilde{\xi} \geq 0.999$ or $\widetilde{\xi''} < 1 \times 10^{-4}$ with the AMC model and $\widetilde{\xi} < 1 \times 10^{-5}$ or very small $P(\eta)$ value with the Girimaji model.

A commercial CFD code 'FLUENT' is used to provide the flow information into the CMC calculation. The CFD and CMC are not coupled therefore heat generation from dynamic field changes by density changes is not included, which can cause reduction in accuracy. However, combustion models in FLUENT will be used for the calculation. Two methods of inter-

face between CFD grid and CMC grid, exact physical location of the CMC grid node and weighting by PDF on CFD grid, give very small differences.

Table 2.1 shows some important applications of CMC calculations and present the trend of CMC modelling, which currently moves toward more complex applications involving local extinction/re-ignition and higher order/doubly conditioning. The following chapters present the application of the elliptic first order CMC for an attached jet flame, a lifted jet flame and opposed jet flames and suggest the limit and ability of the first order of CMC for a variety of non-premixed combustion problems. As evident from Table 2.1, some of these problems have not been analysed before with CMC.

	Homogeneous	Inhomogeneous
Presumed PDF	beta PDF +Clipped Gaussian PDF	beta PDF +Clipped Gaussian PDF
$\langle u\|\eta\rangle$	Linear model	Linear model PDF gradient model with right PDF
$\langle N\|\eta\rangle$	Girimaji	AMC with beta PDF
$\langle u''\phi''\|\eta\rangle$		Gradient diffusion

Table 2.3: The most accurate model, as found by comparison with DNS.

2.6 Figures

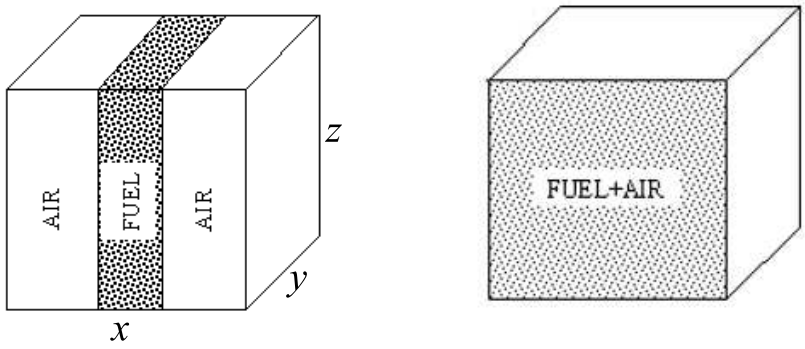

(a) Sandwich, Re=175 (b) Spectrum, Re=100

Figure 2.1: Schematic of the initial fuel distributions in (a) inhomogeneous and (b) homogeneous (in the mean) DNS. In (b), initial scalar fluctuations were introduced by inverting a spectrum.

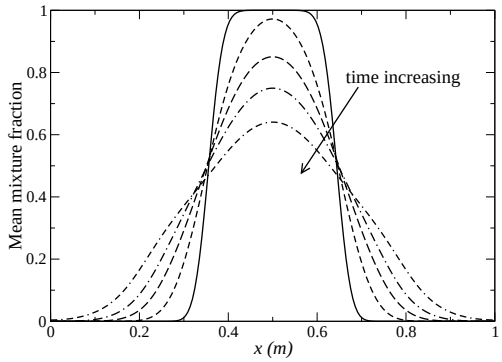

(a) Mean mixture fraction

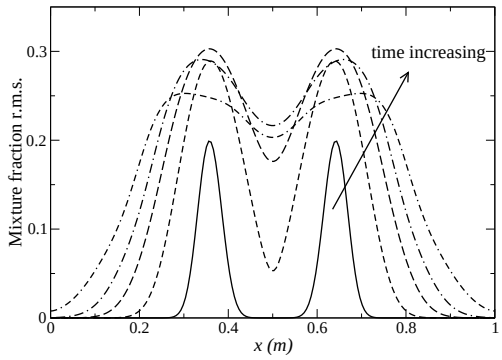

(b) Mixture fraction r.m.s.

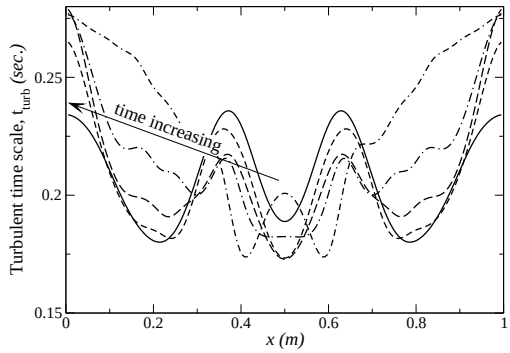

(c) Turbulent time scale

Figure 2.2: Mean mixture fraction, mixture fraction r.m.s. and turbulent time scale (k/ε) of the inhomogeneous DNS case.

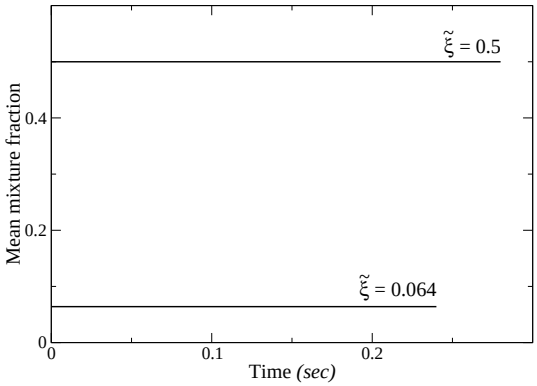

(a) Mean mixture fraction

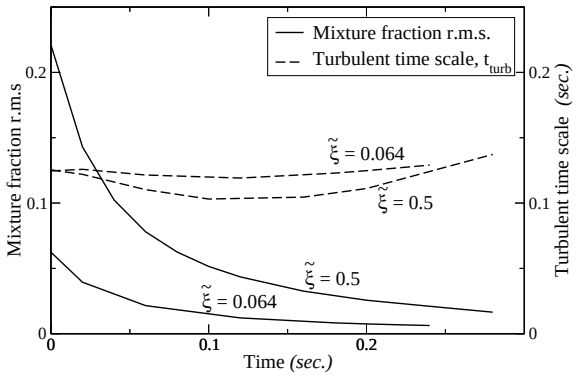

(b) Mixture fraction r.m.s. and turbulent time scale

Figure 2.3: Mean mixture fraction, mixture fraction r.m.s. and turbulent time scale (k/ε) of the homogeneous DNS cases.

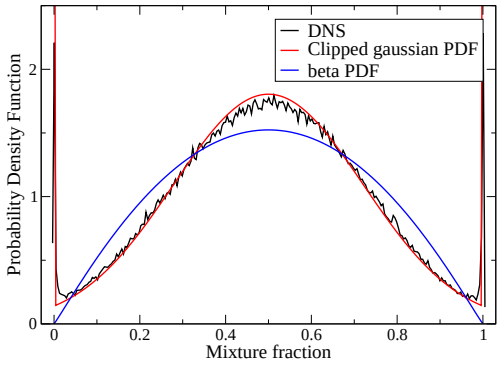

(a) $\tilde{\xi} = 0.5,\ \widetilde{\xi''} = 0.22$

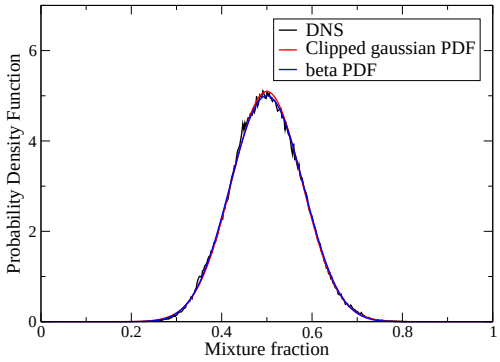

(b) $\tilde{\xi} = 0.5,\ \widetilde{\xi''} = 0.078$

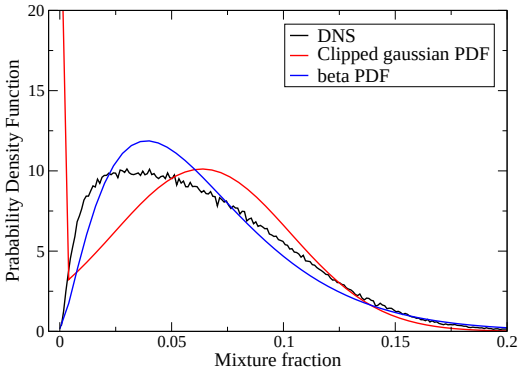

(c) $\tilde{\xi} = 0.064,\ \widetilde{\xi''} = 0.0394$

Figure 2.4: Comparison of PDF shape for (a) $\tilde{\xi} = 0.5,\ \widetilde{\xi''} = 0.22$, (b) $\tilde{\xi} = 0.5,\ \widetilde{\xi''} = 0.078$ and (c) $\tilde{\xi} = 0.064,\ \widetilde{\xi''} = 0.0394$ with the DNS data for the homogeneous case.

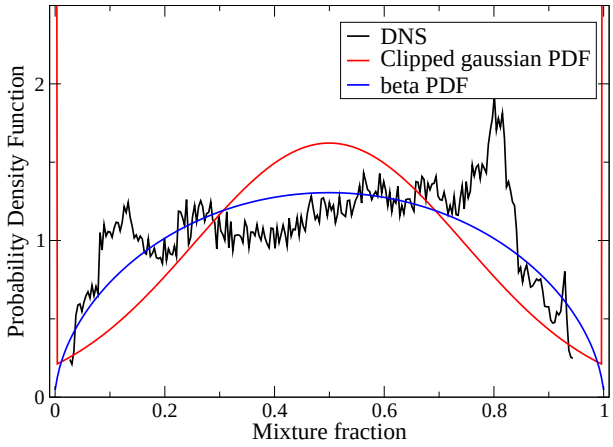

(a) $\tilde{\xi} = 0.5,\ \widetilde{\xi''} = 0.246$

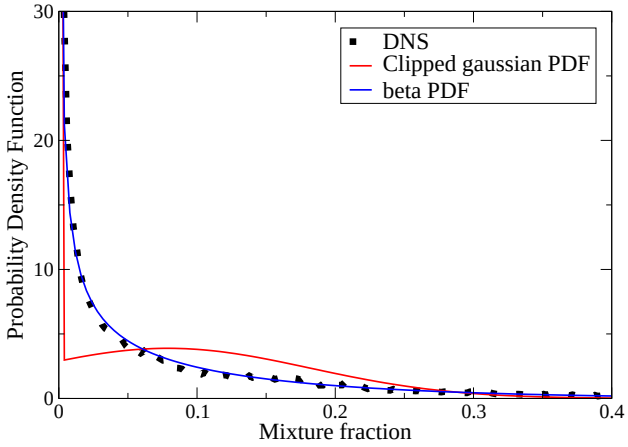

(b) $\tilde{\xi} = 0.0655,\ \widetilde{\xi''} = 0.0908$

Figure 2.5: Comparison of the PDF shape for (a) $\tilde{\xi} = 0.5,\ \widetilde{\xi''} = 0.246$ and (b) $\tilde{\xi} = 0.0655,\ \widetilde{\xi''} = 0.0908$ with the DNS data for the inhomogeneous case.

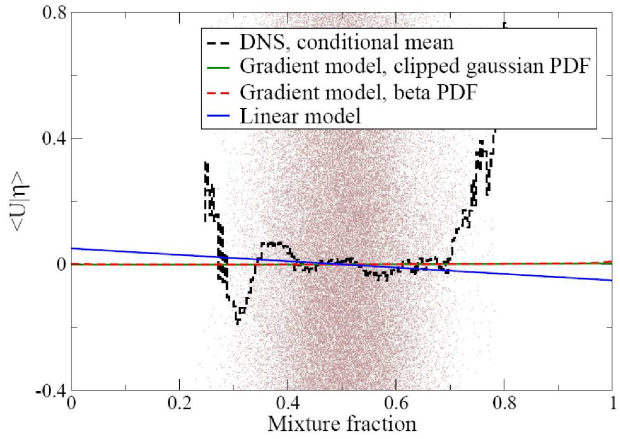

(a) $\tilde{\xi} = 0.5,\ \widetilde{\xi''} = 0.078$

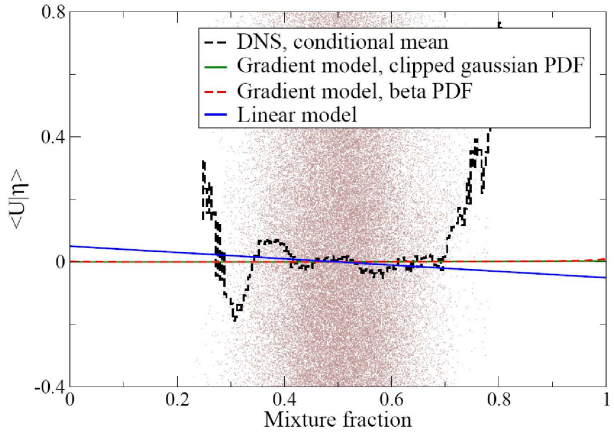

(b) $\tilde{\xi} = 0.5,\ \widetilde{\xi''} = 0.014$

Figure 2.6: Homogeneous case, conditional velocity model comparison. Scatter plots are the DNS data.

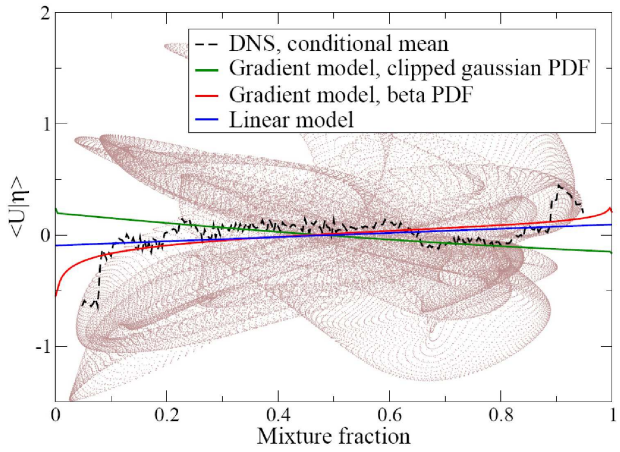

(a) $\tilde{\xi} = 0.5,\ \widetilde{\xi''} = 0.246$

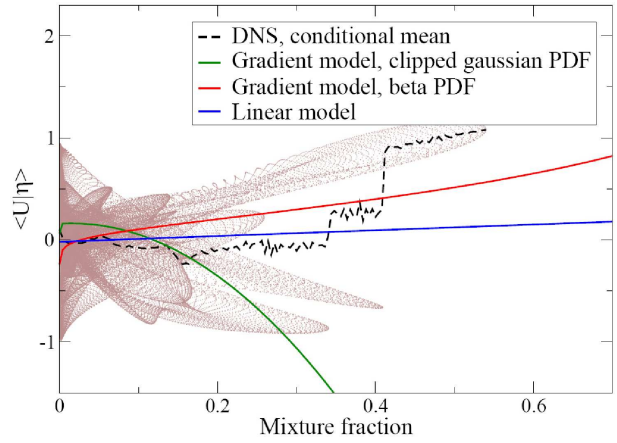

(b) $\tilde{\xi} = 0.0655,\ \widetilde{\xi''} = 0.0908$

Figure 2.7: Inhomogeneous case, conditional velocity model comparison. Scatter plots are the DNS data.

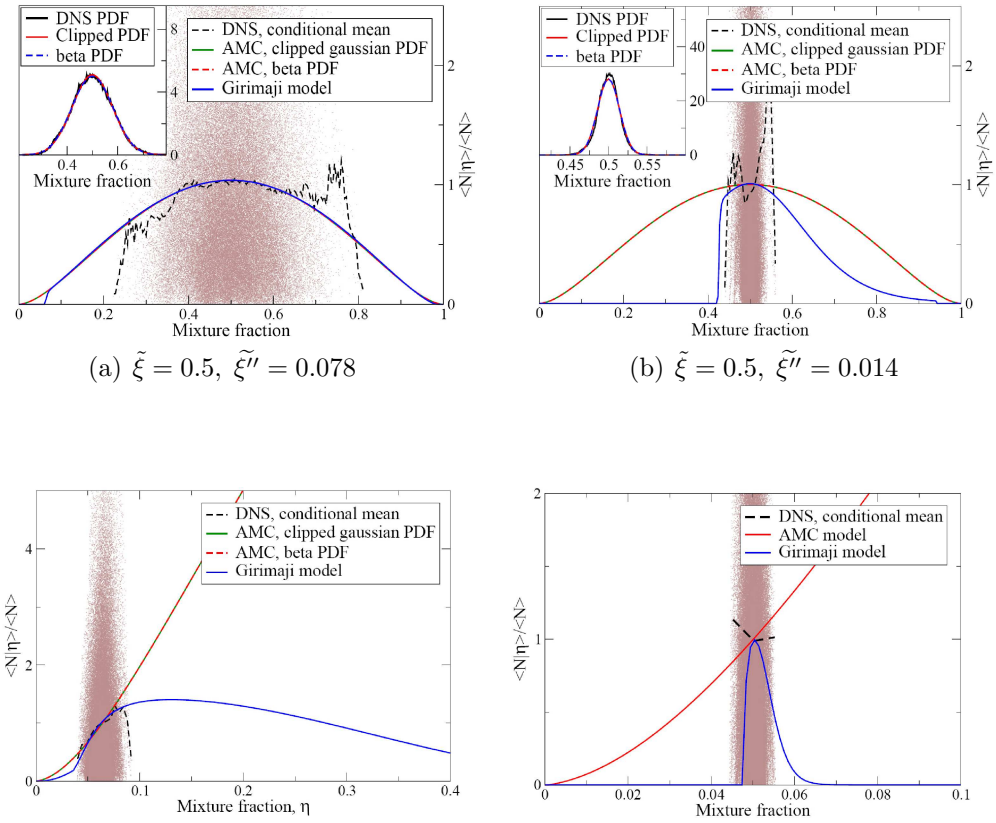

(a) $\tilde{\xi} = 0.5,\ \widetilde{\xi''} = 0.078$ (b) $\tilde{\xi} = 0.5,\ \widetilde{\xi''} = 0.014$

(c) $\tilde{\xi} = 0.064,\ \widetilde{\xi''} = 0.0075$ (d) $\tilde{\xi} = 0.05,\ \widetilde{\xi''} = 0.0014$

Figure 2.8: Homogeneous case, normalised conditional scalar dissipation.

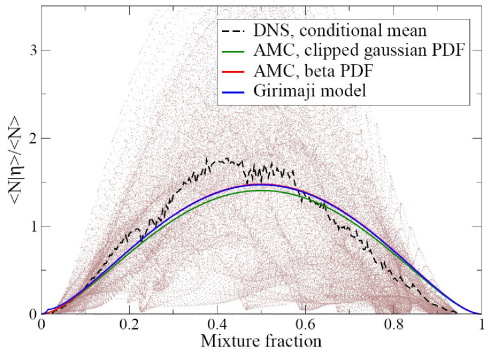

(a) $\tilde{\xi} = 0.5,\ \widetilde{\xi''} = 0.246$

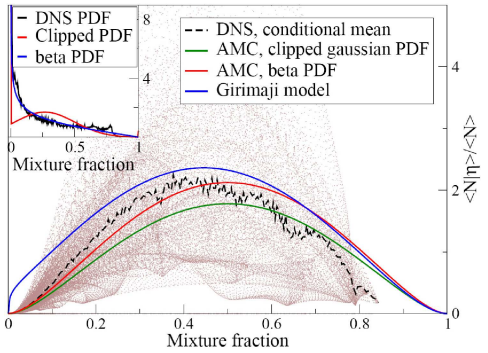

(b) $\tilde{\xi} = 0.309,\ \widetilde{\xi''} = 0.2467$

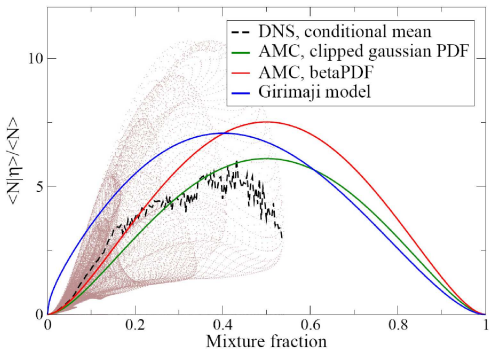

(c) $\tilde{\xi} = 0.0655,\ \widetilde{\xi''} = 0.0908$

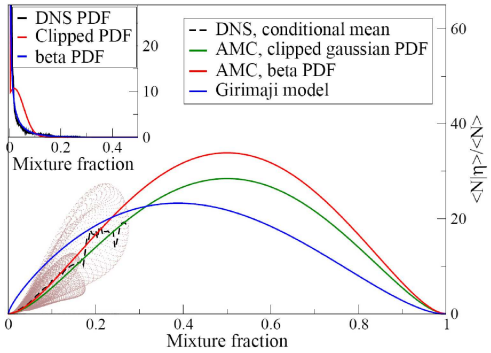

(d) $\tilde{\xi} = 0.029,\ \widetilde{\xi''} = 0.0526$

Figure 2.9: Inhomogeneous case, normalised conditional scalar dissipation.

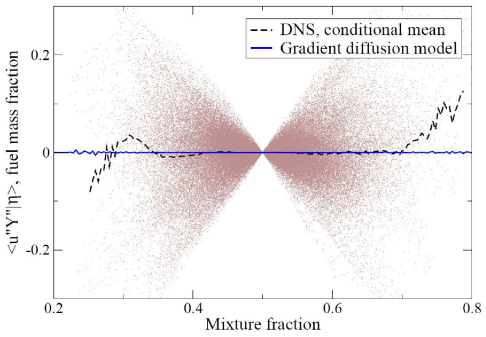

(a) $\langle u''Y''_{fuel}|\eta\rangle,\ \tilde{\xi}=0.5,\ \widetilde{\xi''}=0.078$

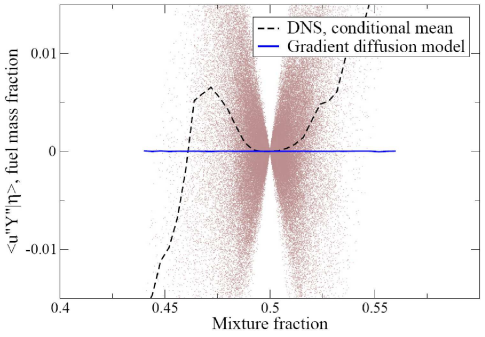

(b) $\langle u''Y''_{fuel}|\eta\rangle,\ \tilde{\xi}=0.5,\ \widetilde{\xi''}=0.014$

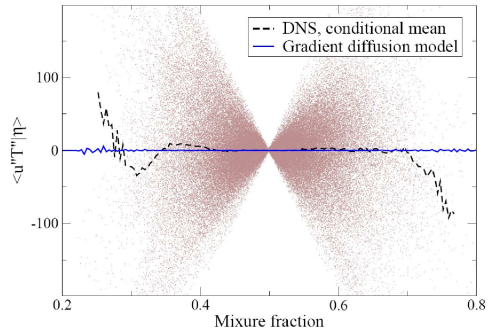

(c) $\langle u''T''|\eta\rangle,\ \tilde{\xi}=0.5,\ \widetilde{\xi''}=0.078$

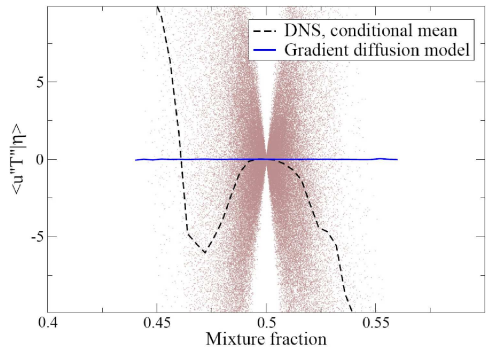

(d) $\langle u''T''|\eta\rangle,\ \tilde{\xi}=0.5,\ \widetilde{\xi''}=0.014$

Figure 2.10: Homogeneous case, conditional fluxes (a) and (b) for $\langle u''Y''_{fuel}|\eta\rangle$, (c) and (d) for $\langle u''T''|\eta\rangle$.

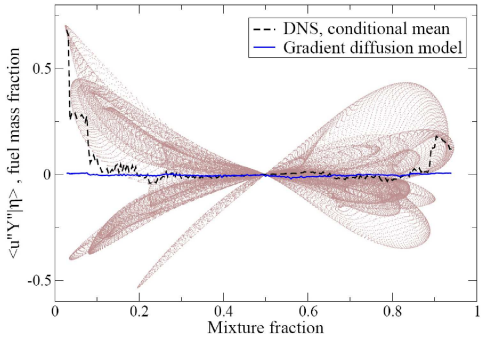

(a) $\langle u''Y''_{fuel}|\eta\rangle,\ \tilde{\xi}=0.5,\ \widetilde{\xi''}=0.246$

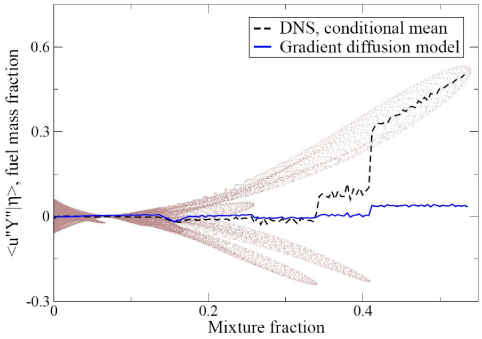

(b) $\langle u''Y''_{fuel}|\eta\rangle,\ \tilde{\xi}=0.0655,\ \widetilde{\xi''}=0.0908$

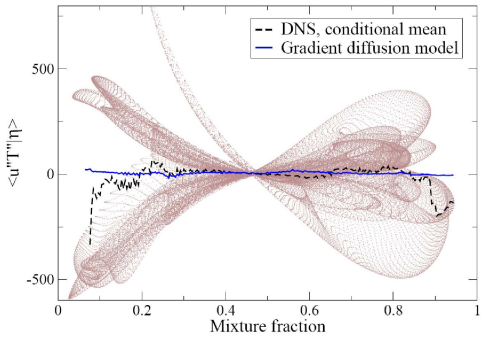

(c) $\langle u''T''|\eta\rangle,\ \tilde{\xi}=0.5,\ \widetilde{\xi''}=0.246$

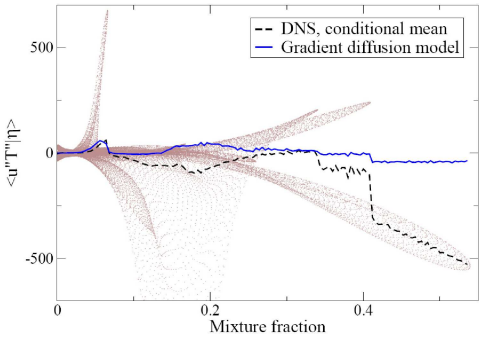

(d) $\langle u''T''|\eta\rangle,\ \tilde{\xi}=0.0655,\ \widetilde{\xi''}=0.0908$

Figure 2.11: Inhomogeneous case, conditional fluxes (a) and (b) $\langle u''Y''_{fuel}|\eta\rangle$, (c) and (d) $\langle u''T''|\eta\rangle$.

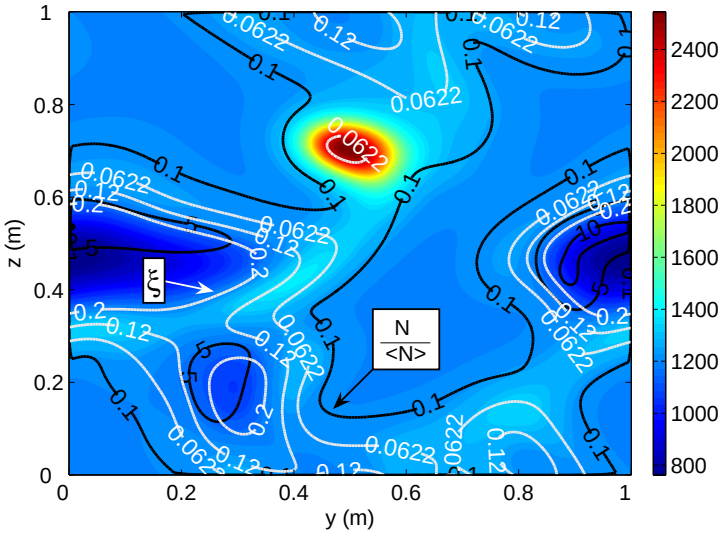

Figure 2.12: Inhomogeneous case for DNS, iso-lines of instantaneous mixture fraction and normalised instantaneous scalar dissipation rate by its mean scalar dissipation rate superimposed. $\tilde{\xi}$=0.0655, $\widetilde{\xi''}$=0.0908. The white line is for the instantaneous mixture fraction and the black line is for the normalised instantaneous scalar dissipation rate.

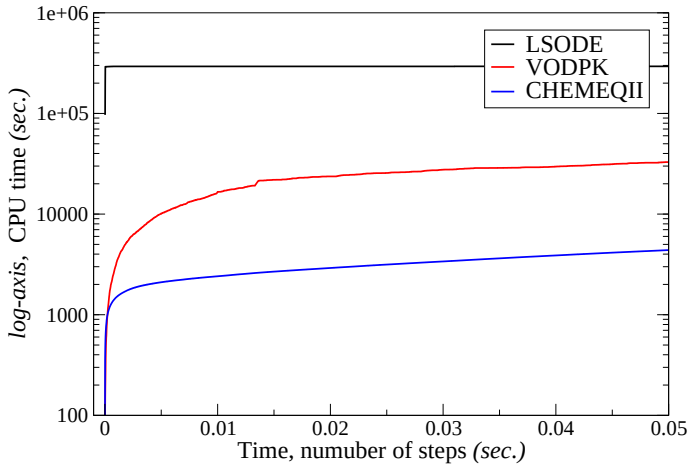

Figure 2.13: ODE solvers comparison of CPU time versus number of steps ; LSODE, VODPK and CHEMEQII, for a CMC0D code and natural gas combustion.

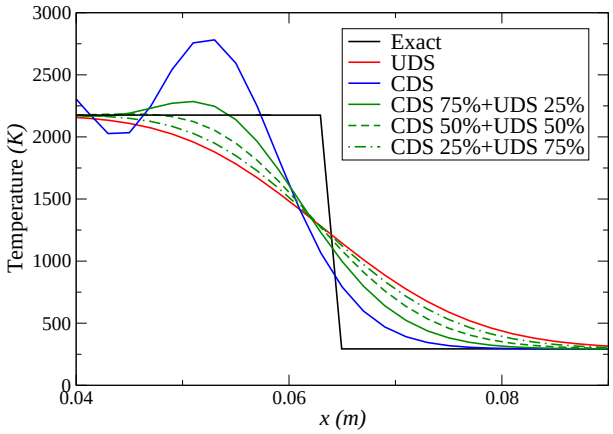

(a) $\Delta t = 5 \times 10^{-5}$, $\Delta x = 0.002$ and $t = 0.06$ *sec*

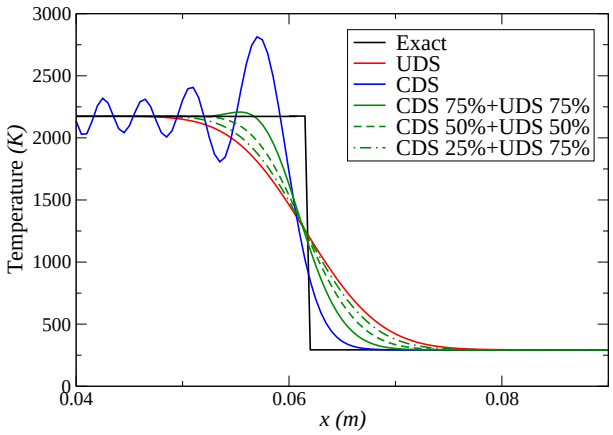

(b) $\Delta t = 5 \times 10^{-5}$, $\Delta x = 0.0005$ and $t = 0.06$ *sec*

Figure 2.14: Comparison of convection by UDS and CDS, $velocity = 1m/s$ and $density = 1kg/m^3$ for a one-dimensional traveling sharp profile.

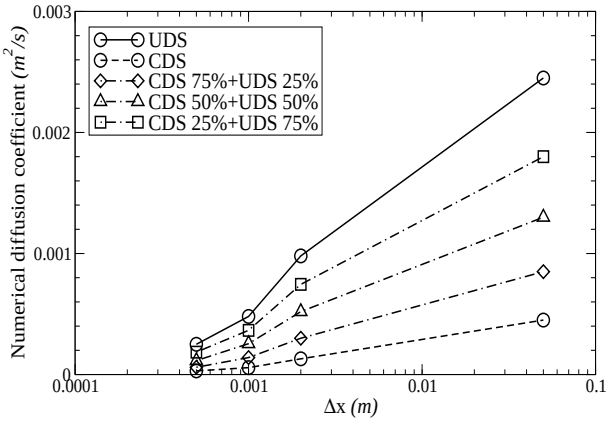

(a)

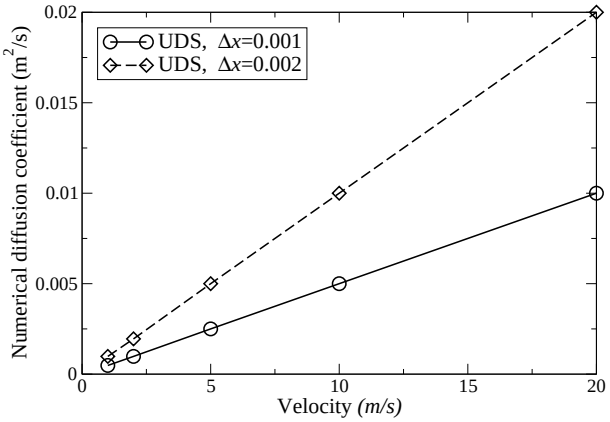

(b)

Figure 2.15: Numerical diffusion caused by the discretisation scheme, (a) Grid space dependence $\Delta t = 5 \times 10^{-5}$, $velocity = 1m/s$ and $density = 1kg/m^3$, (b) Velocity dependence.

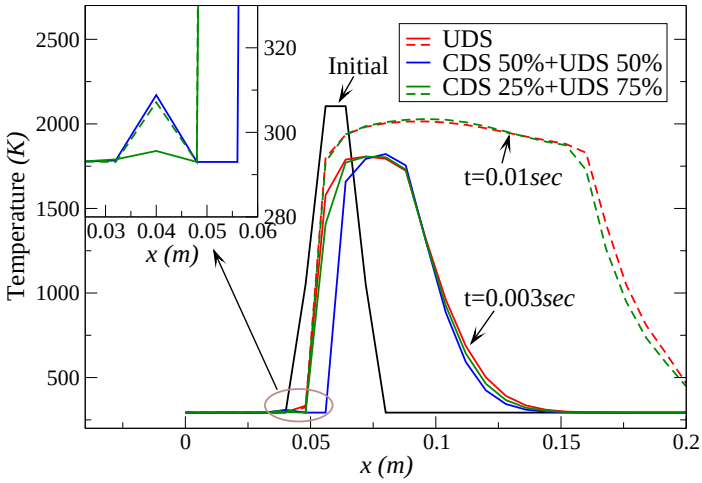

Figure 2.16: Comparison of UDS and CDS for a one-dimensional CMC, flame propagates in the x-direction.

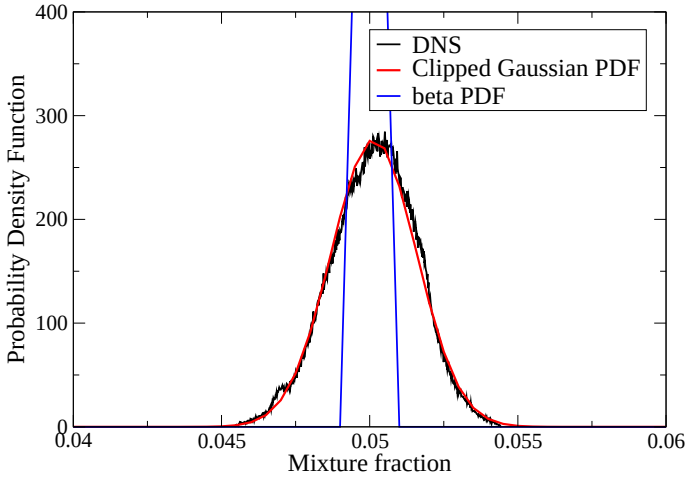

Figure 2.17: DNS vs. Clipped Gaussian PDF comparison, $\tilde{\xi} = 0.05$ and $\widetilde{\xi''} = 0.0014$ results in a delta function of the beta PDF due to numerical problems with $I_b \approx 0$.

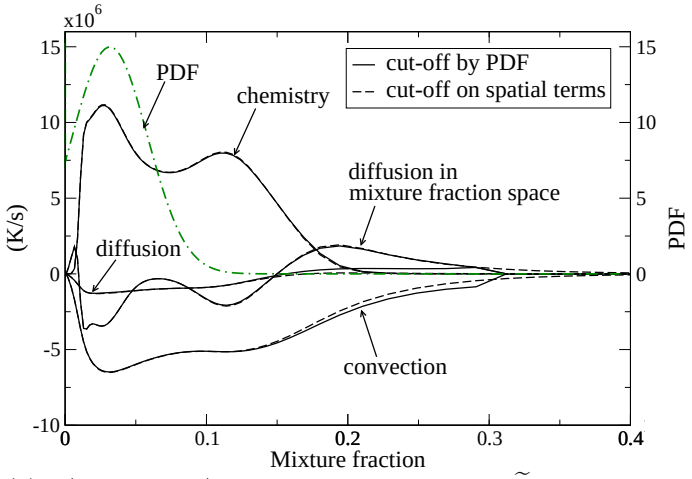

(a) r/D=2.33, x/D=9.8 at lift-off height. $\widetilde{\xi} = 0.031$ and $\widetilde{\xi''} = 0.02604$

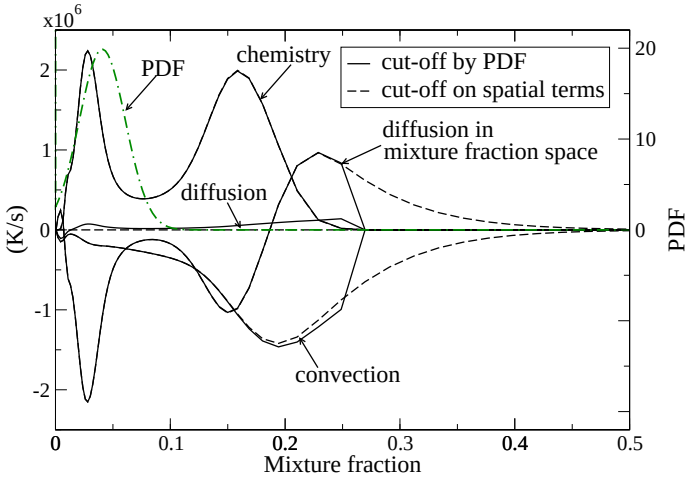

(b) r/D=2.33, x/D=18.4, $\widetilde{\xi} = 0.0402$ and $\widetilde{\xi''} = 0.02003$

Figure 2.18: Comparison of source terms in the temperature CMC equation by various limiting methods.

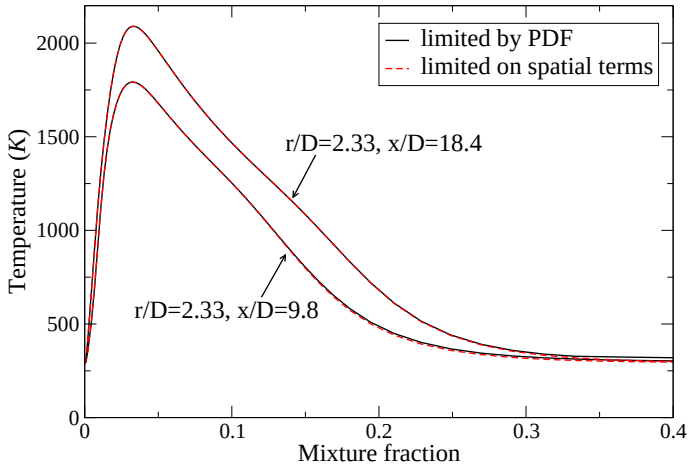

Figure 2.19: Comparison of the conditional temperatures in two simulations by two different cut-off limits.

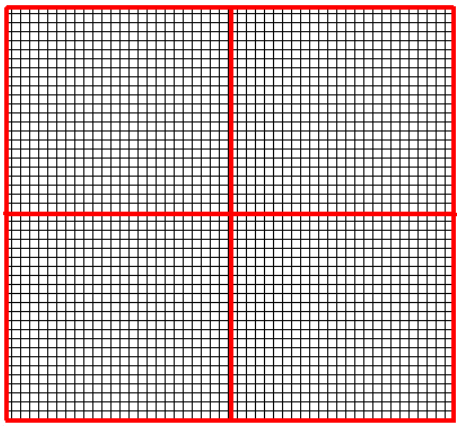

Figure 2.20: A fine grid of CFD (black thin line) and a coarse grid of CMC (red thick line).

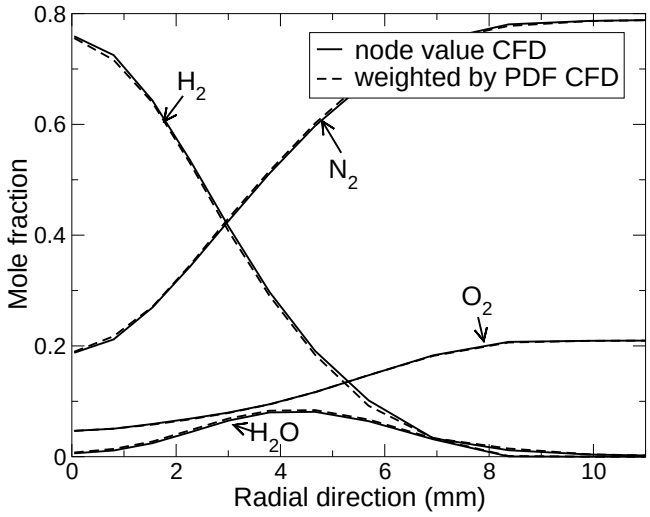

(a) Species in radial direction

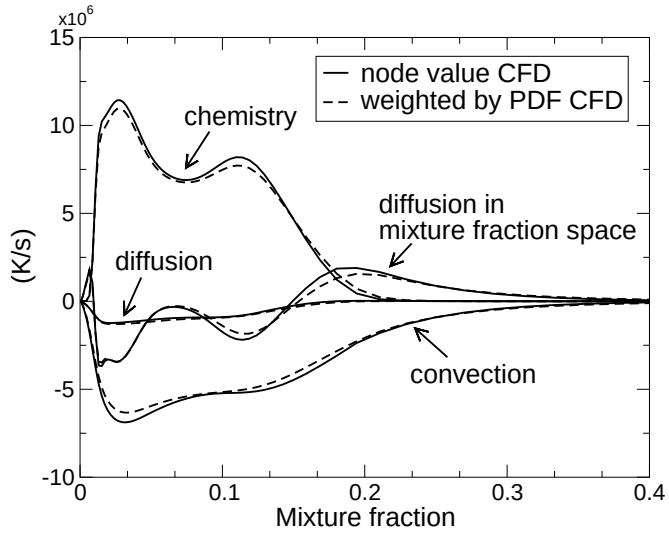

(b) CMC terms in mixture fraction space

Figure 2.21: Comparison between methods of taking CFD information to the CMC code.

Chapter 3

Piloted natural gas jet diffusion flame

In this Chapter, a simulation of CMC for an attached piloted jet diffusion flame is discussed.

3.1 Background

Smith et al. (1992) investigated the CMC model for non-premixed hydrogen jet flames and presented accurate NO_x emissions far from extinction. Smith et al. (1995) studied NO prediction and compared CMC and PDF methods. Both models gave reasonable prediction and suggested that the differential diffusion in the upstream and radiation in downstream regions are significant. Fairweather and Woolley (2003) with cross-stream averaged (one-dimensional) CMC showed that the predictions of major and minor species and temperature of hydrogen jet flames are in reasonable agreement

with experimental data, but gave an underprediction of NO with the first order CMC. Roomina and Bilger (2001) also presented good prediction of species of a methane-air jet flame with cross-stream averaged CMC. However, large errors in species predictions were found on the fuel rich side and in the prediction of NO.

Bradley et al. (2002) studied methane-air piloted-jet flames by laminar flamelets model combined with CMC and second order closure to evaluate a joint PDF of progress variable and mixture fraction. Major species (CH_4, O_2 and H_2O) were in good agreement, but large differences were found in intermediate species. Kim and Huh (2004) presented methane-air piloted jet diffusion flames with one dimensional and second order CMC. The second order correction was only considered for one selected chain-branching step, $H + O_2 \rightarrow OH + O$. Improved results compared with the first order CMC were presented, but large discrepancies of intermediate species were observed where local extinction were severe and multi-step second order corrections were suggested to improve the prediction.

In this Chapter, first order CMC is used for an attached diffusion flame which contains local extinction in order to show the extent to which the first order CMC can capture such phenomena. This simulation presents the discrepancy of the first order CMC and suggests the need of double conditional moment or second order CMC as suggested previous studies (Roomina and Bilger, 2001; Fairweather and Woolley, 2003; Kim and Huh, 2004). The particular flame examined here has not been modelled before with CMC, as far as I am aware, and the use of a two-dimensional CMC formulation for such flames is novel.

The Chapter is organised as follows. Firstly, the natural gas jet (piloted) flame is described and the details of computed flow profiles from a commercial CFD code is presented. The chapter closes with a discussion of results and the conclusion drawn by examining CMC calculations.

3.2 Delft III piloted natural gas flame

The experiment of Delft III piloted natural gas flame was performed as part of an International Workshop on Measurement and Computation of Turbulent Nonpremixed Flames. The experimental data were obtained from *http://www.ca.sandia.gov/TNF* and Nooren et al. (2000).

3.2.1 Experimental configuration

The burner consists of a central fuel jet, surrounded by two concentric coflows of air. Figure 3.1 shows the geometry of the Delft pilot head. The fuel jet nozzle is $6mm$ in diameter and the annulus is for the air supply. Its inner diameter is $15mm$ and outer diameter is $45mm$ at the exit. The pilot is located between the fuel jet and the annulus to stabilise the flame on the burner. The pilot consists of 12 holes ($0.5mm$ in diameter, located on a ring $7mm$ in diameter) and a premixture of $C_2H_2/H_2/air$. The pilot flames are rich with equivalence ratio $\Phi = 1.4$.

The inner diameter of the primary air annulus is initially $30mm$, decreasing to $15mm$ in the final $6mm$. This gives rise to a small negative radial velocity component of the primary air in the exit plane of the annulus. The burner is placed in a chamber $0.9m$ long with square cross-section of side

$0.57m$.

The inlet conditions are shown in Table 3.1 and the inlet stream is at room temperature ($295K$). The natural gas composition is shown in Table 3.2.

	Fuel	Pilot	Primary air	secondary air
Velocity (m/s)	21.9	12	4.4	0.3

Table 3.1: Delft piloted flame inlet conditions

Constituent	Formula	Mass fraction (%)	Mole fraction (%)
methane	CH_4	69.97	81.29
ethane	C_2H_6	4.63	2.87
propane	C_3H_8	0.90	0.38
butane	C_4H_{10}	0.47	0.15
pentane	C_5H_{12}	0.16	0.04
hexane	C_6H_{14}	0.23	0.05
nitrogen	N_2	21.52	14.32
oxygen	O_2	0.02	0.01
carbon dioxide	CO_2	2.10	0.89

Table 3.2: Delft piloted flame natural gas composition

3.2.2 Flow field

The flow field information is calculated by a commercial CFD software, FLUENT. The computational domain is two-dimensional axisymmetric with length $0.9m$ and radius $0.285m$. The grid nodes are 420×200 in the axial and radial direction respectively, a resolution which is fine enough to compute grid independent solutions. The boundary conditions for the FLUENT calculations are taken as inlet-flow, out-flow, wall and axisymmetry.

The inlet-flow conditions are specified fully as developed pipe flow profile, which is pre-calculated by the 1/7th power law for axial velocity, $u_x = u_{x,axis}(y/\delta)^{1/7}$ where δ is the pipe radius, $u_{x,axis}$ is the axial velocity at the centre line of the pipe and y is the coordinate. The turbulent kinetic energy k and the dissipation rate ε is also pre-calculated as input and given by (FLUENT, 2003; Pope, 2000) :

$$\begin{aligned} k_{nw} &= \frac{u_\tau^2}{\sqrt{C_\mu}}, \quad k_{axis} = 0.002u_{axis}^2, \quad \varepsilon = \frac{C_\mu^{3/4}k^{3/2}}{l} \\ u_\tau &= \sqrt{\tau_w/\rho}, \quad \text{with} \quad \tau_w = \frac{f\rho u_{axis}^2}{2}, \quad f = 0.045\frac{u_{axis}\delta^{-1/4}}{\nu} \end{aligned}$$

where k_{nw} is for near-wall, k_{axis} is for the centre line of the pipe and C_μ is assumed as 0.09. The mixing length l is the minimum of κy and 0.085δ with the von Karman constant $\kappa = 0.41$ (FLUENT, 2003). u_τ is the friction velocity and τ_w is the wall shear. The resultant axisymmetric inlet profiles for the jet are shown in Figure 3.2. The inlet condition for the pilot, primary air and secondary air are also calculated as fully developed pipe flow. Axisymmetry condition requires that the velocity component normal to the axis is zero and the radial gradients of all variables are also zero. The outflow condition at the exit of the flow is based on zero normal gradient for all components, except pressure.

The Smooke mechanism (Smooke et al., 1986) for methane combustion is used in the flamelet calculation in FLUENT and consists of 17 species and 46 reversible reactions. The Smooke mechanism does not support all the fuel compositions on Table 3.2. Hence, the fuel composition has been re-

distributed into other species. The total calorific value is calculated using the lower heating values of all constituents. Table 3.3 shows the fuel composition of FLUENT that gives the stoichiometric mixture fraction as $\xi_{st} = 0.0713853$, while the natural gas in the experiment gave $\xi_{st} = 0.0714734$. The fuel composition for CMC is also re-distributed in the same manner used here, as discussed in Section 3.3.1. The mean mixture fraction of the pilot flames is calculated by the equivalence ratio ($\Phi = 1.4$) from the re-distributed fuel composition.

Constituents	Formula	Mass fraction (%)
methane	CH_4	75.98
nitrogen	N_2	21.92
carbon dioxide	CO_2	2.10

Table 3.3: FLUENT fuel composition for Delft flame

Figure 3.3 shows the comparison of the air jet (i.e. no combustion) with experiment and good agreement is found. The air jet of this experiment is tested with the $k-\varepsilon$ turbulent model with a model constant $C_{\varepsilon 2} = 1.77$, which is suggested for jet flows by Pope (2000). The $k-\varepsilon$ model can predict an inert flow accurately as seen in Figure 3.3.

The flamelet non-premixed combustion model in FLUENT is used firstly with $Sc = 0.7$ and $C_{\varepsilon 2} = 1.77$ (standard coefficients) in the Reynolds stress model (RSM) and $k-\varepsilon$ model. In Figure 3.4, the k–ε model over-predicts the turbulent kinetic energy. The Reynolds stress model shows good agreement with the experiment. Therefore, the Reynolds stress model with flamelet non-premixed combustion model provides the flow field information to CMC for the Delft piloted diffusion flame. The use of the flamelet model is that

the model reduces the error from the heat generation from the dynamic field changes (density changes) and provides accurate flow field information of reacting flow for the CMC calculation.

Figure 3.5 shows that the Reynolds stress model with standard coefficients predicts a slower rate of mixing, but also that decreasing Sc number results in faster mixing and a modified set of coefficients provides good agreement with $Sc = 0.4$, $C_D = 1.3$ (C_D is given in Eq. (1.40)) and $C_{\varepsilon 2} = 1.8$. The modified coefficients will be used for the flow field calculation. Figure 3.6 and Figure 3.7 present the axial velocity along the axis and radial direction and it is evident that both the standard and modified coefficient models show good agreement with the experiment. Figure 3.8 presents the mean mixture fraction and mixture fraction r.m.s. along the radial directions and shows that the mixture fraction profile is little broader than the experiment, but the computed profile captures the experiment reasonably well.

The computed flow field information is provided into CMC and the results are presented in the next Section.

3.3 Results and discussion

In this Section, the numerical method and the results from the CMC model are presented for the piloted jet flame.

3.3.1 Numerical methods

The first order CMC calculation has been performed with the GRI-v3.0 (Smith et al., 1999) mechanism. Two dimensional axisymmetric CMC code

described in Chapter 2 is applied with 26×20 spatial nodes and 71 nodes in mixture fraction space. The total number of ODE's is $2,030,600$ and VODPK (Byrne, 1992) is used for their solution. The inlet conditions for the fuel nozzle, the pilot and the air flows are input as frozen, burning and frozen conditions respectively.

The GRI-v3.0 mechanism has 53 species but it can not cover all species in the experiment, for example Butane (C_4H_{10}), Pentane (C_5H_{12}) and Hexane (C_6H_{14}) are not present in GRI-v3.0. The fuel composition of CMC and FLUENT calculations have been re-distributed into other species. The total calorific value calculated by the individual low heating values is matched and Table 3.4 shows the fuel composition of CMC. The stoichiometric mixture fraction of CMC is $\xi_{st} = 0.0714747$.

Constituents	Formula	Mass fraction (%)
methane	CH_4	70.013
acetylene	C_2H_2	0.0695
ethane	C_2H_4	0.289
ethane	C_2H_6	4.873
propane	C_3H_8	1.1155
nitrogen	N_2	21.54
carbon dioxide	CO_2	2.10

Table 3.4: CMC fuel composition for Delft flame.

3.3.2 Results

Figure 3.9 shows the mean temperature contours with iso-lines of the mean mixture fraction and normalised conditional scalar dissipation rate at the

stoichiometric mixture fraction superimposed. The highest temperature appears on the rich side along the mean mixture fraction $\widetilde{\xi} \approx 0.15$, consistent with the experiment (Nooren et al., 2000), where the high temperature zone was along $\widetilde{\xi} \approx 0.15$. The quenching scalar dissipation rate at the stoichiometric mixture fraction is calculated by a homogeneous CMC (no spatial terms) and given as 22.03 s^{-1}. The iso-line contours of the quenching scalar dissipation rate show that the quenching scalar dissipation rate , $\frac{\langle N|\eta\rangle}{\langle N|\eta\rangle_{st,quench}} = 1$, is observed at the edge of the jet ($r = 0.003m$), hence the flame could not stay burning. The pilot flame provides the necessary heat to stabilise the flame, despite the high scalar dissipation rate at the nozzle. Numerically, this is achieved by the spatial transport terms in the CMC equation that provide cross-stream diffusion from the pilot ("burning flamelet") to the jet ("frozen flamelet").

In this experiment (Nooren et al., 2000), local extinction was observed. CFD and CMC calculations with different C_D values (appeared in the Section 2.2.3), that is expected to alter the predicted scalar dissipation, are examined to obtain the local extinction. However, increasing C_D values results in low scalar dissipation rate and could not produce the local extinction by high scalar dissipation rate. Figure 3.10 shows that an increase of C_D gives a decrease of scalar dissipation rate due to the large decrease of mixture fraction r.m.s.. The mean mixture fraction is not altered much by changing the C_D values and the turbulent kinetic energy/dissipation rate are also not altered very much, as seen in Figure 3.4. The result of using different C_D is that different presumed PDF shapes are predicted, as shown in Figure 3.11. In the simulation with increasing C_D values, increase of unconditional values

are expected and described in this Chapter. Increase of scalar dissipation rate by increase of C_D values in a counterflow flame is described in Chapter 5.

Conditional averages

The experimental scatter plots are measured across the flame at given axial locations in Figures 3.12 - 3.15, which also present CMC calculations with different scalar dissipation rate models, AMC and Girimaji models. Figure 3.12 shows the conditional temperature and H_2O mass fraction at $100mm$ axial location from the nozzle. The computed CMC profiles are taken at $\tilde{\xi} = 0.113$ and also the corresponding conditional scalar dissipation rate is shown at the inset. The differences between AMC and Girimaji models are very small and both give conditional scalar dissipation rate less than the extinction value. The wide scatter plots of the experiment is due to local extinction of the flame, therefore the first order CMC can not predict accurately this flame. However, the overall reasonable structure suggests that the CMC code is free of programming errors.

Figure 3.13 and Figure 3.14 show profiles at $100mm$ from the nozzle from various radial locations across the jet. The effect of increasing C_D values gives no big changes, but small increase of conditional temperature and H_2O mass fraction in the two different conditional scalar dissipation rate are observed in $\eta < 0.11$. Therefore, increase of C_D to capture the local extinction by changing scalar dissipation rate is not successful, it simply results in an increase of the products (temperature and H_2O mass fraction). It is also evident that at this axial location all radial positions give virtually

identical conditional averages.

Figure 3.15 shows the intermediate species, CO and H_2 across the stream at $150mm$ from the nozzle, calculated with different scalar dissipation rate models with $C_D = 1.3$ versus the experiment. There are differences between the experiment and CMC calculations due to the local extinction, but the Girimaji model gives the closest profiles to the experiment, shown in Figure 3.15 (b) and (d). As we move downstream along the jet, the mixture is more homogeneous and the Girimaji model for the conditional scalar dissipation rate gives better prediction. The different lines in Figure 3.15 are conditional averages from different radial locations. It is evident that they are very similar, which implies that, at this axial location, the conditional averages are very weak function of radius.

Figure 3.16 shows the conditional mean temperature from the CMC nodes along the pilot jet axis, 'C' in Figure 3.9, and along the radius, 'A' direction in Figure 3.9, at $9.1mm$ from the nozzle. In the region of pilot flame and close to nozzle, the variation in the peak conditional temperature is about $250K$ as in Figure 3.16 (a) and (b). But this variation becomes small at a downstream location as in Figure 3.16 (c). This is because of the changes in the conditional scalar dissipation rate values show in the insets. Figure 3.17 shows large differences of conditional species along the line 'A' and 'C' in Figure 3.9, axial and radial direction respectively. Downstream, the differences are decreased as seen in Figure 3.15. For this experiment, Figures 3.15-3.17 suggest large variances of conditional mean quantities along and across the jet, especially close to the nozzle which implies that this flow should not be calculated by a cross-stream averaged (one-dimensional) CMC. Good predic-

tion in temperature but lack of species predictions were reported by using a cross-stream averaged (one-dimensional) CMC (Roomina and Bilger, 2001; Fairweather and Woolley, 2003; Kim and Huh, 2004), an observation consistent with the present data.

Figure 3.18 shows the comparison between the presumed mixture fraction PDF and the experiment. It is evident that the beta PDF can provide accurate information. The good agreement also suggests that the mean and r.m.s. of mixture fraction are calculated accurately by FLUENT, as also seen in Figure 3.5 and Figure 3.8. The PDF is used to calculate the mean quantities as presented in the next paragraph.

Unconditional averages

Figure 3.19 shows that the computed mean temperature is over-predicted due to the local extinction, but the trend is captured well. The flamelet model by FLUENT also gives similar results, which is expected because it also could not account for extinction.

Figure 3.20 presents the radial mean temperature profiles at a given axial location. In Figure 3.20, (a) the temperature is under-predicted, (b) shows good agreement and (c) and (d) present over-predictions of the temperature, but the trend is well captured by the CMC simulations. Increase of C_D results in increase of mean temperature in this simulation because the r.m.s. fluctuations are smaller. Figure 3.20 (a) shows that the value of $C_D = 9$ gives better prediction of temperature near to the nozzle. It is evident that C_D is higher near the nozzle than downstream (Brethouwer, 2000; Eswaran and Pope, 1988). Both CMC and FLUENT flamelet calculations gives over-

prediction of temperature.

In Figure 3.21 (a), the mean major species mass fraction radial profiles are shown. Over predictions of CO_2, H_2O and CH_4 and under predictions of N_2 and O_2 are observed around $r \approx 0.012m$, especially O_2 shows large differences and is less consumed in the experiment due to the local extinction. Figure 3.21 (b) shows that the intermediate species are predicted reasonably well and also present the sensitivity of the conditional scalar dissipation rate model, with the Girimaji model giving better prediction.

We conclude that, despite the dependence of the conditional averages on space as allowed by the present two dimensional CMC calculations, the presence of localized extinction is not captured well. However, significant differences in the conditional averages both along and across the jet are found.

3.4 Conclusions

In this Chapter, the Delft natural gas (piloted) jet diffusion flame is simulated with the first order two dimensional CMC. A pilot was used to stabilise the flame and local extinction was observed in this experiment.

The flow field is pre-calculated by FLUENT with a Reynolds stress model for reacting flow. The $k-\varepsilon$ turbulent model gives also good agreement in non-reacting (inert) flows with a model constant $C_{\varepsilon 2} = 1.77$ for axisymmetric jet. For reacting flow, the model constants are changed to calculate correctly the flow field information. The flamelet model for non-premixed combustion in FLUENT is used to calculate the flow, with the CMC code run as a post-processing step.

The pilot provides heat to stabilise the flame and the maximum temperature zone is formed along the iso-contour line of mixture fraction $\xi = 0.15$, located in rich mixture side, an observation consistent with experiment.

Comparisons between the Girimaji model and the AMC model for the conditional scalar dissipation rate are also presented. The two models give small differences in major species and temperature, but the intermediate species predictions show some sensitivity with the Girimaji model giving better prediction, especially downstream along the jet.

The scatter plots of the experiment in mixture fraction space show the existence of local extinction. The CMC calculation does not reproduce this and the mean temperature is hence higher than in the experiment, but the calculation captures the trend reasonably well.

The conditional averages of the species along and across the jet are different, which suggests that a cross-stream averaged CMC should not apply near the nozzle where conditional fluctuations are large. Hence, a higher dimensional CMC should be used. An increase of C_D value results in a decrease of the scalar dissipation rate and does not give local extinction phenomena. It seems that a higher value of C_D should be used near the nozzle and hence its modeling is needed to compute correctly the mixing field. The discrepancy of the first order CMC between the experiment and CMC calculation involving local extinction suggests the need of higher order moment closure or double conditional closure, as also suggested by the previous studies by Roomina and Bilger (2001) and Fairweather and Woolley (2003) in attached flames. Despite the fact that two dimensional CMC shows a different approach to extinction at different points in the jet, the effect of localized extinction are

not captured. However, this conclusion should be re-examined when data for the scalar dissipation rate, which may be underpredicted here, become available.

In the following Chapter, simulations of turbulent lifted H_2 non-premixed jet flames are presented with the first order CMC which show good agreement with the experiment. The role of the each term in CMC equation is also presented.

3.5 Figures

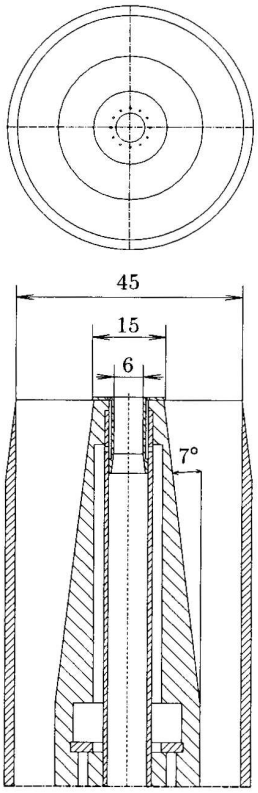

(a) Cross sectional detail of the burner nozzle

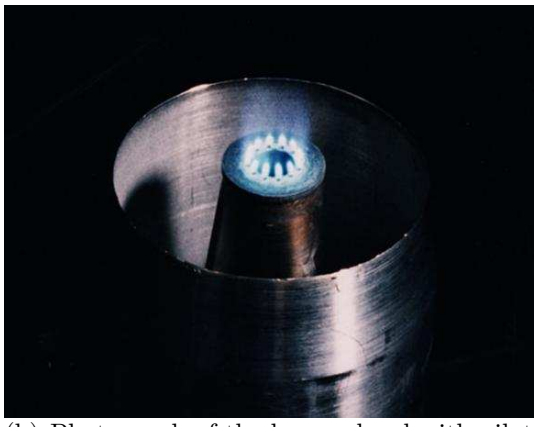

(b) Photograph of the burner head with pilot flames

Figure 3.1: Delft pilot burner; (a) cross sectional detail of the burner nozzle, all dimension, in *mm* (b) photograph of the burner head with pilot flames. From Nooren et al. (2000).

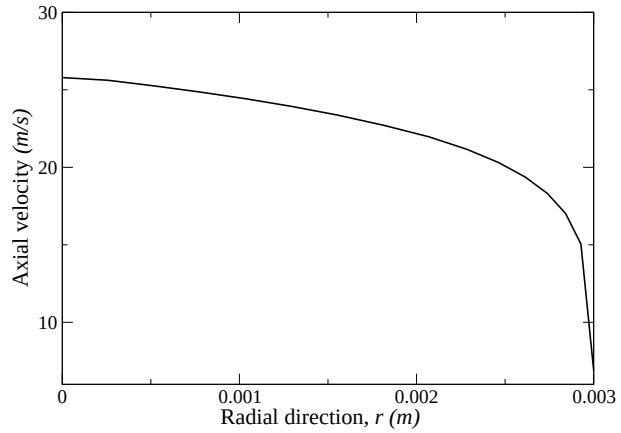

(a) Axial velocity

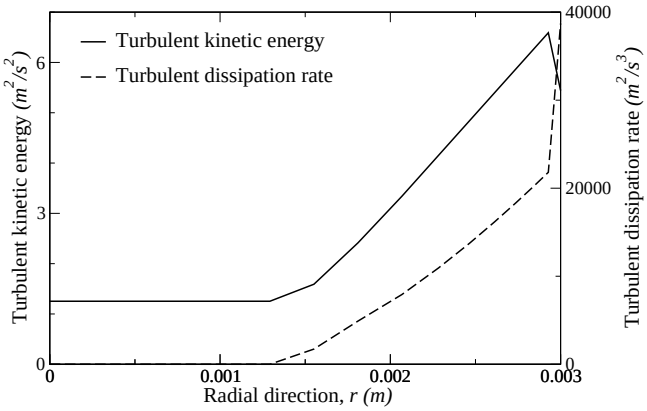

(b) Turbulent kinetic energy and dissipation rate

Figure 3.2: Radial profiles of axial velocity and turbulence quantities at nozzle exit. $r = 0$ corresponds to the burner axis and $r = 0.003$ corresponds to the inner wall of fuel tube.

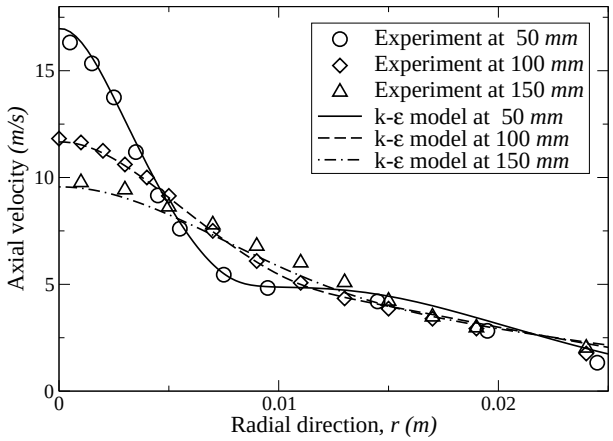

(a) Axial velocity along radial direction

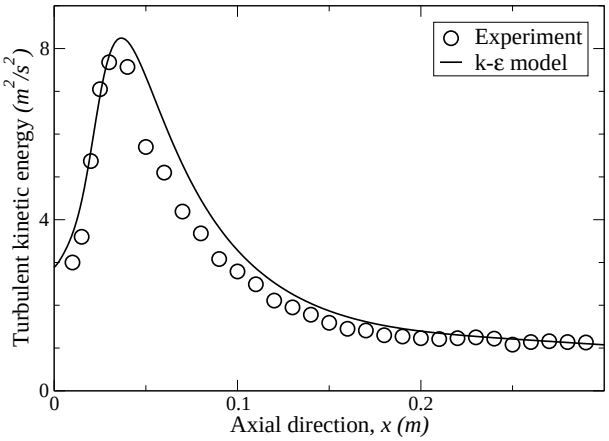

(b) Turbulent kinetic energy

Figure 3.3: Air jet comparison.

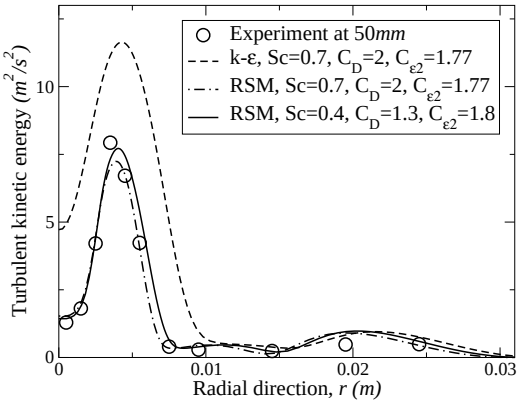

(a) At 50mm from the nozzle

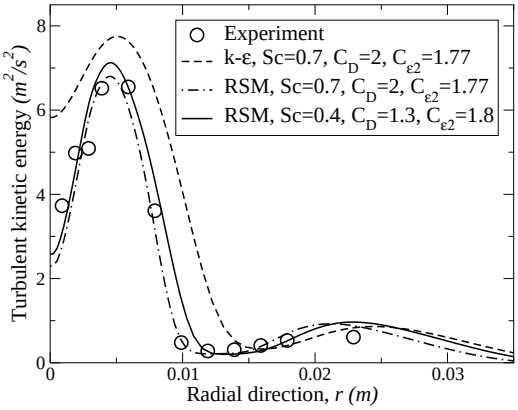

(b) At 100mm from the nozzle

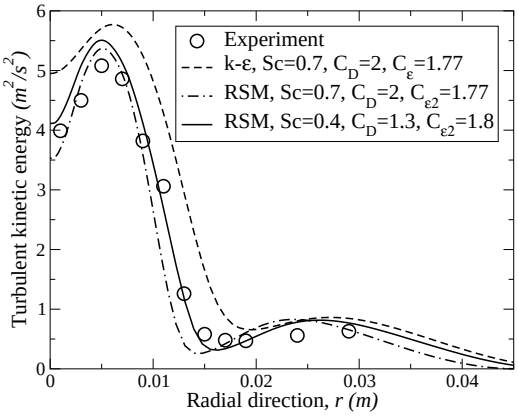

(c) At 150mm from the nozzle

Figure 3.4: Turbulent kinetic energy comparison between $k-\varepsilon$ model and Reynolds stress model (RSM).

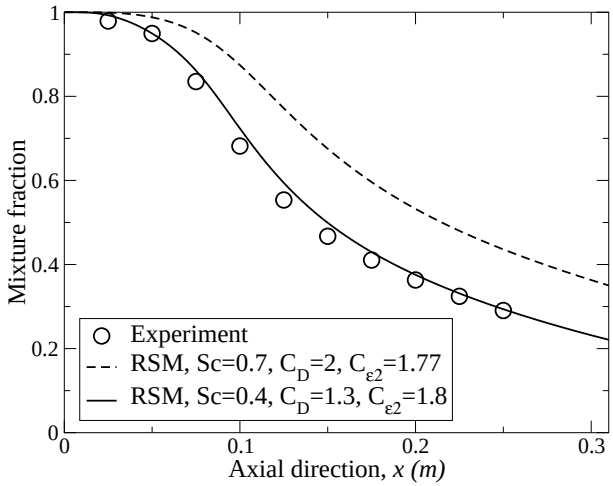

Figure 3.5: Mean mixture fraction along the axis, Reynolds stress model (RSM).

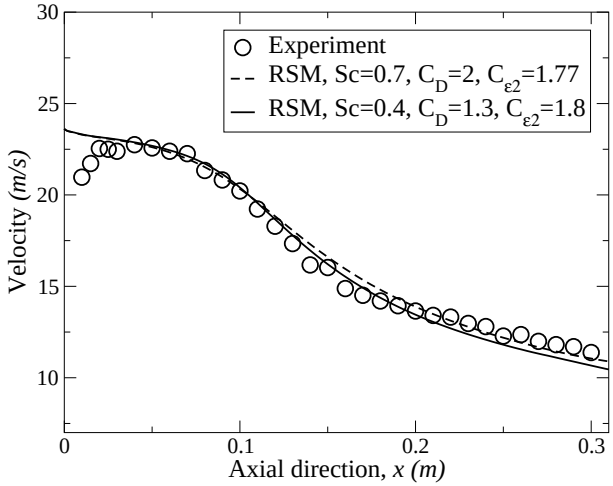

Figure 3.6: Mean velocity along the axis, Reynolds stress model (RSM).

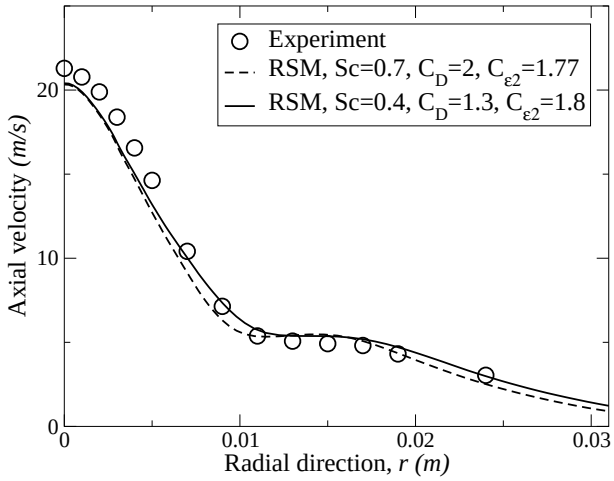

(a) At 100mm from the nozzle

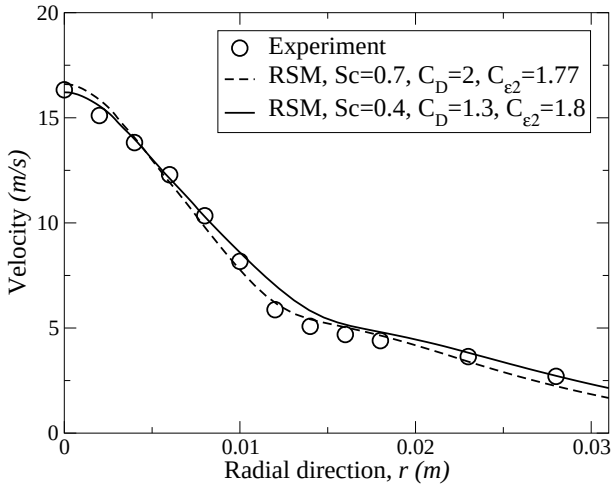

(b) At 150mm from the nozzle

Figure 3.7: Mean velocity along the radial direction, Reynolds Stress model.

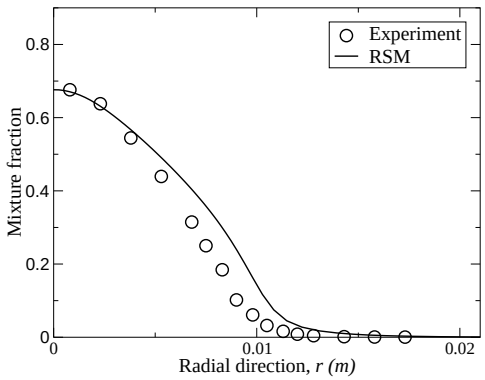

(a) Mean mixture fraction at 100mm from the nozzle

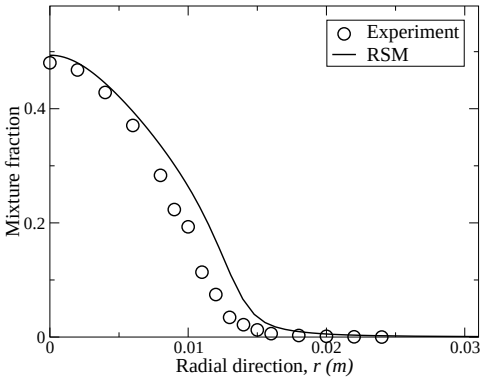

(b) Mean mixture fraction at 150mm from the nozzle

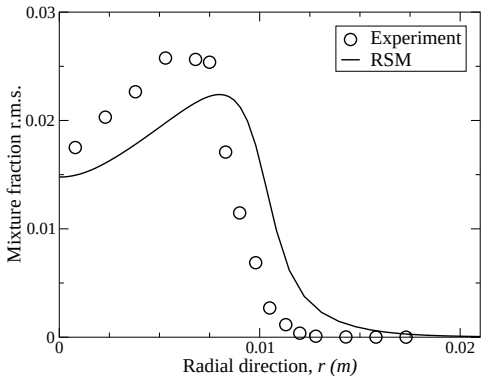

(c) Mixture fraction r.m.s. at 100mm from the nozzle

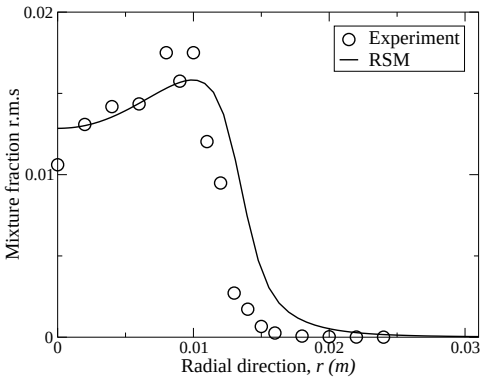

(d) Mixture fraction r.m.s. at 150mm from the nozzle

Figure 3.8: Mean mixture fraction and mixture fraction r.m.s. along the radial directions, Reynolds stress model with $Sc=0.4$, $C_D=1.3$ and $C_{\varepsilon 2}=1.8$.

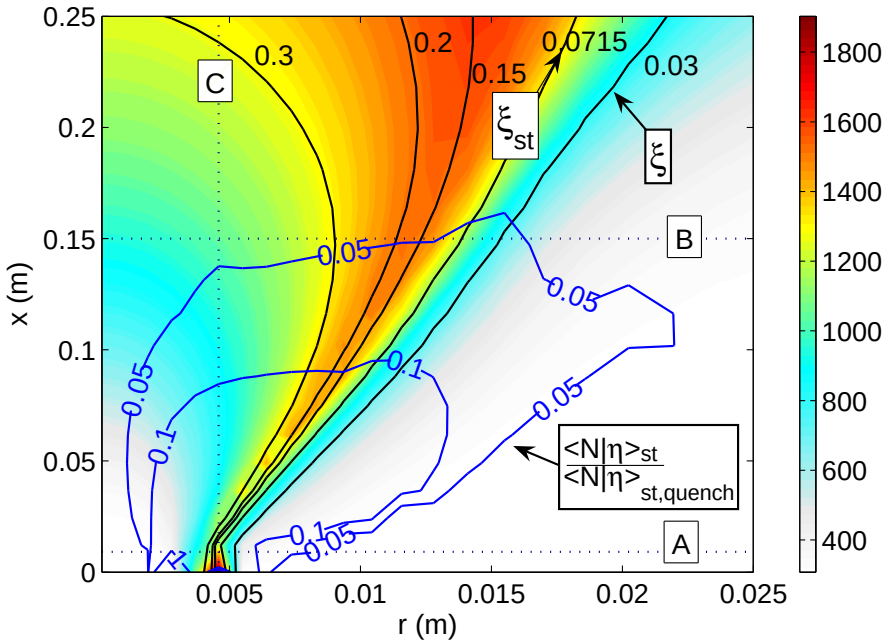

Figure 3.9: Contours of mean temperature with mixture fraction and normalised scalar dissipation rate iso-lines superimposed. The dotted lines show the locations along and across the jet which conditional averages are shown in Figures 3.15-3.17.

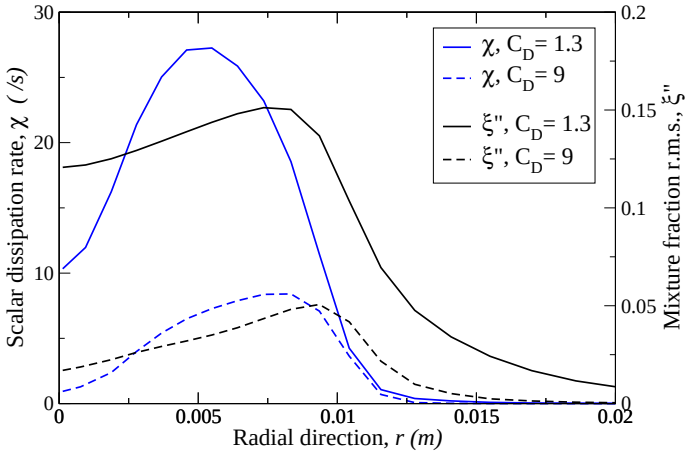

(a) Scalar dissipation rate and mixture fraction r.m.s.

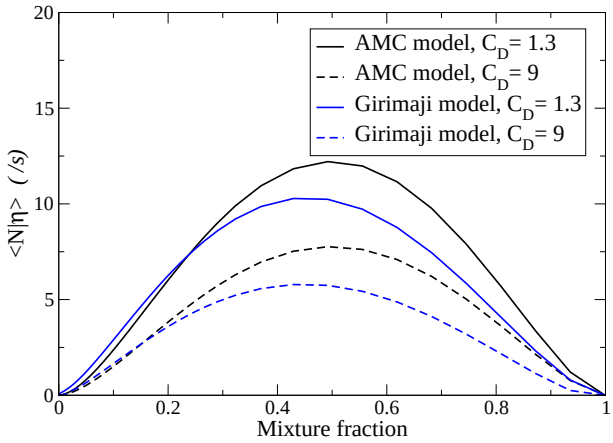

(b) Conditional scalar dissipation rate

Figure 3.10: (a) Scalar dissipation rate and mixture fraction r.m.s., (b) Conditional scalar dissipation rate of AMC and Girimaji model at $100mm$ from the nozzle.

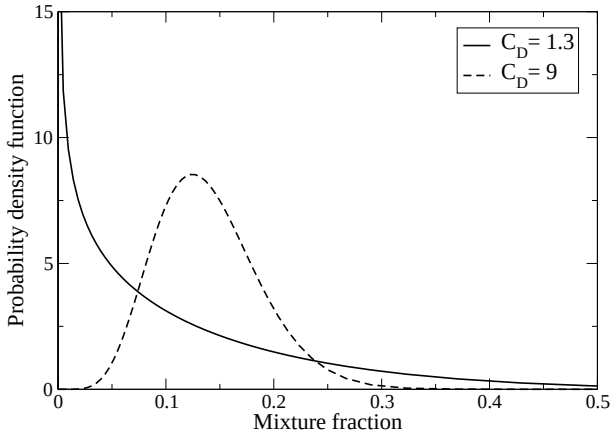

Figure 3.11: beta Probability Density Function at $100mm$ axial location from the nozzle at $r = 10.43mm$. $C_D = 1.3$ with $\widetilde{\xi} = 0.113$ and $\widetilde{\xi''} = 0.117$, $C_D = 9$ with $\widetilde{\xi} = 0.12$ and $\widetilde{\xi''} = 0.045$.

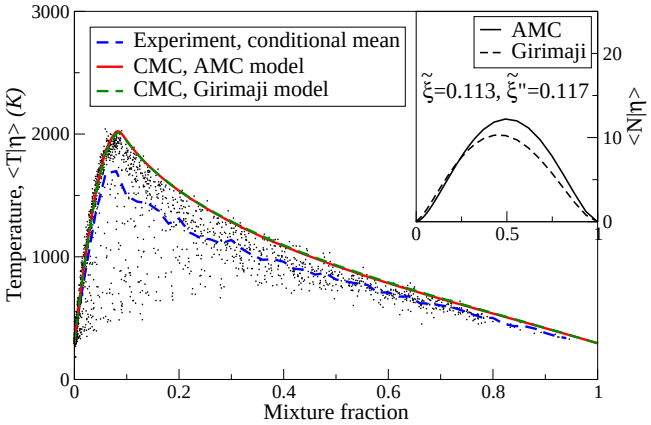

(a) Conditional mean temperature

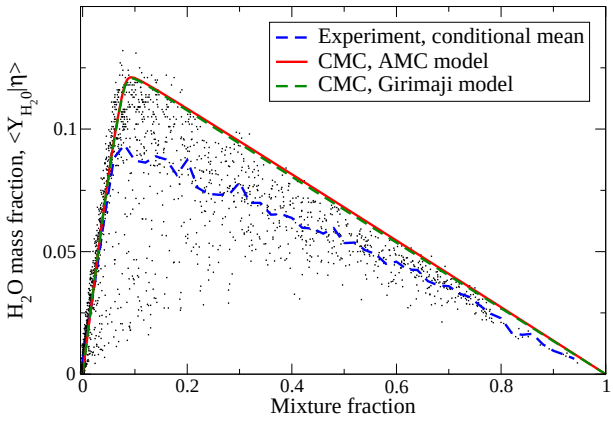

(b) Conditional mean H_2O mass fraction

Figure 3.12: Conditional mean temperature H_2O mass fraction at $100mm$ from the nozzle. $\widetilde{\xi}=0.113$ and $\widetilde{\xi''}=0.117$.

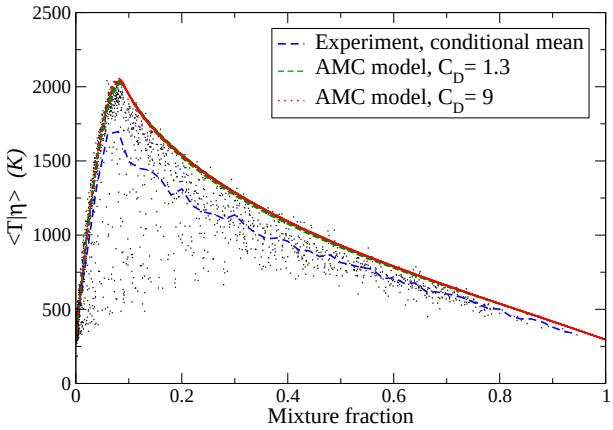

(a) AMC model with different C_D values

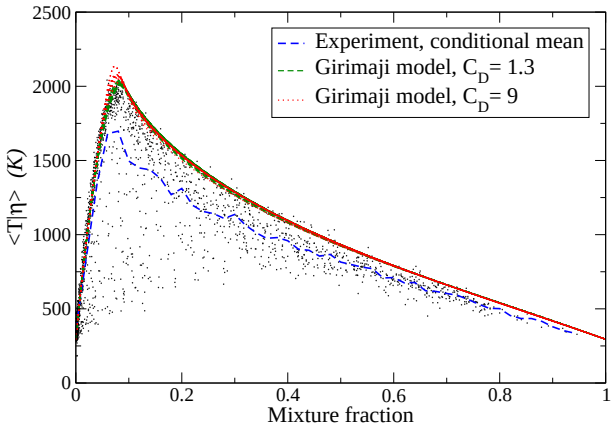

(b) Girimaji model with different C_D values

Figure 3.13: Conditional mean temperature at $100mm$ from the nozzle.

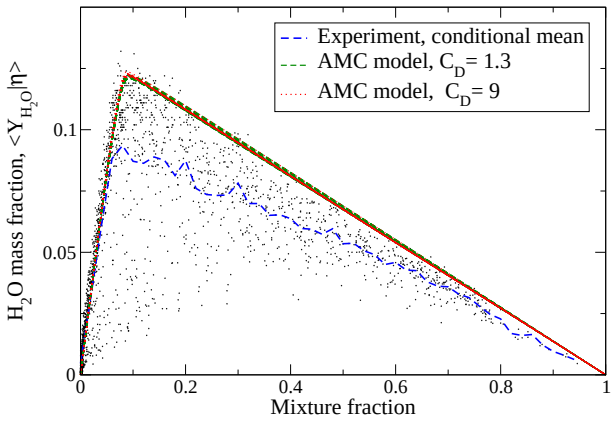

(a) AMC model with different C_D values

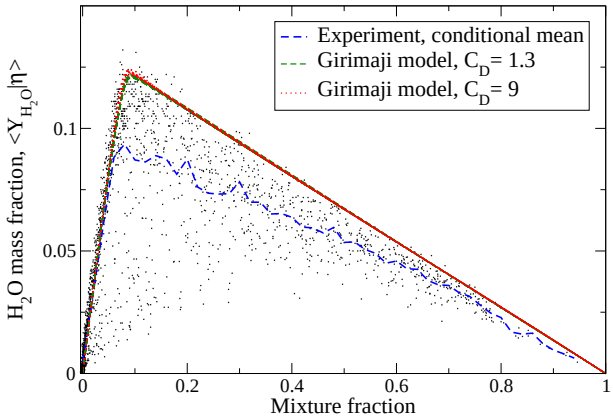

(b) Girimaji model with different C_D values

Figure 3.14: Conditional mean H_2O mass fraction at $100mm$ from the nozzle.

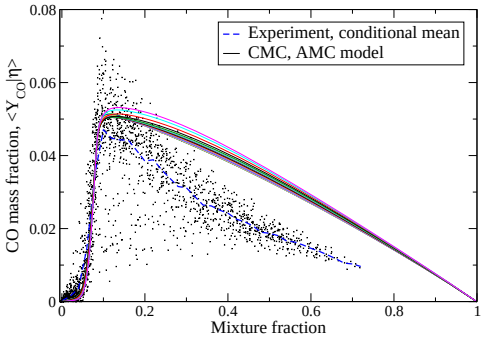

(a) Conditional mean CO mass fraction with AMC model at $150mm$

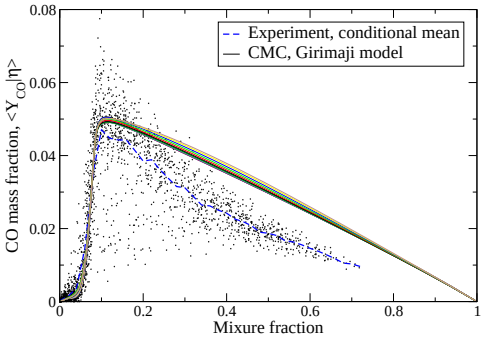

(b) Conditional mean CO mass fraction with Girimaji model at $150mm$

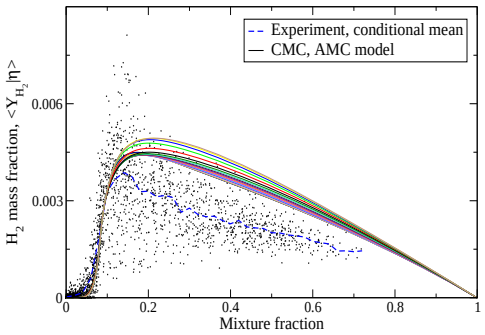

(c) Conditional mean H_2 mass fraction with AMC model at $150mm$

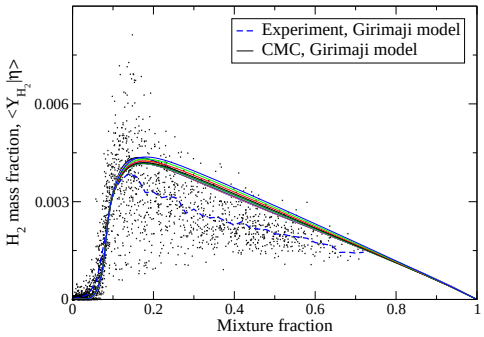

(d) Conditional mean H_2 mass fraction with Girimaji model at $150mm$

Figure 3.15: Conditional mean mass fraction of CO and H_2 at $150mm$ from the nozzle. The different lines are results from different radial locations.

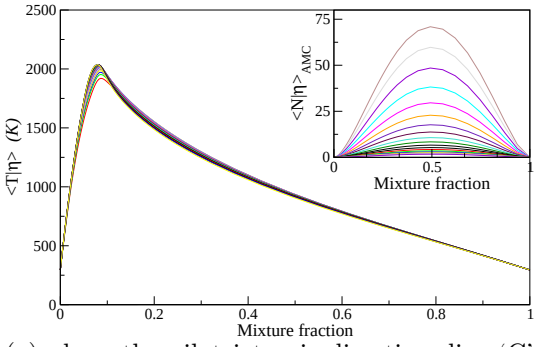

(a) along the pilot jet axis direction, line 'C' in Figure 3.9

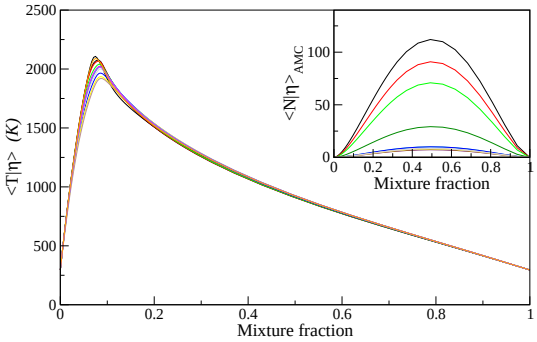

(b) at 9.1mm from the nozzle along the radial direction, line 'A' in Figure 3.9

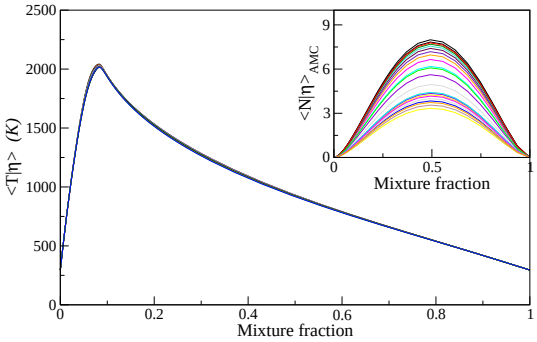

(c) at 150mm from the nozzle along the radial direction, line 'B' in Figure 3.9

Figure 3.16: Conditional mean temperatures from all CMC nodes along the axial and radial directions.

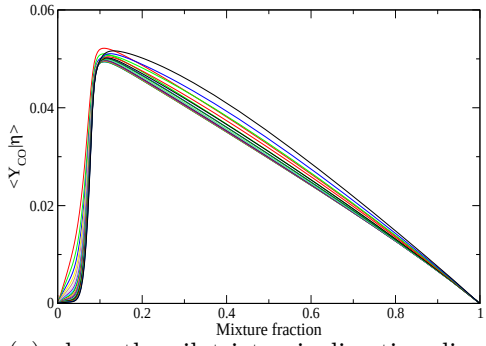

(a) along the pilot jet axis direction, line 'C' in Figure 3.9

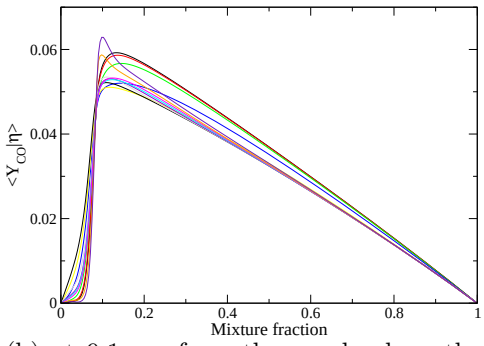

(b) at 9.1mm from the nozzle along the radial direction, line 'A' in Figure 3.9

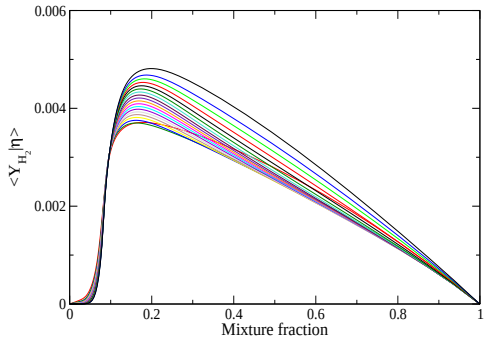

(c) along the pilot jet axis direction, line 'C' in Figure 3.9

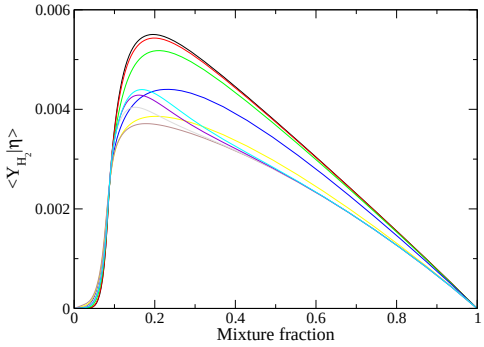

(d) at 9.1mm from the nozzle along the radial direction, line 'A' in Figure 3.9

Figure 3.17: Conditional mean species across stream along the axial and radial directions.

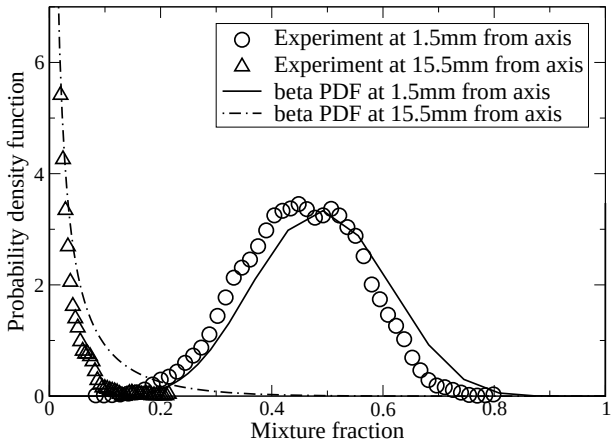

Figure 3.18: beta Probability Density Function at 150mm axial location from the nozzle.

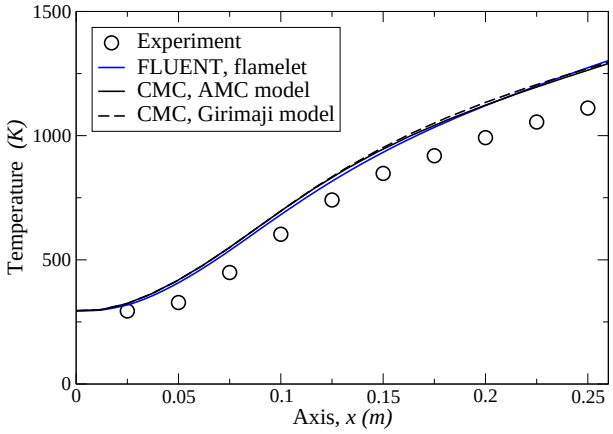

Figure 3.19: Mean temperature along the axis.

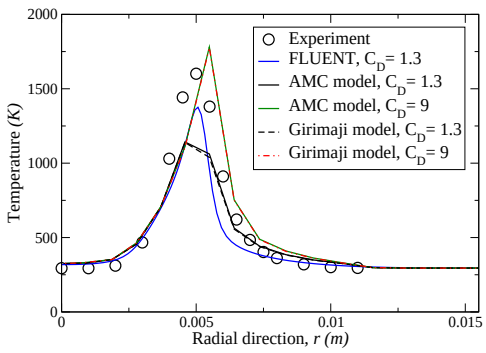

(a) Mean temperature at $25mm$

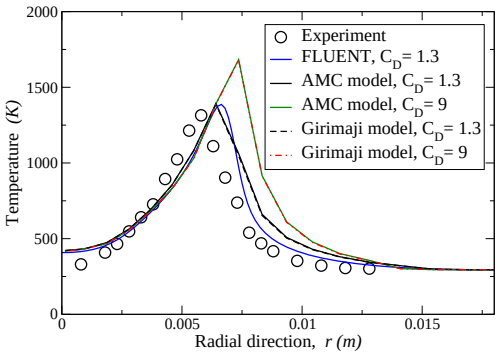

(b) Mean temperature at $50mm$

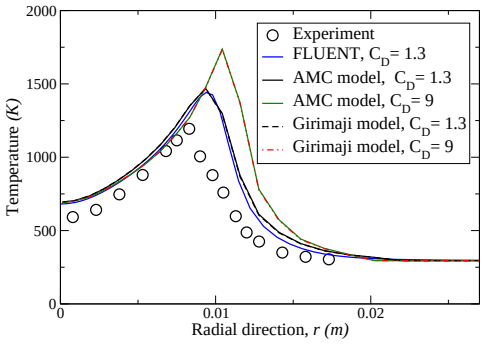

(c) Mean temperature at $100mm$

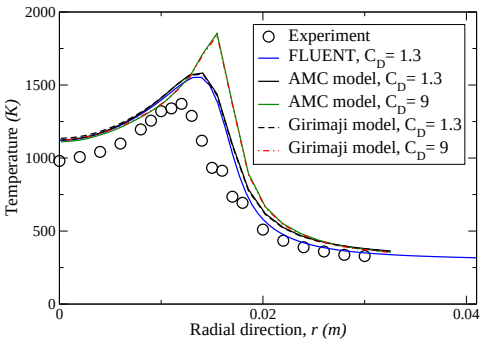

(d) Mean temperature at $200mm$

Figure 3.20: Mean temperature along the radial directions at given axial locations.

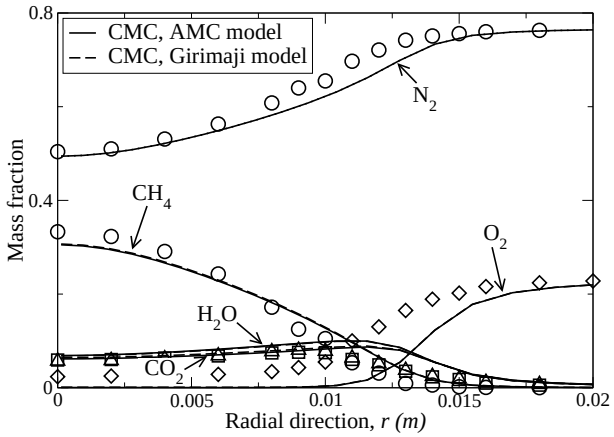

(a) Mean species mass fractions at 150mm

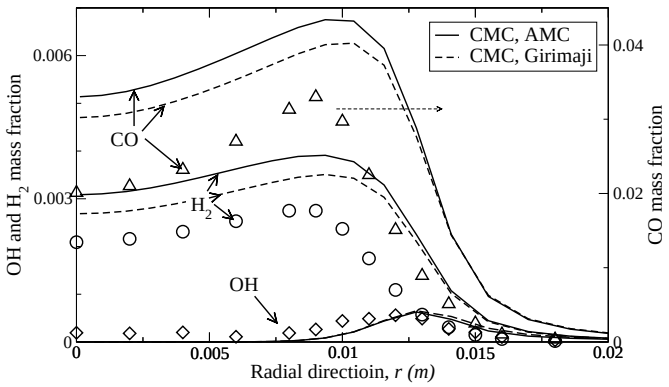

(b) Intermediate species mass fractions at 150mm

Figure 3.21: Mean species and intermediate species at 150mm axial location from the nozzle.

Chapter 4

Turbulent lifted hydrogen jet flame

In this Chapter[1], a review of stabilisation mechanisms is presented firstly and the CMC results and discussion follow. The Chapter finishes with a summary of the main conclusions and suggestion of further work.

4.1 Background

Turbulent non-premixed flames are employed in many industrial applications such as diesel engines, industrial furnaces and boilers, etc.. In those applications, lifted flames may occur and hence must be studied. In addition, lifted flames are interesting from a scientific point of view because many of the flame stabilisation and extinction controlling mechanisms are involved.

[1]Most of this work has appeared in the 30th international symposium on combustion in Chicago, 2005 (Kim and Mastorakos, 2005)

4.1.1 Flame stabilisation mechanisms

At sufficiently low flow rates, a jet flame lies close to the exit of the burner tube and is called an *attached* flame. If the flow rate is increased, there is no continuous flame close to the burner port. This is the *liftoff* condition. Therefore the flame starts at several diameters downstream of the burner, called the liftoff distance or height. At a sufficiently large flow rate, the flame can not be stabilized at all and *blowoff* or *blowout* occurs (Turns, 2000; Williams, 1985; Pitts, 1988; Savas and Gollahalli, 1986).

The stabilisation mechanism of the lifted flames have been the subject of many previous studies. The different approaches taken can be classified into three main concepts:

I) Premixed flame propagation

Understanding liftoff using the turbulent premixed burning speed has been proposed by Vanquickenborn and van Tiggelen (1966) who have suggested that the fuel and air are fully premixed along the stoichiometric mixture contour prior to the flame base. The flame stabilisation occurs at the position where the local velocity along the stoichiometric mixture contour is equal to the local flame speed. It is assumed that the diffusion flame is stabilized by propagation of a premixed flame into the mixture and the mixing has occurred on the molecular level.

II) Extinction process

The premixed flame propagation concept has been questioned by some

experimental and theoretical studies. Peters and Williams (1983) propose that flamelet extinction by excessive strain rate occurs. They argue that the amount of premixing at the molecular scale is not sufficient to justify the use of the premixed flame concept. The turbulent diffusion flame is assumed to be an ensemble of laminar flamelets at the local instantaneous stoichiometric surfaces that are stretched and contorted by the turbulent flow. If the strain rate imposed on a laminar diffusion flame exceeds a critical value, then reaction abruptly ceases and extinguishment occurs. The effects of premixedness at the molecular level are neglected in this view. Moreover, the strain between large-scale turbulent structures may describe the extinction of non-premixed flamelets and can be accounted for (Miake-Lye and Hammer, 1988; Broadwell et al., 1984).

III) Triple and Leading edge flames

This concept has been developed recently. Leading edge flame stabilisation mechanism occurs via the stabilisation of a triple flame. When a flame propagates through a fuel concentration gradient, a triple flame occurs. A triple flame is composed of two partially premixed flames, as can be seen on Figure 4.1. In Figure 4.1 (a), if the scalar dissipation rate χ exceeds the quenching limit, i.e. $\chi > \chi_q$, then an edge flame appears. On the other hand, if $\chi < \chi_q$, a propagating triple flame separates a burning zone from a non-burning zone (Vervisch, 2000). The leading-edge flames form by merging of the rich and lean branches of the triple flames into the trailing diffusion flame. Figure 4.1 (b) shows the definition of the lift-off height and also shows

the triple flame configuration.

The partially premixed fronts propagate on each side of the stoichiometric surface and are quenched rapidly and leave a diffusion flame on the stoichiometric mixture. The fuel and air mixtures form a fuel rich, a fuel lean and a stoichiometric flame near the center. Between the fuel lean and rich mixture, the curvature decreases the flame speed as the mixture moves away from the stoichiometric line.

Another factor affecting the propagation speed of triple flames is the heat release. The effect of heat release is to deflect the flow upstream of the triple flame, making the triple flame speed greater than the propagation speed of a planar stoichiometric flame, and also to decrease the mixture fraction gradient in the trailing diffusion flame. The triple flame speed decreases when the scalar dissipation rate at the flame tip increases (Veynante and Vervisch, 2002; Vervisch, 2000; Ghoasl and Vervisch, 2001).

4.1.2 Numerical simulations

Some numerical simulations will be reviewed here as related to those three concepts of stabilisation mechanism. Janicka and Peters (1982) performed a calculation for methane flames using the transport equation for PDF with extinction of laminar diffusion flamelets. Taking the value of scalar dissipation at quenching from experiments and calculating the volume-average of mean scalar dissipation rate, good agreement was found only for small lift-off heights. The extended model for partially premixed or locally premixed diffusion flamelets by Peters (1984b) derived that the concept of premixed flame propagation was only justified if the scalar fluctuations at the stabilisation

height were very low.

The extinction process by large scale motions was proposed by Broadwell et al. (1984). They considered large scale motion and small scale mixing between fuel and air. The large scale motion carried the hot combustion products from inside of the fuel jet to the outer edge with re-entrained air. Consequently, flame sheets at near stoichiometric condition along the mixture could be formed with sufficient mixing time. If the mixing time was too short, then temperature and radical species concentrations decrease before ignition can occur (Schefer et al., 1994a,b).

Yamashita et al. (1996) showed the relationships between Reynolds and Damköhler numbers at transition point from laminar to turbulent where large scale fluctuations and locally stretched flames were assumed to cause extinction. Bradley et al. (1998) presented a diffusion flame model based on combustion in strained premixed laminar flamelets. The high shear generated by the initial mixing between fuel and air near the jet quench both diffusion and premixed flamelets. The strain rate then relaxes and premixed burning is ensured further downstream. The prediction of lift-off heights agreed well with limited experimental data.

Triple flame and leading-edge flames have been considered as possible stabilisation mechanisms for lifted flames, as discussed before. Müller et al. (1994) combined premixed and non-premixed flamelet formulations to treat partially premixed combustion in the fast chemistry limit to account for the partial premixing of fuel and oxidizer that occurs before the lifted flame. They showed that the unsteady flame propagation dominated in partially premixed flame and that the flame stabilised downstream of the position

where $\bar{\chi} = \chi_q$, presenting hence that flamelet quenching was important as well.

Domingo and Vervisch (1996) worked on autoignition (by an adiabatic compression) of non-premixed turbulent mixtures using DNS and observed the role of partially premixed flame in the propagation of ignition as triple flamelets structure. The ignition started along the stoichiometric surface and the two different premixed flames (lean and rich) separate and propagate into opposite directions. The quenching of diffusion flames by large strain rate were also observed. They concluded that the flame at ignition was more dominated by the conditional mean value of the dissipation rate at stoichiometric mixture fraction rather than by its total mean value, and they showed that the autoignition of non-premixed mixtures had strong relationship with partially premixed combustion in the particular form of triple flamelets.

Chen et al. (2000) also combined the flamelet models for turbulent premixed and non-premixed combustion to describe turbulent flame propagation in inhomogeneous mixtures of fuel and oxidiser. They showed that the mean structure of the lifted turbulent diffusion flame was similar to a laminar triple flame. The stabilisation points, assumed to be locally premixed, were found to be located on the lean side of triple flame at low exit velocities of the jet and near the isoline of stoichiometric mixture. Their results had good agreement with experimental data.

Ghoasl and Vervisch (2001), using DNS, found that the stabilisation behaviour was related to the Schmidt number and the Reynolds number. They observed that at the stabilisation point the triple flame propagation speed was much larger than the stoichiometric flame speed, which was due to the

curvature of the triple flame. Hysteresis effects were also observed so that the flame lift-off and reattachment did not happen at the same conditions. They presented possible stable lifted flames for all values of the Schmidt number, however, the lifted flame region was only supported for Schmidt numbers less than unity.

Mizobuchi et al. (2002) analysed a simulation of turbulent lifted hydrogen jet lifted flame with three-dimensional DNS. The lifted flame structure consisted of three flame elements. A stable laminar leading-edge flame (a triple flame-like structure) occurred outside of the jet and the inner turbulent premixed flame was observed before burning and stabilised by the leading-edge flame. Abruptly isolated floating diffusion flame from the rich premixed flame was observed and was continuously burning by the molecular diffusion on the outside of the flame. A review of the edge-flame can be found in Buckmaster (2002).

Domingo et al. (2002) performed a Large Eddy Simulation (LES) for a lifted flame and observed that the combustion regime combined the properties of both premixed and diffusion flames. Partially premixed flames were observed in the fuel and air mixture before burning.

The recent research (Mizobuchi et al., 2002; Ghoasl and Vervisch, 2001; Chen et al., 2000; Domingo and Vervisch, 1996; Domingo et al., 2002) has focused on the triple flame stabilisation mechanism and the propagation of partially premixed flames.

4.1.3 Experimental evidence

Many experimental results have provided data on the flame stabilisation mechanisms and have assisted modelling efforts. Eickhoff et al. (1984) measured the rate of molecular mixing and fuel burnout from gas concentration and velocity. Approximately forty to fifty percent of the total fuel stream was already mixed at the molecular level and reacted a very short distance downstream of the stabilisation region. It was suggested that molecular diffusion occurred through the large eddies and support for the premixed concept was given.

Savas and Gollahalli (1986) observed Schlieren photographs of lifted flames. The structure of the flow between the nozzle and the base of the flame was essentially similar to that of the cold jet. The rolled-up eddies retained their identity and integrity for some distance even above the flame base. The flame base was much closer to the rolled-up eddies than the attached flame.

In Schefer and Goix (1998) and Schefer et al. (1994b,a), the flame zone formed along large-scale turbulent structures in the mixing region. These authors observed that the large-scale turbulent structures in the mixing region caused higher fluctuations in the flame and greater spatial movements than in the central jet region. The fuel and air were premixed and spanned the flame stabilisation point where the magnitude of the scalar dissipation rate was considerably below the critical value that could result in extinction. This indicated that the scalar dissipation was not an important parameter in the stabilisation mechanism for the flames. Local stoichiometry and turbulence characteristics were the primary factors to control flame stability. The

excessive stretch of the vortical large-scale structure could lead to local flame extinction. They suggested that large-scale structure effects and premixed flame propagation should be included for stabilisation. Triple flame concepts were also employed in Schefer and Goix (1998).

Miake-Lye and Hammer (1988) studied the effects of dilution on the lift-off heights for methane, ethylene and natural gas. Dilution of the fuel in the jet with air produced a greater lift-off height for large dilutions. The stability of the flame was dominated by the strain between large-scale structures in the jet. Muñiz and Mungal (1997) presented the effects of coflow and jet-exit velocities. Increasing coflow or jet-exit velocities increased the height of lift-off. They also noticed that the structure was similar to triple flames.

Lifted flames in bluff-body flows, not jets, have been introduced in Esquiva-Dano et al. (2001) and Chen et al. (1998). In general, the recirculation zone generated by the bluff-body improved the stabilisation. In this geometry, lift-off heights also increased with increasing fuel exit and coflow velocity and triple flames were also observed. Tacke et al. (1998) observed that the large-scale turbulent structures played the main role in the stabilisation mechanism, similar to the experiment by Hasselbrink and Mungal (1998).

Han and Mungal (2002) presented the stabilisation region of turbulent lifted deflected-jet flames injected at 45° into a cross-flow and observed that the velocity at the flame base was related to the stoichiometric velocity. The increase of the flame base velocity beyond the leading edge flame propagation speed resulted in blowout. The observations supported the leading edge flame stabilisation mechanism that the incoming flow speed is balanced with the propagation speed of the partially premixed flame (Buckmaster, 2002).

These experiment can be summarised into a few points below. Substantial premixing occurs when the mixture starts being ignited at the base of the turbulent lifted flame (Eickhoff et al., 1984). The flame can be stabilised when the local gas velocity is or near the premixed laminar flame speed, hence the turbulence characteristics are also important factors in keeping stability (Muñiz and Mungal, 1997; Esquiva-Dano et al., 2001; Chen et al., 1998). The scalar dissipation rate at the flame base is lower than the critical quenching value and the excessive stretch of the eddies can play an important role of local flame extinction (Schefer and Goix, 1998; Schefer et al., 1994b,a). Finally, recent work suggests that triple flame stabilisation at the base of a turbulent lifted flame can explain all of the important phenomena.

In the following Section, a simulation of turbulent lifted jet flames with two-dimensional CMC is presented, in order to assist understanding of the stabilisation mechanism and to examine the use of elliptic CMC for an application where significant gradients of conditional averages are expected to occur.

4.2 Simulation of turbulent lifted jet flames

4.2.1 Background

As we saw in the previous review, turbulent lifted jet flames involve a complex balance between convection, diffusion and chemistry and hence present a considerable challenge to combustion models. In this Section, simulations of H_2-air lifted jet flames are presented, obtained in terms of two-dimensional, first-order Conditional Moment Closure (CMC). The unsteady CMC equa-

tion with detailed chemistry is solved without the need for operator splitting, while the accompanying flow field is determined using commercial CFD software (FLUENT) employing a k-ε turbulence model. Computed lift-off heights and Favre-averaged species mole fractions are found to be very close to values obtained experimentally for a wide range of jet velocities and fuel-air mixtures.

Two different initial flame conditions are explored. In the first, the jet velocity gradually increased from an attached flame, and in the other condition "ignition" was made downstream of the nozzle by initialising with a burning solution in mixture fraction space at a few CMC spatial nodes. These two different initializations result in different behaviour of lifted flames. The stabilisation mechanism is explored by quantifying the balance of terms in the CMC equation in the lift-off region. An analysis of the scalar dissipation was done to help understand the stabilisation mechanism.

Recently, lifted turbulent flames have also been examined by Devaud and Bray (2003) with the CMC model. In that work, the first-order CMC approach included the spatial convection and diffusion terms, but cross-stream averaging was performed following Klimenko and Bilger (1999), so that the conditional averages were predicted to depend only on axial distance. Very good agreement with experimental data was found. The present simulations are two-dimensional in order to examine if the extra dependence of conditional averages affects the results.

In attached turbulent non-premixed jet flames, the homogeneous version of CMC (i.e. without any spatial transport terms) has produced very accurate results (Roomina and Bilger, 2001; Smith et al., 1995; Fairweather

and Woolley, 2003). Two-dimensional first-order CMC calculations have been performed for autoignition problems (Mastorakos and Wright, 2003; Kim et al., 2000a; Kim and Huh, 2002b) and bluff-body flames (Kim et al., 2000b). Devaud et al. (2003) developed a two-dimensional formulation for lifted methane flames, but no detailed analysis of the differences between cross-stream averaged CMC and two-dimensional CMC was given.

In the present Chapter, we revisit the problems simulated by Devaud and Bray (2003). Two-dimensional CMC simulations of turbulent lifted jet flames of hydrogen with a wide range of jet velocities and dilutions are performed in order to explore lift-off height and to understand better the stabilisation mechanism. In the next Section the model and numerical methods are presented, which is followed by a detailed discussion of the results.

4.2.2 Numerical methods

The governing equation of CMC for the temperature is analysed in terms of spatial and mixture fraction spaces. The governing equation for the conditional temperature can be re-written from Eq. (2.18):

$$\frac{\partial Q_T}{\partial t} = \underbrace{-\langle u_i|\eta\rangle \frac{\partial Q_T}{\partial x_i}}_{T_{cv}} + \underbrace{\langle N|\eta\rangle \frac{\partial^2 Q_T}{\partial \eta^2} + \langle N|\eta\rangle \left[\frac{1}{\langle c_p|\eta\rangle}\left(\frac{\partial \langle c_p|\eta\rangle}{\partial \eta} + \sum_{\alpha=1}^{n} c_{p\alpha}\frac{\partial Q_\alpha}{\partial \eta}\right)\right]\frac{\partial Q_T}{\partial \eta}}_{T_m}$$
$$\underbrace{-\frac{1}{\bar{\rho}\tilde{P}(\eta)}\frac{\partial}{\partial x_i}\left(\langle u_i'' T''|\eta\rangle \bar{\rho}\tilde{P}(\eta)\right)}_{T_d} + \underbrace{\frac{\langle \omega_h|\eta\rangle}{\langle \rho|\eta\rangle\langle c_p|\eta\rangle}}_{T_c} \tag{4.1}$$

In Eq. (4.1), the T_{cv} and T_d terms are for spatial convection and diffusion and T_m correspond to molecular diffusion (i.e. mixing in mixture fraction space). Pressure is assumed constant and hence the pressure work term is

neglected.

The linear model for the conditional velocity (Eq. 2.23) and the gradient diffusion model for the conditional flux (Eq. 2.27) are used. The AMC and the Girimaji model for the conditional scalar dissipation rate with the clipped Gaussian PDF and beta PDF of the mixture fraction are used and compared in this Chapter. The other sub-models are used as described in Section 2.2. A detailed mechanism for hydrogen was taken from GRI-v3 (Smith et al., 1999), keeping only the H_2 sub-system, resulting in a total of 9 species with 28 reactions. Very similar results were obtained with the mechanism of Devaud and Bray (2003).

The CMC equations were discretised by finite differences in physical and mixture fraction space. Upwind differences were used for the convection term and central differences for the diffusion term. The resulting three-dimensional grid had N_r=16, N_x=17 and N_η=101 nodes in the radial and axial directions and in mixture fraction η-space, clustered around the expected stabilisation region and the stoichiometric mixture fraction to improve resolution.

The mean velocities, the mean and variance of the mixture fraction, the turbulent diffusivity, k and ε come from a CFD solution of the jet with FLUENT (FLUENT, 2003), assuming inert flow, following Devaud and Bray (2003). This is not a bad assumption since the flow until the stabilisation height is frozen. No coupling between CMC and CFD has been attempted here. However, the expansion caused by the flame could affect the flow field just ahead of the flame edge and should be examined in the future. The computational domain extended $130D$ (D being the jet diameter) in the axial and $50D$ in the radial directions and incorporated a total of 48,728 nodes, which

gave grid-independent results. Outflow boundary conditions were used for the downstream exit and a given entrainment rate calculated from Spalding (1979) as a function of the jet flow rate was used in the boundary far away from the axis and the inlet air boundary next to the nozzle. The standard $k-\varepsilon$ model with the modification $C_{\varepsilon 2}$=2.02 provided the best results. This was done in order to have as accurate mixing as possible, if a comparison between the computed and measured means is a true test of CMC. The CMC spatial grid extends $9D$ in the radial and $20D$ in the axial direction, as we are mostly interested in the lift-off region.

The boundary conditions at $\eta = 0$ and $\eta = 1$ were specified according to the air and fuel composition and temperature. All conditional averages had zero axial gradient on the downstream boundary and zero radial gradient along the axis. At large radii and at the jet inlet, a Dirichlet condition with a "frozen flamelet" (i.e. corresponding to inert mixing between fuel and air) in η-space was imposed.

Figure 4.2 shows an example of the frozen and burning flamelets in mixture fraction space. The burning flamelets are calculated from an homogeneous version of CMC (i.e. no spatial convection and diffusion terms in the CMC equation (Eq. 4.1)) with $\langle N|\eta = 0.5\rangle = 10\ s^{-1}$ and the flamelets are used as initial condition for the lifted flames.

4.2.3 Experiment

The lifted jet flames from Brockhinke et al. (2000) and Cheng et al. (1992) have been considered, as these have been very thoroughly documented. The jet diameter D was 2 mm and the fuel velocity U_{jet} varied from 80 to 900

m/s. No co-flow was used and H_2 pure, or diluted by N_2, was used. The experiments covered lift-off heights, mean temperature, mean mole fractions of major species and OH and estimates of the scalar dissipation rate.

4.3 Results and discussion

4.3.1 Flow field

Experimental measurements (Cheng et al., 1992) are only available at few axial locations. Figure 4.3 presents radial distributions of mean and root mean square (r.m.s.) of the mixture fraction (the latter normalised by the centreline value), at two axial locations. It is evident that the mixing field is accurately computed, which is due to the care taken with the k–ε model constants and the entrainment boundary condition in the CFD analysis. The velocity profiles are not presented because there are no experimental data available, however the good agreement in Figure 4.3 indicates that the velocity should be accurately computed as well. These results suggest that further comparisons of mean quantities obtained with CMC and from measurements can be performed unambiguously.

4.3.2 Lift-off height

The lift-off height (h/D) of pure and diluted flames is investigated here at various U_{jet}. These CMC calculations were performed by initialising with a frozen flamelet everywhere except for a few CMC nodes (at a value of x/D corresponding approximately to the measured h/D to save CPU time) where a burning flamelet was deposited. Figure 4.4 shows the CMC grid (dotted lines) and the initial flame temperature condition for pure H_2, $U_{jet} = 680m/s$

and the downstream is ignited at $x/D = 12$ and radial locations corresponding to $0.018 < \tilde{\xi} < 0.04$. The flame then spread in all directions and stabilised at the location shown in Figure 4.5. The lift-off height was determined experimentally (Cheng et al., 1992) by visual observation corresponding to a peak mean temperature of about 900K; the same criterion was used here. Figure 4.5 suggests that the first order elliptic CMC agrees with the experiment (Brockhinke et al., 2000). In general, the lift-off height was obtained to within 1 to $2D$ of the experimental value for all jet velocities and dilutions tested.

Figure 4.5 also includes calculations where the initial condition of the simulation was an attached flame and U_{jet} was gradually increased. In these cases, the flame remains attached to the jet nozzle, even at velocities for which downstream ignition resulted in a lifted flame. This phenomena was also observed in the experiment by Brockhinke (2003). Hence the present simulations seem to reproduce very well many facets of lifted jet flame stabilisation.

4.3.3 Unconditional and conditional averages

Figure 4.6 shows the PDF profiles on the different locations around the lift-off height. The differences between the beta PDF and the Clipped Gaussian PDF are large and the Clipped Gaussian PDF generates a large delta function at $\eta = 0$. The resultant unconditional averaged species mole fractions are shown in Figure 4.7 and Figure 4.8. The AMC model with Clipped Gaussian PDF around the lift-off heights gives more accurate results as shown in Figure 4.8.

Figure 4.7 shows that, immediately downstream of the lift-off height, the computed mean mole fractions are in reasonable agreement with the measured values (Cheng et al., 1992). It is evident that H_2O is under-predicted and O_2 and H_2 are over-predicted around r/D=2.5 in the three different simulations (the AMC models and the Girimaji model for the conditional scalar dissipation rate with Clipped Gaussian PDF and beta PDF). Figure 4.8 shows that the mean OH is under-predicted, but the general trend is captured well. The differences between experiment and calculation are partly due to the fact that the computed h/D was at 9, while the measured one was at 7. The same good agreement was found in Devaud and Bray (2003) with a cross-stream averaged CMC and this suggests that the present 2D-CMC may not be necessary for lifted jet flames. However, it is explored for a better understanding of the stabilisation mechanism.

The following analyses are calculated with the AMC model for conditional scalar dissipation rate and the Clipped Gaussian PDF. In Figure 4.9, the highest temperature at the flame edge is observed at the mean stoichiometric mixture fraction ($\tilde{\xi}_{st} = 0.0285$) and the highest temperature appears on the rich side further downstream. The general shape of the contour is consistent with measurements and recent DNS data (Mizobuchi et al., 2002) and is typical of other dilutions. The five points around the lift-off region as marked on Figure 4.9 are used for further analysis.

Figure 4.10 and Figure 4.11 show that the conditional averaged temperature and OH mole fraction respectively correspond to a burning flamelet further downstream, while the upstream profiles show intermediate values. A Q_T of about 700K (Figure 4.10; $x/D = 8.5$) still has negligible OH. The

peak OH is found at stoichiometric mixture fractions and the smooth progression from frozen to burning flamelet is evident. Figure 4.12 shows that the conditionally-averaged oxygen corresponds to inert mixing before the flame, is consumed at the flame, and a local peak is found at rich mixture fractions. This is due to the significant pre-mixing that has occurred until the flame edge and is consistent with LES calculations (Domingo et al., 2002) and other models (Müller et al., 1994). At large distances downstream, this oxygen is consumed and the flame tends to the equilibrium state.

4.3.4 Balance of terms in CMC equation

The balance of the individual terms in the CMC equation for the temperature (Eq. 4.1) is examined here in order to investigate the flame stabilisation process. Each of the terms around the lift-off region are plotted separately in mixture fraction space. In Figure 4.13, the subscript *axi* and *rad* refer to axial and radial component respectively. Figure 4.13 (a), (b) and (c) show the profiles at different x/D but at the same radius. In Figure 4.13 (a), just before the flame region, the axial convection ($T_{cv,axi}$) and the molecular diffusion terms (T_m) are negative and balance the chemistry (T_c) and the axial diffusion ($T_{d,axi}$) terms. The radial convection ($T_{cv,rad}$) is important only at the rich side, while the radial diffusion term ($T_{d,rad}$) is negligible everywhere. This "flamelet" receives heat by diffusion from downstream at $\eta \approx 0.05$, and generates a little of its own and distributes it to other mixture fractions.

As we move into the flame region (Figure 4.13 (b)), the chemistry term is an order of magnitude larger than before and now balances all other terms.

The peak heat release has now shifted to ξ_{st}. Further downstream, Figure 4.13 (c), the heat release term is again lower and the molecular diffusion term becomes the dominant in balancing the chemistry, approaching the well-known structure of a non-premixed flame. The second peak of heat release at $\eta \approx 0.15$ (also evident in Figure 4.13 (b)) is due to a rich reaction zone propagating across mixture fraction space to consume the premixed fuel-oxygen mixture, consistent with the underlying presence of a triple flame and with the high oxygen concentrations found in rich η in Figure 4.12.

A comparison of Figure 4.13 (b) and (d) shows that away from the stabilisation region towards the axis, the flamelet produces heat at stoichiometry and loses it to axial convection, with all other terms being small. Further outwards (Figure 4.13 (e)) we see again a double reaction zone at stoichiometric and at rich mixture fractions. Substantial partial premixing is evident everywhere.

Therefore, the spatial transport terms play a major role in stabilisation, as expected. The large magnitude of the spatial diffusion term at the stabilisation point, and the use of the model for Eqs. (2.23) and (2.27) which has been validated by DNS in Chapter 2, but more extended validation should be performed by DNS or experiments, implies that this sub-model is important and should receive further attention. In addition, a consistent observation is that the radial convection and diffusion terms are almost negligible. This justifies fully the use of cross-stream averaged CMC for jet problems (Devaud and Bray, 2003; Klimenko and Bilger, 1999; Fairweather and Woolley, 2003) except close to the nozzle, as described in Chapter 3.

4.3.5 Scalar dissipation rate at lift-off height

A comparison between the computed scalar dissipation rates at the lift-off height with the one necessary for flamelet extinction is given here. A homogeneous version of our CMC code with the same chemistry was run with increasing $\langle N|\eta\rangle$ (Eq. 2.25) so that the quenching scalar dissipation rate at extinction $\langle N|\eta\rangle_{st,quench}$ at the stoichiometric mixture fraction could be quantified. This was found to be around 73 s^{-1} for pure H_2 flame.

Figure 4.14 shows the comparison of the different conditional scalar dissipation rate models around the lift-off height. The AMC model with beta PDF produces values little higher than the AMC model with Clipped Gaussian PDF and the Girimaji model lower values than the AMC models. The different conditional scalar dissipation rate contour plots can be seen in Figure 4.15 and Figure 4.16.

Figure 4.15 and Figure 4.16 present the different conditional scalar dissipation rate models (Figure 4.15 (a) is simulated by the AMC model with Clipped Gaussian PDF, Figure 4.15 (b) is the AMC model with beta PDF and Figure 4.16 is the Girimaji model). The profiles show the same lift-off heights and result in small differences in mean temperature and the normalised scalar dissipation rate. The contour plots of Girimaji model for the conditional scalar dissipation rate are not as smooth as the AMC models because the Girimaji model shifted the maximum peak toward the mean mixture fraction and gives unsymmetrical profile as seen in the Section 2.2.3. The three different profiles show that the conditional dissipation rate at the flame's leading edge is always well below this quenching value, consistent with

measurements (Brockhinke et al., 1996, 2000). Figure 4.15 and Figure 4.16 also explain the "hysteresis" phenomenon discussed previously. Even close to the nozzle, the contour $\langle N|\eta\rangle_{st}/\langle N|\eta\rangle_{st,quench}=1$ is away from the stoichiometric iso-line (i.e. $\tilde{\xi}=\xi_{st}$). Therefore the jet velocity has to increase to very high values for $\langle N|\eta\rangle_{st}$ to reach the quenching value at the flame location, and so the flame stays attached.

4.4 Conclusions

Simulations of H_2-air turbulent lifted jet flames have been performed with two-dimensional first-order Conditional Moment Closure. The full unsteady 2D-CMC equation with detailed chemistry was solved without operator splitting with the stiff solver VODPK. The flow field was determined using FLUENT with a $k-\varepsilon$ turbulence model, which gave good agreement with measurements for the mean and the variance of the mixture fraction.

The computed lift-off heights and the Favre-averaged species mole fractions were found to be very close to experimental data for a wide range of jet velocities and dilutions. Simulations were also performed where the initial condition was an attached flame and the jet velocity then gradually increased to magnitudes that otherwise showed a lifted flame with downstream ignition. This did not result in lift-off, fully consistent with experimental observations, hence reproducing the hysteresis behaviour of turbulent lifted flames.

The predictions with different models for the conditional scalar dissipation rate and the presumed PDF of the mixture fraction were very similar, suggesting that this modelling aspect of CMC is not very critical for this problem.

The stabilisation mechanism was explored by quantifying the balance of terms in the 2D-CMC equation in the lift-off region. It was found that, in agreement with experimental data, the conditional scalar dissipation rate at the stabilisation height was well below the extinction value. The heat release term and the axial diffusion balanced axial convection and diffusion in mixture fraction space, with the radial components of convection and diffusion being always very small. This justifies previous approaches with a cross-stream averaged CMC, which seems to be adequate for jet problems. The present results also suggest that first-order CMC is adequate for flame stabilisation problems.

4.5 Figures

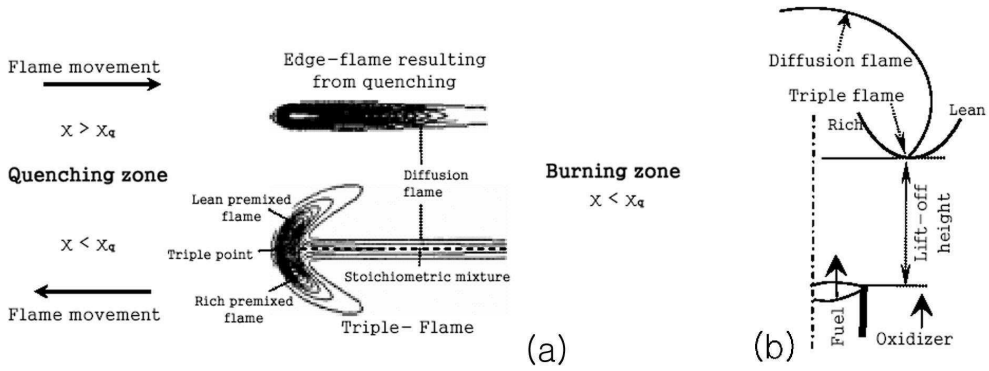

Figure 4.1: Triple and Leading-edge flame structure. (a) Structure of triple and leading-edge flame (Vervisch, 2000; Veynante and Vervisch, 2002), (b) Schematic sketch showing the location of the triple flame (Ghoasl and Vervisch, 2001; Buckmaster, 2002)

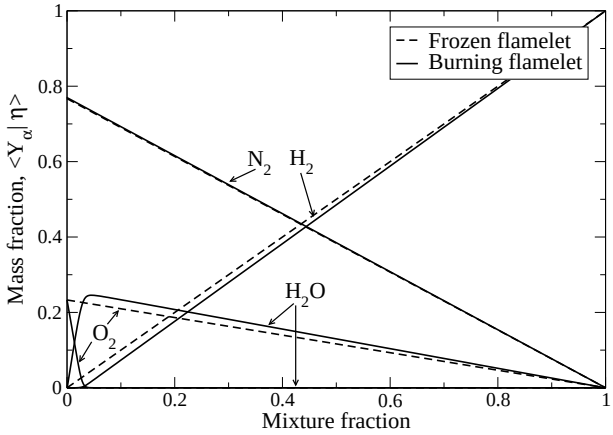

(a) Conditional mean mass fractions of major species

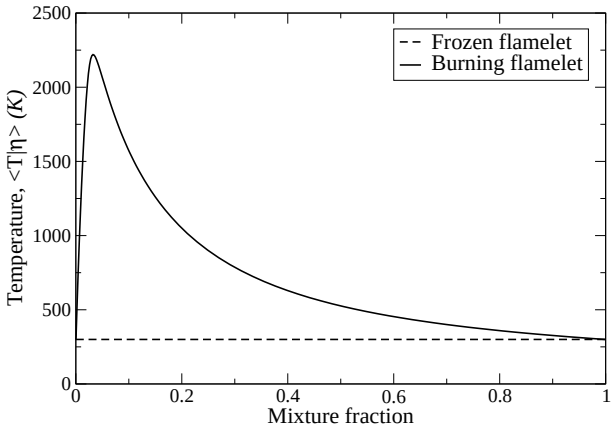

(b) Conditional mean temperature

Figure 4.2: Conditional mean mass fractions and temperature, Comparison of frozen and burning flamelet with $\langle N|\eta = 0.5\rangle = 10\ s^{-1}$.

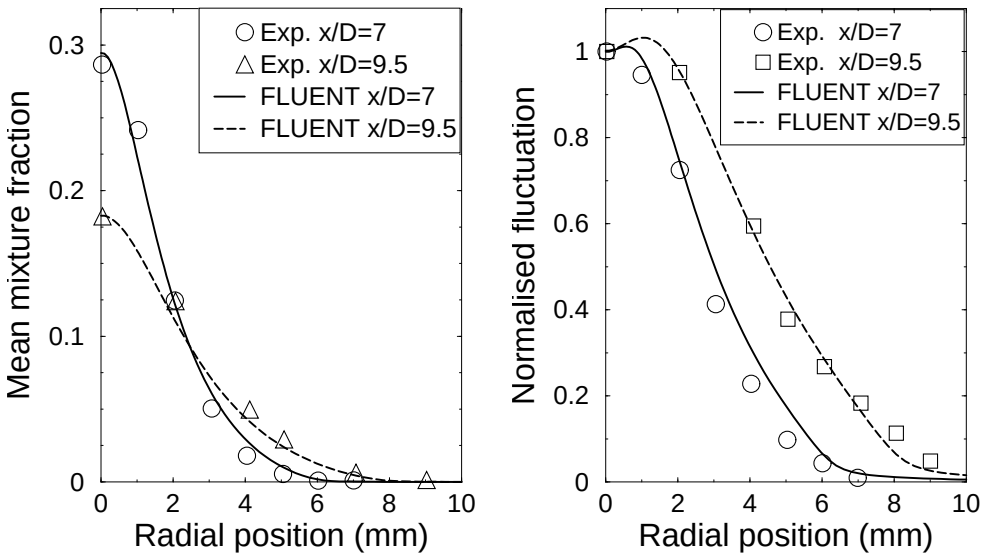

(a) Mean mixture fraction

(b) Mixture fraction r.m.s.

Figure 4.3: Radial profiles of mean and r.m.s. mixture fraction from computations and experiment (Cheng et al., 1992).

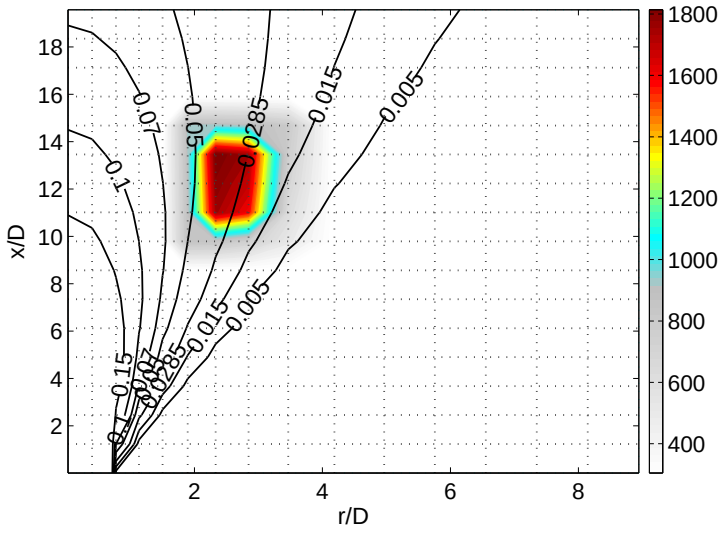

Figure 4.4: Initial mean temperature condition of downstream ignition, ignited at $x/D = 12$ and $0.018 < \tilde{\xi} < 0.04$, (stoichiometry $\tilde{\xi}_{st} = 0.0285$). Iso-lines of the mean mixture fraction are superimposed for pure H_2, $U_{jet} = 680m/s$. The dotted lines correspond to the CMC physical space grid.

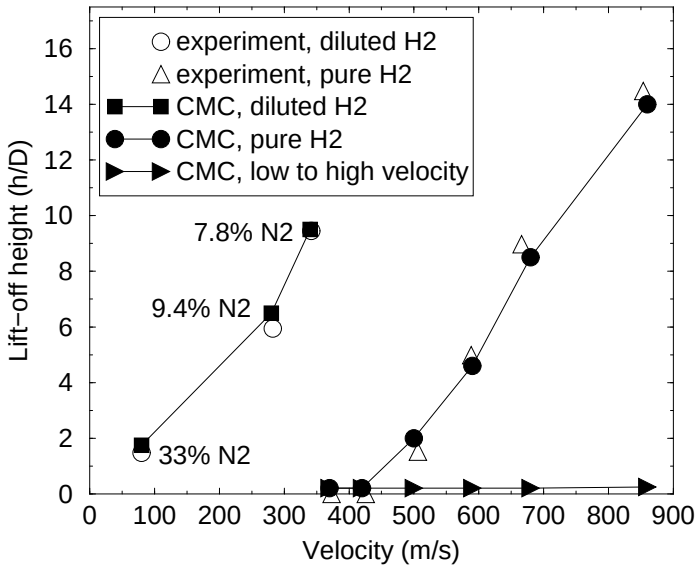

Figure 4.5: Lift-off height vs. jet velocity for pure and diluted H_2 flames. Experimental data from Brockhinke et al. (2000).

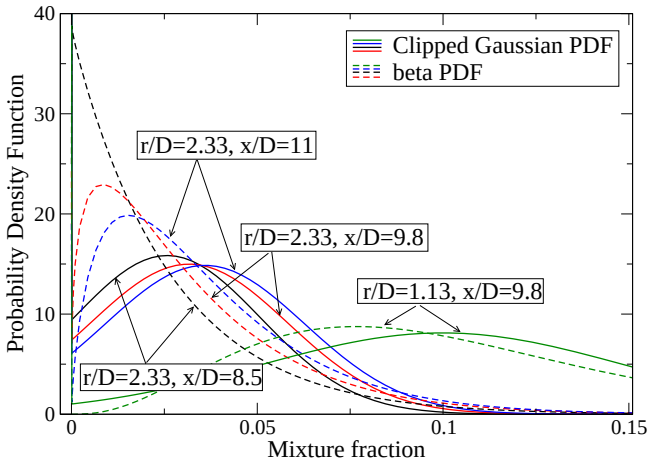

Figure 4.6: Probability Density Function around the flame base for pure H_2, $U_{jet} = 680m/s$.

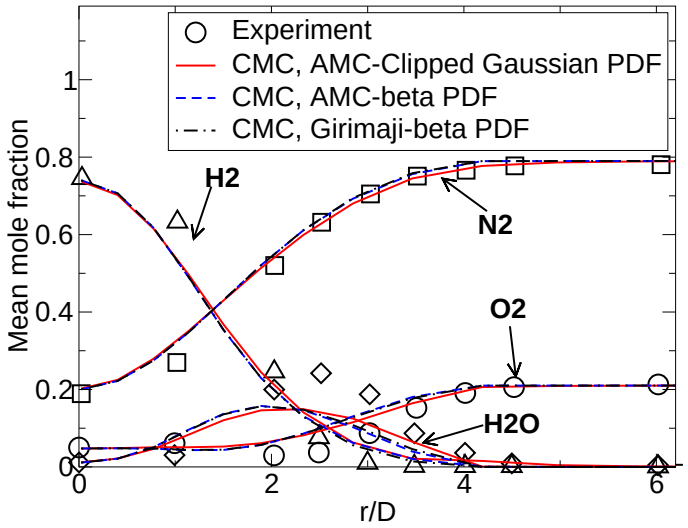

Figure 4.7: Radial profiles of mean mole fractions at $x/D = 9.5$, pure H_2, $U_{jet} = 680m/s$. Data from Cheng et al. (1992).

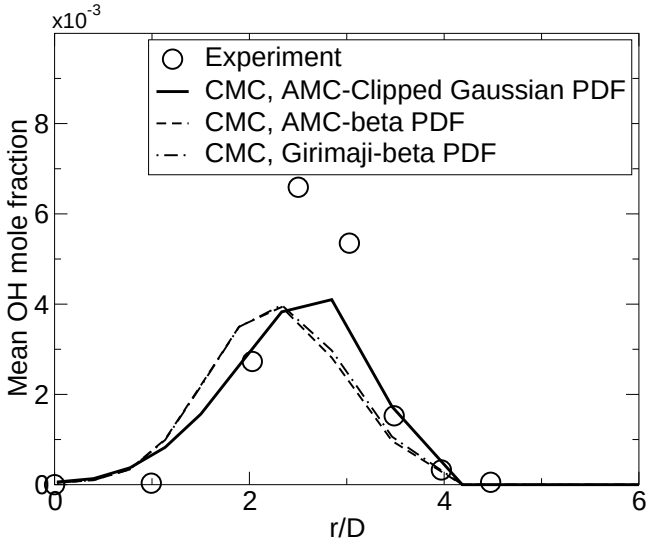

Figure 4.8: Radial profiles of the mean averaged OH mole fraction at $x/D = 9.5$, pure H_2, $U_{jet} = 680m/s$. Data from Cheng et al. (1992).

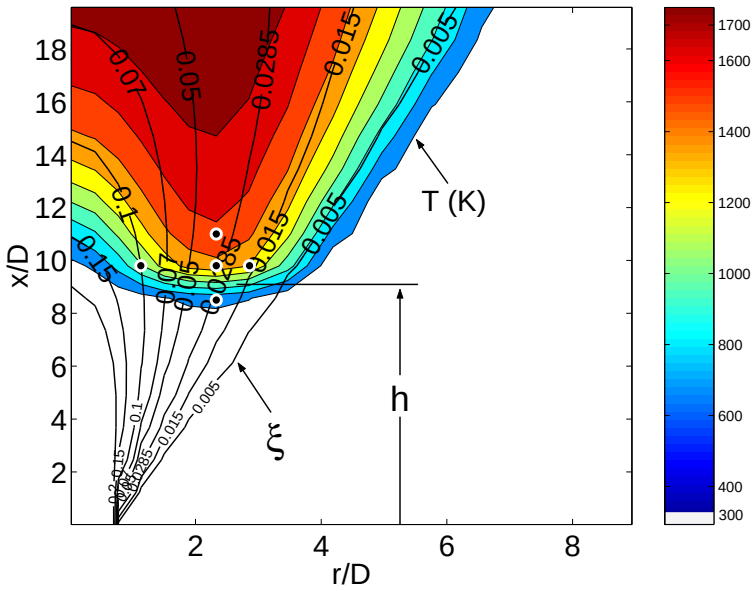

Figure 4.9: Contours of mean temperature with the mean mixture fraction iso-lines superimposed for pure H_2, $U_{jet} = 680m/s$.

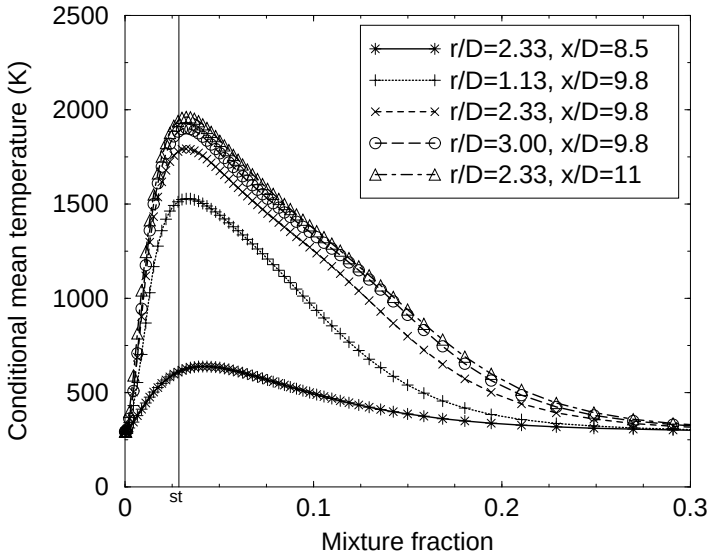

Figure 4.10: Conditional mean temperature for pure H_2, $U_{jet} = 680m/s$.

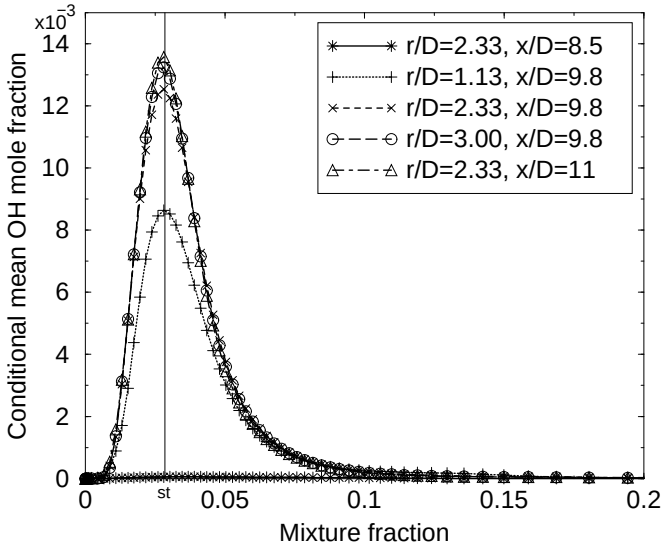

Figure 4.11: Conditional mean OH mole fraction for pure H_2, $U_{jet} = 680m/s$.

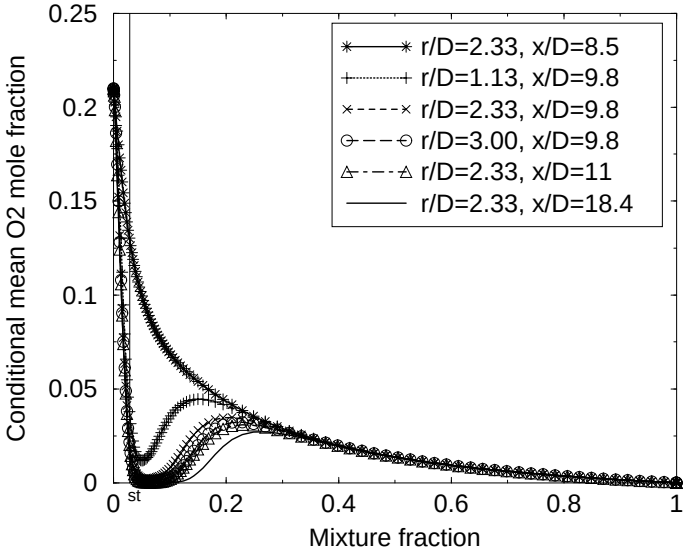

Figure 4.12: Conditional mean O_2 mole fraction for pure H_2, $U_{jet} = 680m/s$.

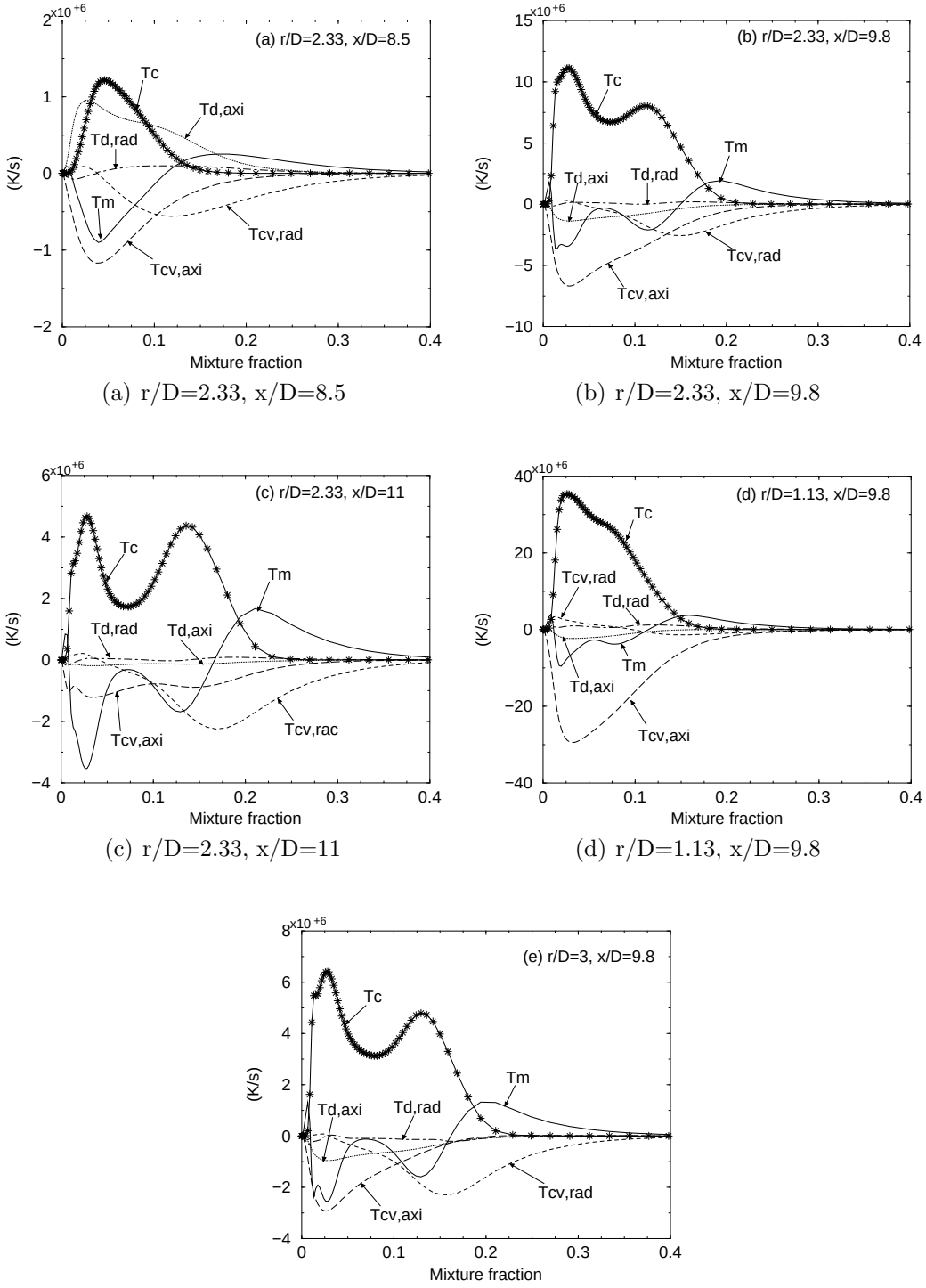

(a) r/D=2.33, x/D=8.5

(b) r/D=2.33, x/D=9.8

(c) r/D=2.33, x/D=11

(d) r/D=1.13, x/D=9.8

(e) r/D=3.0, x/D=9.8

Figure 4.13: The terms in the CMC equation for the conditional temperature around the lift-off region for pure H_2, $U_{jet} = 680m/s$. The corresponding locations are indicated in Figure 4.9.

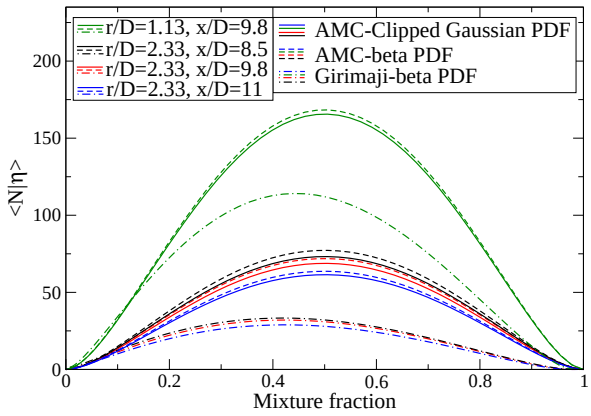

Figure 4.14: Conditional scalar dissipation rate, $\langle N|\eta\rangle$, around the lift-off height for pure H_2, $U_{jet} = 680m/s$.

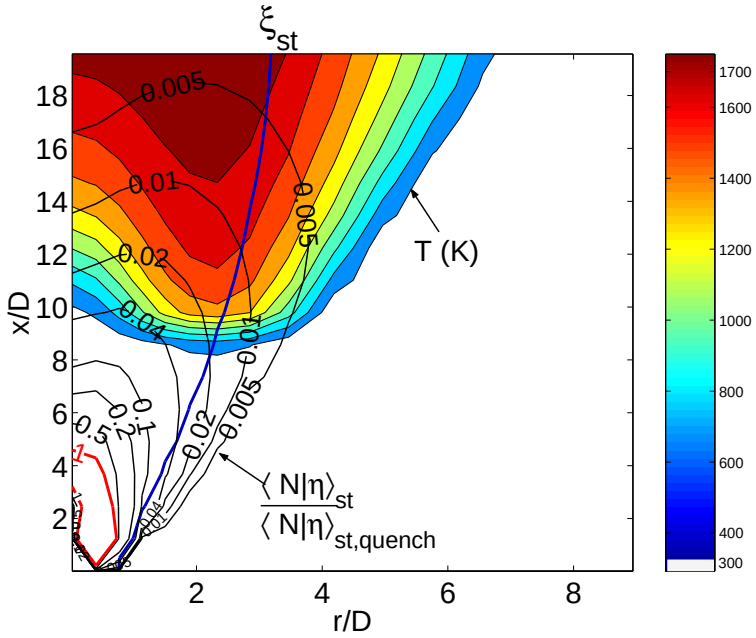

(a) $\langle N|\eta\rangle$ AMC model with Clipped Gaussian PDF

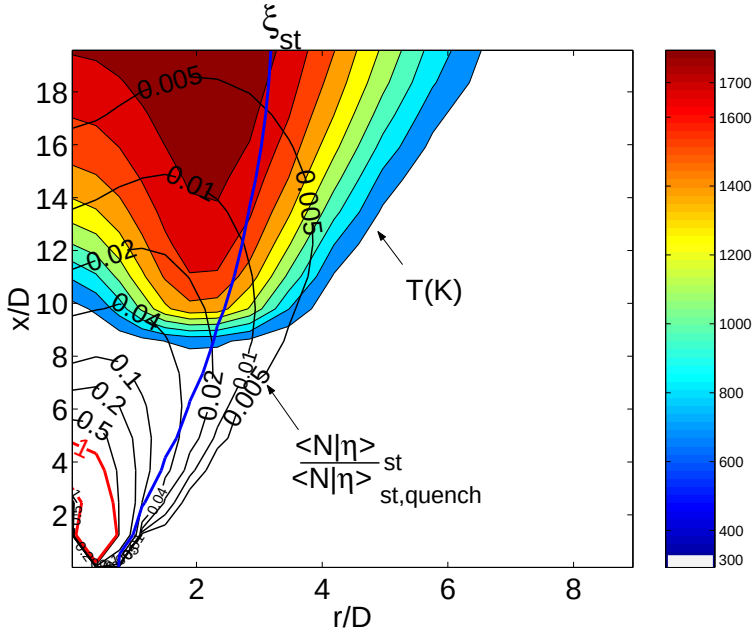

(b) $\langle N|\eta\rangle$ AMC model with beta PDF

Figure 4.15: Iso-lines of conditional scalar dissipation rate (AMC model) $\langle N|\eta = \xi_{st}\rangle$ normalised by its quenching value ($73\ s^{-1}$) superimposed on mean temperature contours. The thick line indicates the iso-line $\tilde{\xi} = \xi_{st}$ for pure H_2, $U_{jet} = 680m/s$.

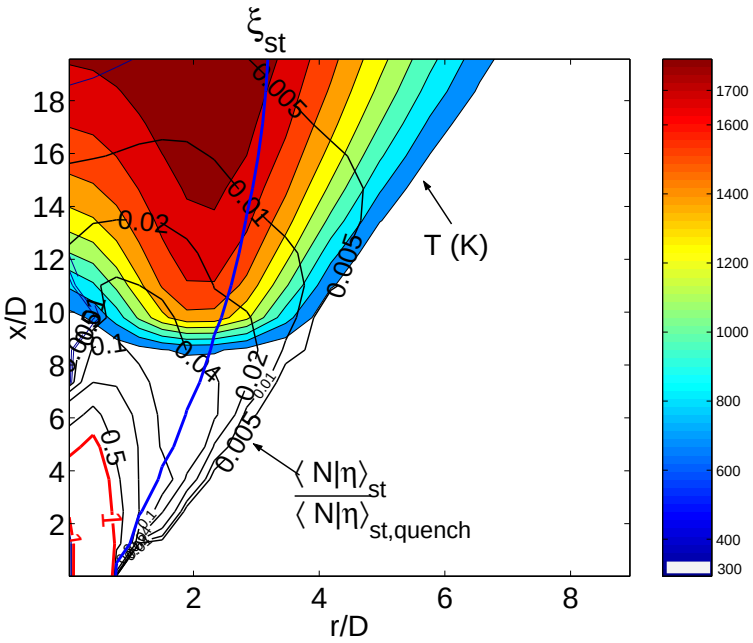

Figure 4.16: Iso-lines of conditional scalar dissipation rate (Girimaji model) $\langle N|\eta = \xi_{st}\rangle$ normalised by its quenching value (73 s^{-1}) superimposed on mean temperature contours. The thick line indicates the iso-line $\tilde{\xi} = \xi_{st}$ for pure H_2, $U_{jet} = 680m/s$.

Chapter 5

Turbulent non-premixed counterflow flames

In this chapter, turbulent counterflow (partially premixed and non-premixed) flames between two opposed jets are described and examined in terms of comparison with experimental data for the flame structure and extinction limits.

5.1 Background

Turbulent twin premixed counterflow flames have been examined by Kostiuk et al. (1989, 1993a,b, 1999) and Mastorakos (1993). Theses flames were formed in the stagnation region between two identical turbulent opposed jets of premixed propane or methane and air. The extinction limits have been measured and related to the total stretch rate acting on the flame. The total stretch rate was estimated as the sum of the bulk flow strain rate (i.e. the velocity gradient perpendicular to the stagnation streamline) and small scale turbulent strain rate. Near extinction, parts of the two separated flames were observed to collide and merge to produce local extinctions. An effect of

buoyancy was also observed (Kostiuk et al., 1999).

Mounaïm-Rousselle and Gökalp (1994) studied experimentally a twin-flame arrangement with air coflow to reduce the unsteady flame axial motion called "bouncing" by Kostiuk et al. (1993b). Extinction occurred when the distance of two burners were small, while dilution by the external air caused extinction for large distance of the burners.

Bray et al. (1991) analysed numerically a single and double premixed flame (Kostiuk et al., 1989) and characterized the extinction by a critical Damköhler number. A single reaction zone in the single reactant stream was thickened as the Da number decreased (i.e. rate of strain increased). Two separate reaction zones were formed in the two reactants streams and small values of the Da number caused these zones to merge and extinction occurred. Further analysis were made by Bray et al. (1996) using different inlet conditions with enthalpy variations.

The turbulent non-premixed and partially premixed counterflow flames are examined in this Chapter. A turbulent diffusion counterflow hydrogen jet against a wider and slower turbulent air stream was examined in terms of strain rate by Goix and Talbot (1991) and high instantaneous stretch rate was observed in the stagnation zone. Kitajima et al. (1996, 2000) studied experimentally methane-air turbulent non-premixed counterflow flames and the bulk strain rate and the Da number determined the extinction.

Mastorakos et al. (1992a) measured extinction in non-premixed and partially premixed natural gas flat flames with N_2 coflow and achieved the extinction by increasing the bulk velocity, decreasing the burner distance, increasing the turbulent intensity and decreasing the air volume fraction.

Extinction at a critical total strain rate equal to the critical strain rate for extinction for laminar counterflow flames was suggested. The partial premixing (i.e. dilution of the fuel with air) made the flame more strain resistant. Mastorakos et al. (1992b) studied this flow numerically and concluded that the fluctuation of mixture fraction increased as the bulk strain rate decreases. The mean scalar dissipation rate increased with increasing bulk strain rates and extinction occurred at a critical mean scalar dissipation rate for the whole spectrum of flames. Omar et al. (2004) also investigated methane-air counterflow flames and concluded that the flame extinction was driven by strain effects rather than severe flame wrinkling.

In Geyer et al. (2003, 2005b,a), a turbulent partially premixed counterflow methane/air flames were studied experimentally and compared with large eddy simulations and Monte Carlo PDF simulations. The experiment showed that the mean mixture fraction was almost unaltered by chemical reactions and heat release, but a decrease in the mixture fraction fluctuation was found in the reacting flows. Local maxima and a strong increase of scalar dissipation rate were observed on the rich mixture side for burning flow. The large eddy simulation presented good agreements with the experiment using a value of $Sc = 0.45$ and differences of the scalar dissipation rate were found on the rich side. The Monte Carlo PDF simulations overestimated the extinction limits and showed also large discrepancies on the rich mixture side. The previous work of the Monte Carlo PDF simulations by Eckstein et al. (2000) used high C_D (appeared in the Section 2.2.3). $C_D = 2$ gave 80% larger r.m.s. of the mixture fraction and $C_D = 10$ produced reasonable agreements with the data (Mastorakos, 1993; Mastorakos et al., 1992a) but even at $C_D = 10$

over-prediction of the mixture fraction r.m.s. were observed. A key feature of mixing in opposed jet flows is that the residence time is less than the turnover time of the turbulence. This suggests "early mixing" characteristics, i.e. large fluctuations of the mixture fraction (Geyer et al., 2003, 2005b,a; Mastorakos et al., 1992b), bimodal PDFs (Mastorakos, 1993; Stapountzis et al., 1986; Eswaran and Pope, 1988) and large C_D values (Eckstein et al., 2000). These points will be used repeatedly later on during discussion of the predictions.

In this Chapter, the first order CMC simulations are compared with experimental data from Mastorakos et al. (1992a), Mastorakos (1993) and Geyer et al. (2003, 2005b). Turbulent counterflow non-premixed flame simulations by CMC have not been performed yet by others, to the author's knowledge. An attempt is also made to predict extinction limits in order to explore the range of applicability of the first order CMC.

5.2 Turbulent counterflow flames simulations

5.2.1 Experimental configuration

The experiments of non-premixed and partially premixed turbulent counterflow flames with N_2 coflow have been performed and the data were described by Mastorakos et al. (1992a); Mastorakos (1993); Geyer et al. (2003, 2005b). Figure 5.1 shows the burners arrangement which comprised two opposed jets and N_2 coflows. The diameters of the jet (D_i) is $25.4mm$ for Mastorakos (1993) and $30.0mm$ for Geyer et al. (2003, 2005b) and the diameters (D_o) of N_2 coflow is twice of the jet diameter. The distance of the opposed jets is one diameter of the jet. The burner design and experiments followed the

characteristic of Mastorakos (1993). The flow stagnated at the center of the jets and was controlled by the momentum flow rates of the two jets i.e. $(\rho U^2)_{air} = (\rho U^2)_{fuel}$. The extinction limits were measured by the increase of the velocity by a $0.05 m/s$ stepping, both in the experiment and in the simulation.

The fuel composition and velocity field are shown in the Table. 5.1 and Table. 5.2. The normalised turbulent intensity ($\sqrt{u'^2 + 2v'^2}/U$, u' and v' are axial and radial r.m.s. velocity) was 8.5% and this value was used as initial condition for the CFD calculation.

Species	Mass fraction		Velocity
CH_4	10.38%	U_{air}	3.4 m/s
O_2	20.87%	U_{fuel}	$\sqrt{\frac{\rho_{air}}{\rho_{fuel}} U_{air}}$
N_2	68.75%	$U_{N_2,coflow}$	1.13 m/s

Table 5.1: Fuel composition and velocity condition of Geyer et al. (2003, 2005b). Stoichiometric mixture fraction $\xi_{st} = 0.5315$.

Velocity (m/s)	$U_{air} = 1.48$	$U_{fuel} = \sqrt{\frac{\rho_{air}}{\rho_{fuel}} U_{air}}$	$U_{N_2,coflow} = 0.5$
Air volume fraction in fuel stream	X=0.0	X=0.5	X=0.8
Stoichiometric mixture fraction	$\xi_{st} = 0.055$	$\xi_{st} = 0.1544$	$\xi_{st} = 0.452$
Species	Mass fraction	Mass fraction	Mass fraction
CH_4	100%	35.74%	12.2%
N_2	–	49.29%	20.46%
O_2	–	14.97%	67.34%

Table 5.2: Fuel composition and velocity condition of Mastorakos (1993).

5.2.2 Flow field

The flow field information is calculated by a commercial CFD software, FLUENT run for inert or reacting flow with its own flamelet model. The grid of axisymmetrical computation domain is 250×170 nodes in $1D_i \times 1D_i$ axial and radial direction respectively, a resolution which is fine enough to compute grid independent solutions. The boundary conditions for the FLUENT are taken as inlet-flow, out-flow, wall and axisymmetry. The inlet conditions are specified by the experiments' measured profile at the exit of nozzle and the turbulent intensity. The inlet for the coflow was N_2 in the experiment. This is a three-stream problem and so single mixture fraction based approaches can not treat it. Hence air was considered as the coflow in the simulations. This configuration produced flame at the exit of coflow on the fuel side and could affect downstream profiles. However, our main interest is along the centre line and this flame does not affect the flow there.

Chou et al. (2004) suggests that the Reynolds stress model with linear pressure-strain correlation by Launder et al. (1975) shows overall the best agreement with the experiment (Mastorakos, 1993) among the turbulent models tested ($k - \varepsilon$ model and another Reynolds stress model with non-linear pressure-strain correlation). Hence, the Reynolds stress model with flamelet model is used here to provide the flow field information to the CMC calculation.

Comparisons between CFD simulation by FLUENT and the experiment data by Geyer et al. (2003, 2005b) are following. Figure 5.2 shows the inert counterflow mean mixture fraction and r.m.s. and presents good agreement

with the experiment (Geyer et al., 2003, 2005b) with standard Reynolds stress model ($Sc = 0.7$ and $C_D = 2$) by FLUENT. For the reacting counterflow, Schmidt number Sc and C_D are modified to match the experimental data. In Figure 5.3, the mixture fraction r.m.s. decreases by combustion (Geyer et al., 2003) and the standard model can not capture the mixture fraction r.m.s., as also presented by Eckstein et al. (2000). The mean mixture fraction profiles show good agreement with the data (Figure 5.4). The simulations with $C_D = 14$ with $Sc = 0.6$ and 0.7 give overall the most accurate results.

Figure 5.5 shows the radial profiles of velocity, normalised velocity fluctuation and turbulent kinetic energy at $5mm$ from the fuel nozzle and excellent agreement with the experiment is evident. The initial profiles are supplied as the experiment's nozzle exit profile. Figure 5.6 presents good agreement of axial velocity with the experiment. An increase of C_D alters the profile a little near the stagnation point. The normalised velocity r.m.s. shows an overprediction of the turbulence presented in Figure 5.7, a similar behaviour was also observed in the Monte Carlo PDF simulation (Geyer et al., 2005b). We conclude that FLUENT with its own flamelet model predicts adequately the main velocity and mixture fraction field structure of counterflow non-premixed flames. It is also evident that to predict the right level of the mixture fraction r.m.s., C_D has to increase from its standard value of 2 to values as high as 14, as also seen by Eckstein et al. (2000) and Maury and Libby (1995).

5.2.3 Numerical methods

The first order CMC calculation has been performed with a detailed mechanism (Smooke et al., 1986) which consists of 16 species with 25 reactions. Zero-, one- and two-dimensional CMC codes are applied (no spatial convection/diffusion in zero dimensional CMC). The computational domain for the CMC calculation is set between $1D_i \times 0.45D_i$, axial and radial direction, to avoid interference of the unwanted flame caused by using air in the coflow. The CMC0D calculation uses an integrated version of the CMC equation with the scalar dissipation given by Eq. (2.32). The PDF weighted average of the scalar dissipation rate is considered and averaged along the axis. The AMC model (presented in Section 2.2.3) for the conditional scalar dissipation rate and linear model for the conditional velocity (presented in Section 2.2.2) were used. 91 nodes of the mixture fraction space with various spatial griding are used. The inlet and outlet conditions are used in physical space and other conditions are the same as described in the previous Chapters.

The governing equation of CMC for the temperature and the species are analysed in spatial and mixture fraction space. The governing equation for the conditional temperature and species can be re-written from Eq. (2.13) and Eq. (2.18):

$$\begin{aligned}\frac{\partial Q_\alpha}{\partial t} &= \underbrace{-\langle u_i|\eta\rangle \frac{\partial Q_\alpha}{\partial x_i}}_{Q_{cv}} \underbrace{+\langle N\,|\,\eta\rangle \frac{\partial^2 Q_\alpha}{\partial \eta^2}}_{Q_m} \underbrace{+\frac{\langle \omega_\alpha|\eta\rangle}{\langle \rho|\eta\rangle}}_{Q_c} \\ &\quad \underbrace{-\frac{1}{\overline{\rho}\widetilde{P}(\eta)}\frac{\partial}{\partial x_i}\Big(\langle u_i'' Y_\alpha''|\eta\rangle\, \overline{\rho}\widetilde{P}(\eta)\Big)}_{Q_d} \end{aligned} \tag{5.1}$$

$$\frac{\partial Q_T}{\partial t} = \underbrace{-\langle u_i|\eta\rangle \frac{\partial Q_T}{\partial x_i}}_{T_{cv}} + \underbrace{\langle N|\eta\rangle \frac{\partial^2 Q_T}{\partial \eta^2} + \langle N|\eta\rangle \left[\frac{1}{\langle c_P|\eta\rangle}\left(\frac{\partial \langle c_p|\eta\rangle}{\partial \eta} + \sum_{\alpha=1}^{n} c_{p\alpha} \frac{\partial Q_\alpha}{\partial \eta}\right)\right] \frac{\partial Q_T}{\partial \eta}}_{T_m}$$
$$\underbrace{-\frac{1}{\bar{\rho}\tilde{P}(\eta)} \frac{\partial}{\partial x_i}\left(\langle u_i'' T''|\eta\rangle \bar{\rho}\tilde{P}(\eta)\right)}_{T_d} + \underbrace{\frac{\langle \omega_h|\eta\rangle}{\langle \rho|\eta\rangle\langle c_p|\eta\rangle}}_{T_c} \tag{5.2}$$

In Eqs. (5.1) and (5.2), the subscripts of cv and d terms are for spatial convection and diffusion and m correspond to molecular diffusion (i.e. mixing in mixture fraction space). Pressure is assumed constant and hence the pressure work term is neglected.

5.3 Results and discussion

5.3.1 Unconditional averages

Figure 5.8 shows the mean temperature profile with superimposed contour lines of normalised conditional scalar dissipation rate by its quenching rate at the stoichiometry and the stoichiometric mixture fraction. x is axial direction from the lower jet (fuel) and r is radial distance from the axis. The quenching conditional scalar dissipation rate at the stoichiometry ($\xi_{st} = 0.5315$) is 377.34 s^{-1}, which was calculated by a homogeneous CMC0D (no spatial convection and diffusion). The conditional scalar dissipation rate is well below its quenching level so that the flame is stable. The maximum temperature lies near the stagnation point ($x = 0.015$) and the stoichiometric mixture fraction.

Figure 5.9 shows a comparison of the unconditional temperature averages along the axis of the jets with CMC1D and CMC2D. CMC1D stands for the one-dimensional CMC calculation only taken along the axis value

without radial direction component. CMC2D is for two-dimensional CMC. The FLUENT run with $Sc = 0.6$ and $C_D = 14$ provide the most accurate results in CMC1D and CMC2D and these modified values are used for the CMC calculation. The flamelet calculation by FLUENT produces overprediction of the mean temperature. An increase of C_D and a decrease of the Sc number give a decrease of the mixture fraction r.m.s. (Figure 5.3) and an increase of the temperature (Figure 5.9), but a high C_D value results in high scalar dissipation rate $\widetilde{\chi}$, as expected (Figure 5.10). The calculation using a value of $C_D = 8$ gives good agreement with the mean scalar dissipation rate from the experiment, however an underprediction of temperature is observed in Figure 5.9, despite the fact that the r.m.s. of mixture fraction are well predicted with $C_D = 8$.

Figure 5.11 shows the CMC1D calculation for mean mass fractions of major species. An underprediction of O_2 and an overprediction of H_2O are observed. In Figure 5.12, the CMC1D calculation shows overprediction of CO, but the general experimental trends (Mastorakos, 1993) are captured well.

5.3.2 Conditional averages

Figure 5.13 shows that two different conditional scalar dissipation rates are presented by the experiment in same conditions, i.e. curve fit A for Geyer et al. (2003) and curve fit B Geyer et al. (2005a). Different conditional scalar dissipation rate models are also presented i.e. the AMC model with Clipped Gaussian PDF and beta PDF, the Girimaji model and the initial idea of $\langle N|\eta\rangle = \frac{1}{2}\widetilde{\chi}(\eta = \widetilde{\xi})$ by Bilger (1993). The conditional scalar dissipation rate

($\langle N|\eta\rangle_{st} = 98.13\ s^{-1}$) from the value of $Sc = 0.6$ and $C_D = 14$ and the AMC model with beta PDF gives reasonable agreement with experiment, curve fit A (Geyer et al., 2003) in the very rich mixture side ($\eta > 0.7$), but shows a discrepancy in the lean side and the rich side ($\xi_{st} < \eta < 0.7$) where a local peak appears. The AMC model with Clipped Gaussian PDF and the Bilger's model give underprediction and the Girimaji model gives overprediction compared to the experiment (Geyer et al., 2003). The AMC model with beta PDF provides the closest value to the experiment (Geyer et al., 2003) among the four different conditional scalar dissipation rate models, however none of them can capture the local peak on the rich mixture side. The AMC model with beta PDF captures the stoichiometric conditional scalar dissipation rate well compared to the experiment (Geyer et al., 2003). For the curve fit B (Geyer et al., 2005a), the conditional scalar dissipation rate at the stoichiometry is about 2 times less than the AMC model with beta PDF and a very large local peak is observed on the rich mixture side. In order to capture the conditional scalar dissipation rate of the experiment for the local peak in the rich side, the conditional scalar dissipation rate is needed to increase by factor of 2 or 3 from $\langle N|\eta\rangle_{st} = 98.13\ s^{-1}$. It is not clear why different conditional scalar dissipation rates are reported in the experiments for the same conditions, it may be related to the fact that 45% experimental error of scalar dissipation rate was reported by Geyer et al. (2005a).

Figure 5.14 presents the comparison of conditional mean profiles of temperature, H_2O and CH_4 mass fractions. The CMC0D and CMC1D gives good agreements on the lean side ($\eta \leq \xi_{st}$), but discrepancies are observed on the rich side ($\xi_{st} < \eta < 0.8$) and the large experimental error can be also

seen. The profiles with high conditional scalar dissipation rate, artificially increased by factor of 3, provides overall better match, but underprediction of the conditional temperature is observed in the lean mixture side in Figure 5.14 (a) and overprediction of the conditional H_2O mass fraction is still presented in Figure 5.14 (b). The profiles with curve fit A and B of the experiment give similar profiles of the AMC model with beta PDF. The curve fit B decreases the discrepancy between $\xi_{st} < \eta < 0.8$, this may due to the large local peak of $\langle N|\eta \rangle$, despite the fact that the stoichiometric conditional scalar dissipation rate is two times lower than the AMC model with beta PDF and the curve fit A. In order to achieve the correct profiles, less $\langle N|\eta \rangle$ in the lean side and higher $\langle N|\eta \rangle$ in the rich mixture side is needed.

Figure 5.15 presents the comparison of the mixture fraction PDFs between prediction and experiment. The experiment show PDF shapes which have 3 peaks, while the presumed PDF is bimodal. The beta PDF and Clipped Gaussian PDF could not reproduce the experimental PDF. This may be an additional reason why, despite the good prediction of the unconditional scalar dissipation rate (Figure 5.10), the conditional scalar dissipation rate is not predicted well (Figure 5.13).

In Figure 5.14, conditional temperature, H_2O and CH_4 mass fractions from all CMC nodes along the axis are included and it is clear that there are small differences due to the difference in the conditional scalar dissipation rate. The red dotted lines on the bottom in Figure 5.14 (a) and (b) and the red dotted straight diagonal lines in Figure 5.14 (c) are the frozen flamelet near to the jets, which is input as a boundary condition to the calculation.

We conclude that i) the overall structure of the flame in mixture fraction

space is predicted accurately with the first order CMC only if the conditional scalar dissipation rate is increased artificially by a factor of 3. ii) the measurements show some scatter but without localized extinction, to the extent that was seen in the Delft flame (Chapter 3). Hence the first order order CMC with proper conditional scalar dissipation rate should be adequate to capture extinction in these flames.

5.3.3 Extinction limits

The extinction limits have been examined using the experimental data by Mastorakos (1993), Mastorakos et al. (1992a) and Geyer et al. (2003, 2005b,a). The extinction limits were achieved by increasing U_{air} by 0.05 m/s progressively to extinguish the flame. In this simulations for extinction limits, the AMC model with beta PDF model for conditional scalar dissipation rate is used, as seen in Figure 5.13, the AMC model with beta PDF gives reasonably agreement with the curve fit A (Geyer et al., 2003).

Figure 5.16 shows the conditional scalar dissipation rates of the AMC model and the curve fits A and B for Geyer et al. (2003) and Geyer et al. (2005a) scaled and increased to cause the flame extinction. The AMC model with beta PDF gives that at the lean side ($\xi \approx 0.5$), the scalar dissipation rate is above the quenching level while at the rich side ($\xi > 0.5315$) it is below the quenching level. The curve fits give the opposite profiles of the AMC model.

Table 5.3 shows the extinction velocity limits by CMC0D calculation for the experiment (Geyer et al., 2003, 2005b,a) and compared with different conditional scalar dissipation rates i.e. the AMC model and the curve fit A

from Geyer et al. (2003), as seen in Figure 5.16. The curve fit A shows higher extinction velocity than the AMC model due to high $\langle N|\eta\rangle$ in Figure 5.16. Despite the experimental conditional scalar dissipation rate being used, capturing the extinction velocity by CMC0D calculations is not successful.

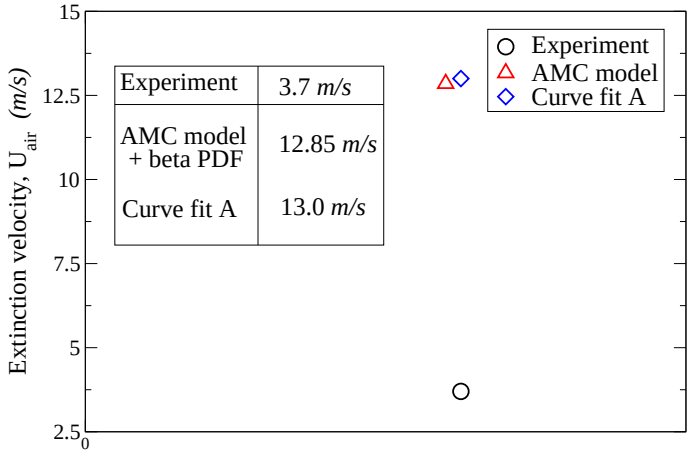

Table 5.3: Extinction velocity limits for Geyer et al. (2003, 2005b,a).

Figure 5.17 shows that the quenching conditional scalar dissipation rate at stoichiometry increase linearly as the velocity of jets increase. Higher air volume fractions in fuel stream, $X = 0.5$ and $X = 0.8$, produce steeper increases and higher quenching level compared to $X = 0.0$. Figure 5.18 shows the measured extinction velocity versus the air volume fraction in fuel stream compared with CMC0D and CMC2D calculations. Large discrepancies between the CMC calculations and the experiment are observed, however they capture the trend reasonably well. The differences are about the factor of 3 or 4 times large than the experiment in CMC predictions and the right conditional scalar dissipation rate could bring accurate prediction, consistent with

the observation of Figure 5.14 that the predicted conditional temperature seems as if it is being calculated with a smaller conditional scalar dissipation rate.

In the CMC2D calculation, the flame stays alight even at the velocity corresponding to the extinction limit of the CMC0D. The extinction occurs at $U_{air} = 6.83\ m/s$ that is about 5% higher than CMC0D. However, the CMC2D shows the same trend as the CMC0D, which implies that the importance of spatial terms at the extinction are small.

Figure 5.19 presents the CMC2D calculation at $X = 0.0$ and the maximum temperature is located on the rich mixture side (fuel jet side). The temperature contours at low velocity with stable flame are shown in Figure 5.19 (a). Figure 5.19 (b) shows a CMC2D calculation of a flame at a velocity close to extinction, although this velocity is higher than the velocity needed to extinguish of CMC0D simulations. As the velocity increases, the flame is thinner and has a lower temperature and an increase of the scalar dissipation rate is observed. The quenching scalar dissipation rate was calculated by the homogeneous CMC and is 15.35 s^{-1} at the stoichiometry mixture fraction for this air dilution. In Figure 5.19 (b), the normalised quenching scalar dissipation rate ($\frac{\langle N|\eta\rangle_{st}}{\langle N|\eta\rangle_{st,\ quench}} = 1$) covers most of the flame zone, however, the stoichiometry is outside of the quenching scalar dissipation rate zone. Figure 5.19 (c) shows a simulation of CMC2D without spatial convection and diffusion terms and it is clear that the flame only establishes outside of the quenching scalar dissipation rate zone and that the temperature is low inside the quenching zone. Therefore, the flamelet inside of the quenching scalar dissipation rate receives heat from the outside flamelets and

keeps flame alight, this occurs through the action of the spatial convection and diffusion terms. Eventually, the quenching scalar dissipation rate zone expands as the velocity is increased and the flame will extinguish.

In Figure 5.20, we present the temperature source terms distributions in mixture fraction space at the different locations marked as red and blue dots in Figure 5.19 (b). Figure 5.20 (a) shows that heat is generated at the stoichiometry and balances with the molecular and axial diffusion. The radial components and the axial convection are negligible. In Figure 5.20 (b) at this point $\langle N|\eta\rangle_{st} \gg \langle N|\eta\rangle_{st,quench}$, the flame is inside of the critical quenching zone and the chemistry term is very small, as expected. The heat is received from outside of the quenching zone by the axial convection and diffusion and lost by the molecular diffusion, consistent with the observation in Figure 5.19.

Figure 5.21 and Figure 5.22 show the profiles of the species terms of CMC (Eq. 5.1). The CH_4 species is destructed by the reaction and balanced with the molecular diffusion in Figure 5.21 (a), typical of the structure of a non-premixed flame. The CH_4 species is destructed by axial convection and diffusion and radial diffusion from the downstream and balances with the molecular diffusion in Figure 5.21 (b). It is evident that the CH_4 is not consumed very much inside of the quenching zone and consumed outside of the quenching zone, as shown in Figure 5.21 (c).

In Figure 5.22 (a), the OH is produced at stoichiometry and consumed at rich mixture side ($\eta > 0.06$) and at very lean mixture side ($\eta < 0.04$). It is almost fully balanced by molecular diffusion. In the region where $\langle N|\eta\rangle_{st} > \langle N|\eta\rangle_{st,quench}$, all mixture fractions consume OH by recombination reactions.

The OH reaches that region by axial convection and spatial diffusion in Figure 5.22 (b).

In the temperature terms profile of Figure 5.20, the radial components are negligible, however the radial diffusion is important in the species terms of Figure 5.21 and Figure 5.22 at radial position $r = 0.83mm$ from the axis. At the axis, the radial terms would be zero. The flame inside of the critical quenching zone survives by receiving heat from the outside of the quenching zone by the axial convection and diffusion and minor contribution of radial diffusion closed to the axis (not shown). Therefore, higher velocity is needed so that the critical scalar dissipation rate covers the whole flame to extinguish. The spatial terms are only important to sustain the flame inside the quenching zone to receive heat from the outside quenching zone, with very low chemistry contribution and low CH_4 consumption seen in Figures (5.20-5.22). If there are no heat generation outside of the quenching zone, the flame will be extinguished. Hence, the scalar dissipation rate controls the extinction in this counterflow flame. It is evident that despite the effort to predict the measured mean scalar dissipation rate, the conditional scalar dissipation rate still seems to be underpredicted (Figure 5.13 and Figure 5.14), which results in an extinction velocity prediction higher than the experiment.

5.4 Conclusions

Turbulent counterflow non-premixed and partially premixed flames have been simulated by CMC0D, CMC1D and CMC2D in this Chapter to study the flame structure and extinction limits. The flow field is pre-calculated by FLUENT with Reynolds stress and a flamelet model. Various model con-

stants have been tested including the Schmidt number Sc and the timescale ratio constant C_D. An increase of C_D and a decrease of Sc result in a decrease of the mixture fraction r.m.s. and an increase of the scalar dissipation rate. The C_D is not constant across the flow (Brethouwer, 2000; Eswaran and Pope, 1988) and a model of C_D must be developed to increase accuracy of the prediction of the mixing field.

Using high C_D, i.e. increasing the scalar dissipation rate, can capture the mean temperature profile well, however it can not capture the experimental data (Geyer et al., 2005b) in mixture fraction space. The measured scalar dissipation rate is unsymmetrical and locally peaked on the rich mixture side (Geyer et al., 2003, 2005a). The different shape of conditional scalar dissipation rate between the experiment and model gives some difference in quenching conditional scalar dissipation rate at stoichiometry.

The conditional stoichiometric scalar dissipation rate increases as the velocity increases. In CMC0D, the flame is extinguished at a critical condition and this extinction velocity is higher as the air volume fraction in the fuel stream increases, consistent with experiment. Large discrepancies in the extinction velocity are observed in CMC0D, however the trend is captured reasonably well. In simulations where the experimental conditional scalar dissipation rate is used, capturing the extinction velocity limits by CMC0D calculations is still not successful. The high sensitivity of CMC calculation to the conditional scalar dissipation rate is presented and we conclude that predicting the right conditional scalar dissipation rate is the key point to capture the extinction limits. The experimental measurement should also be more accurate.

The flame stays alight in CMC2D calculations at the critical condition of the CMC0D. The scalar dissipation rate must be higher than the quenching value across the whole flame zone to extinguish the flame. The CMC2D calculations show the same trend of the CMC0D, which implies that the importance of the spatial terms is less than the conditional scalar dissipation rate to extinguish the flame and the spatial terms are important to sustain the flame inside the quenching zone, where the flame receives the heat from outside of quenching zone. Molecular diffusion controls the extinction in regions where $\langle N|\eta\rangle_{st} > \langle N|\eta\rangle_{st,quench}$. In the critical quenching zone, the heat is provided from the outside quenching zone by axial convection and diffusion. Radial diffusion is also important to sustain the flame away from the jet axis.

For more accurate results, an accurate C_D model and scalar dissipation rate model are needed. Regarding conditional fluctuations, the second order CMC could give more accurate results, although the relatively small scatter of the conditional fluctuations seen in the experiment suggest that the first order CMC, with accurate models for conditional scalar dissipation rate and the spatial diffusion terms, could capture extinction of counterflow non-premixed flames.

5.5 Figures

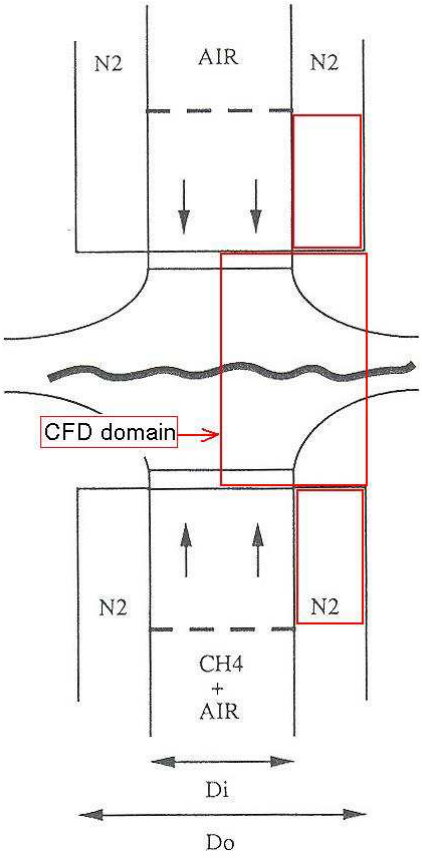

Figure 5.1: Counterflow flame burner arrangement (Mastorakos et al., 1992a; Mastorakos, 1993) and the computational (CFD) domain.

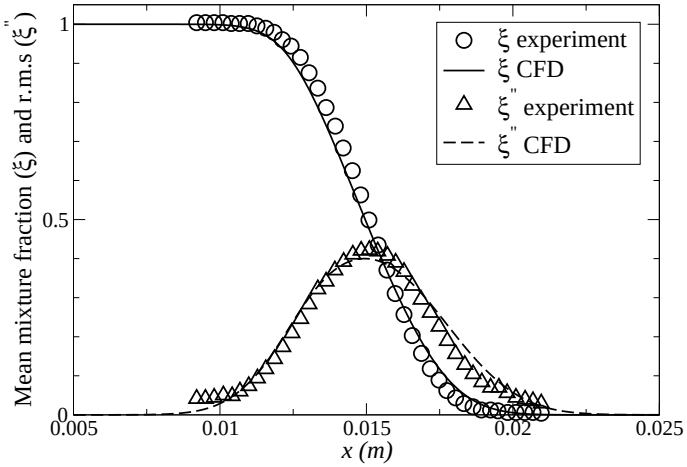

Figure 5.2: Inert counterflow mean mixture fraction and r.m.s., experimental data from Geyer et al. (2003, 2005b,a).

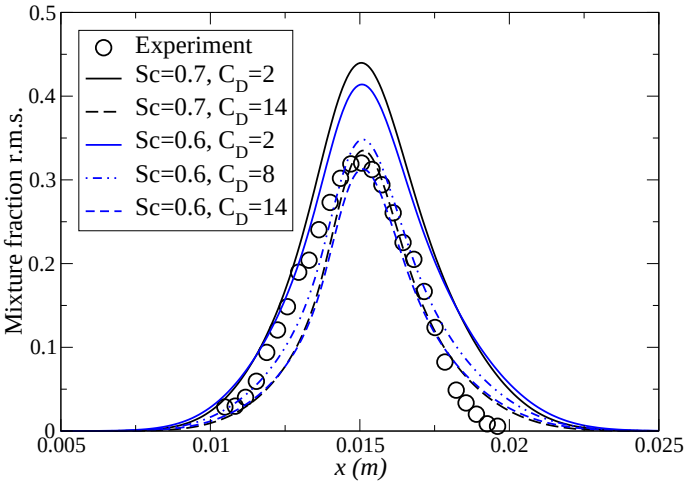

Figure 5.3: Reacting counterflow mixture fraction r.m.s., experimental data from Geyer et al. (2003, 2005b,a).

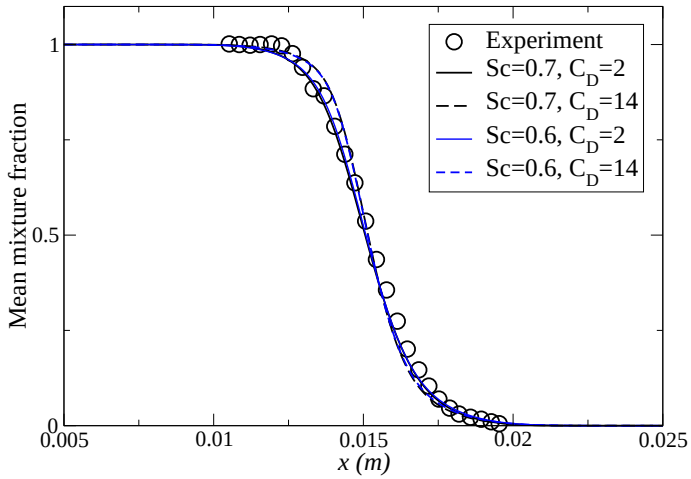

Figure 5.4: Reacting counterflow mean mixture fraction, experimental data from Geyer et al. (2003, 2005b,a).

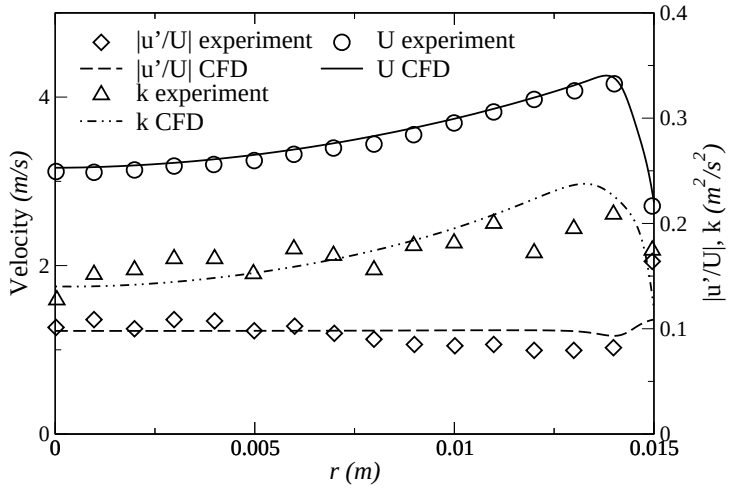

Figure 5.5: Reacting counterflow radial profiles at $5mm$ from the fuel nozzle, experimental data from Geyer et al. (2003, 2005b,a).

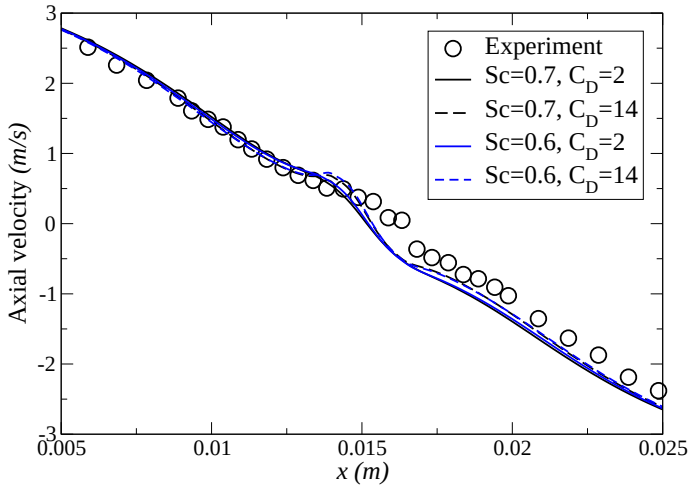

Figure 5.6: Reacting counterflow mean axial velocity profiles, experimental data from Geyer et al. (2003, 2005b,a).

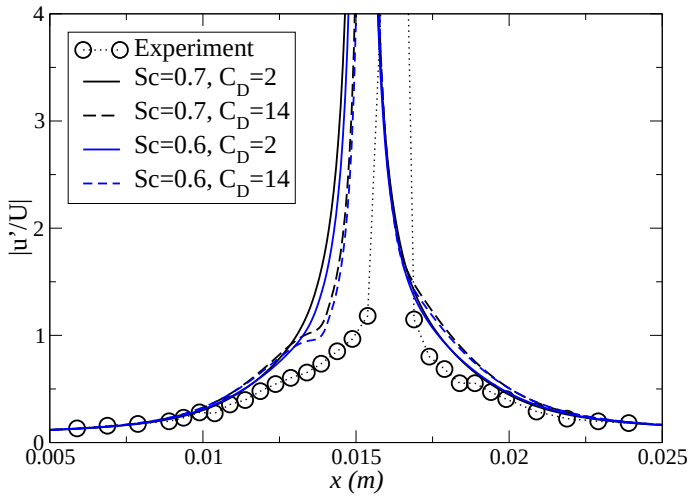

Figure 5.7: Reacting counterflow normalised axial velocity r.m.s. profiles, experimental data from Geyer et al. (2003, 2005b,a).

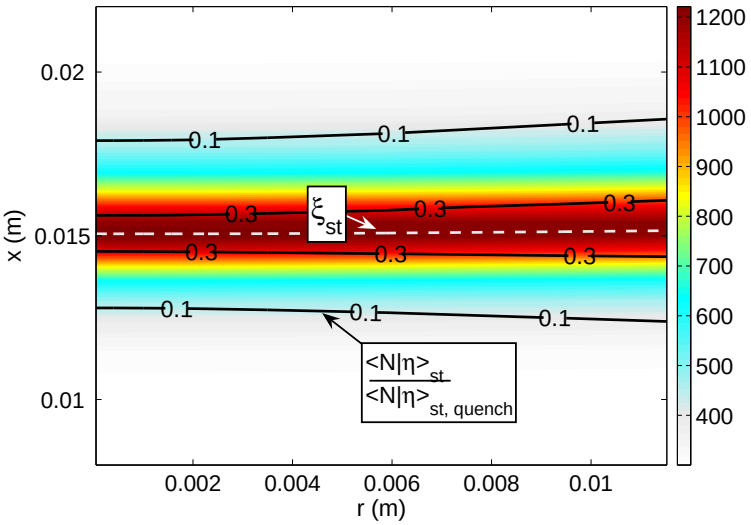

Figure 5.8: Mean temperature contours superimposed on iso-lines of normalised conditional scalar dissipation rate and stoichiometric mixture fraction, $Sc = 0.6$ and $C_D = 14$, test case for Geyer et al. (2003, 2005b).

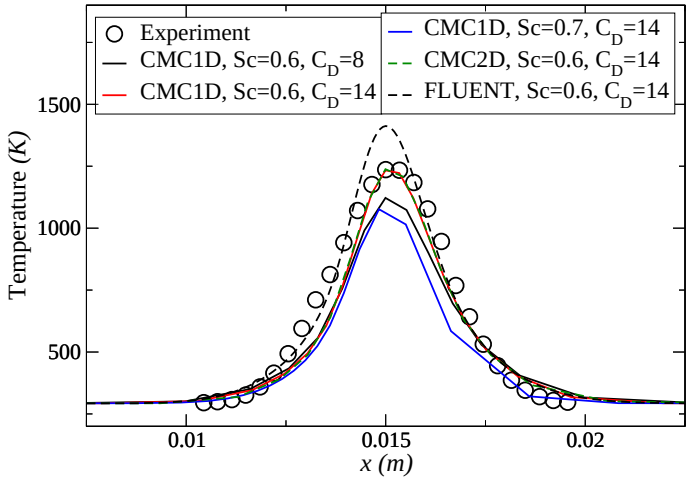

Figure 5.9: Mean temperature along the axis for Geyer et al. (2003, 2005b).

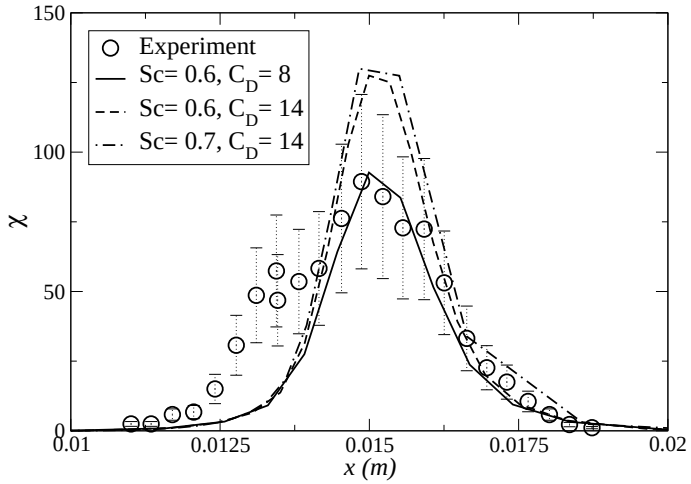

Figure 5.10: Mean scalar dissipation rate along the axis for Geyer et al. (2003, 2005b).

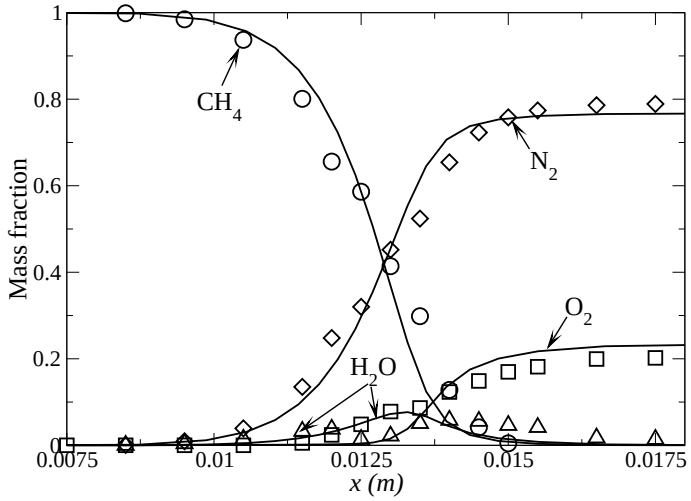

Figure 5.11: Mean mass fractions along the axis for Mastorakos (1993). $X = 0.0$ and $U_{air} = 1.48\ m/s$.

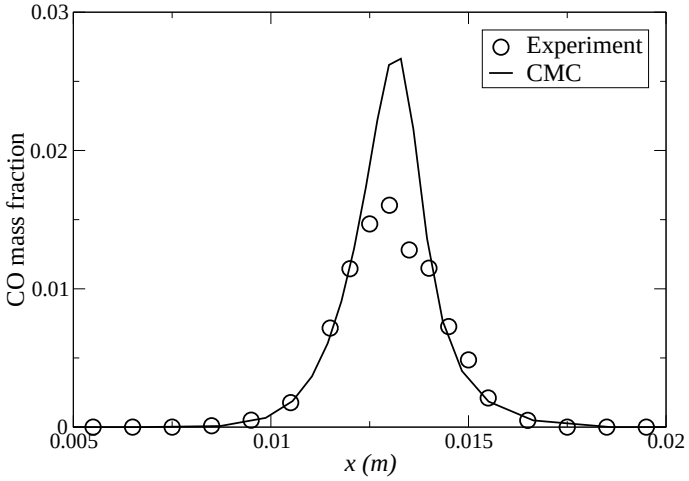

Figure 5.12: Mean CO mass fractions along the axis for Mastorakos (1993). $X = 0.0$ and $U_{air} = 1.48\ m/s$.

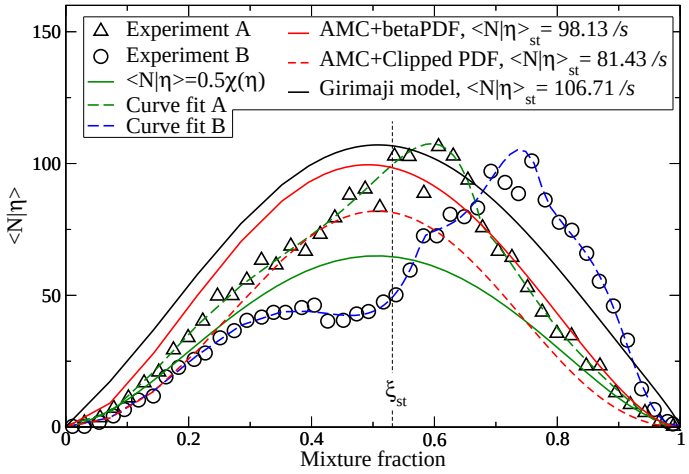

Figure 5.13: Conditional scalar dissipation rate for CMC0D. Curve fit A for Geyer et al. (2003) and curve fit B for Geyer et al. (2005b).

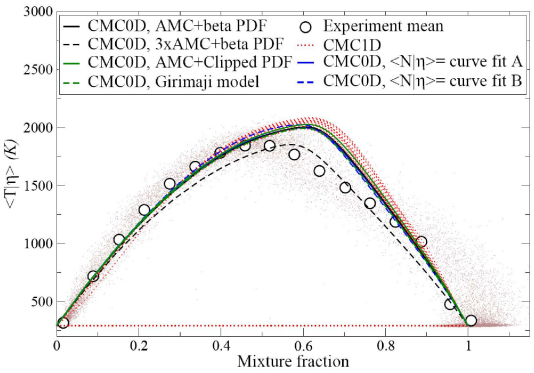

(a) Conditional mean temperature

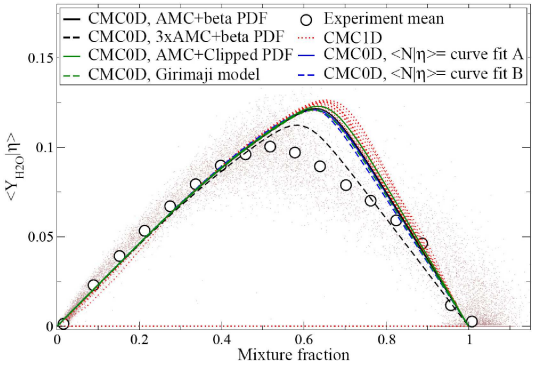

(b) Conditional mean H_2O mass fraction

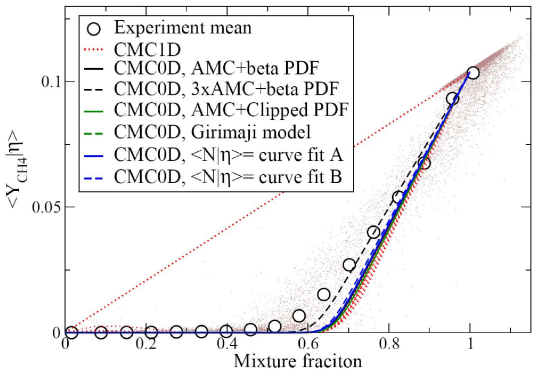

(c) Conditional mean CH_4 mass fraction

Figure 5.14: Conditional mean profiles along the axis, black dotted scatter plots are the experiment. Experimental data from Geyer et al. (2003, 2005b).

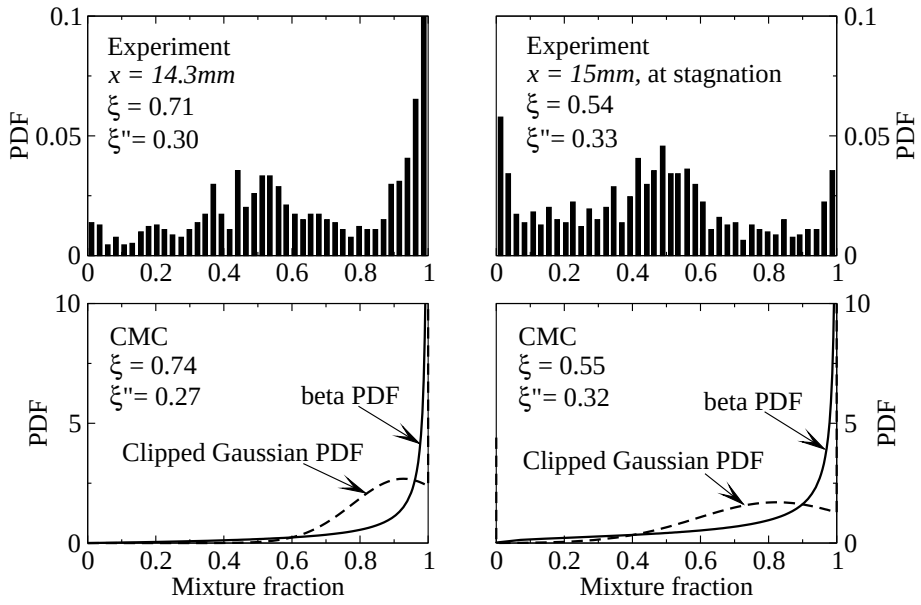

Figure 5.15: Probability density function comparison, data from Geyer et al. (2005b).

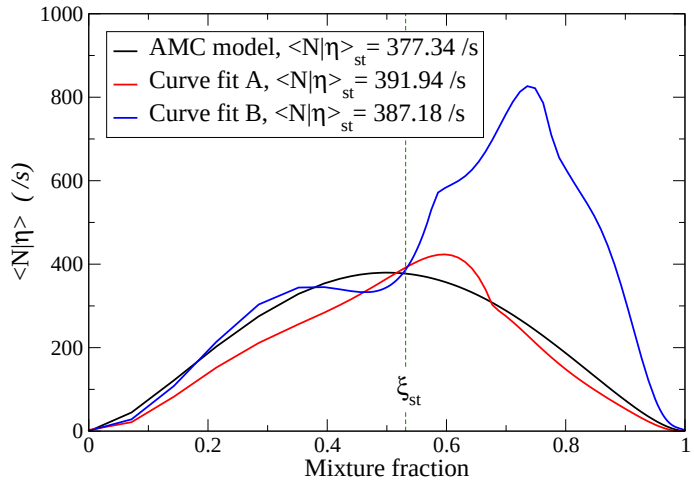

Figure 5.16: Quenching conditional scalar dissipation rate for Geyer et al. (2003) and Geyer et al. (2005a).

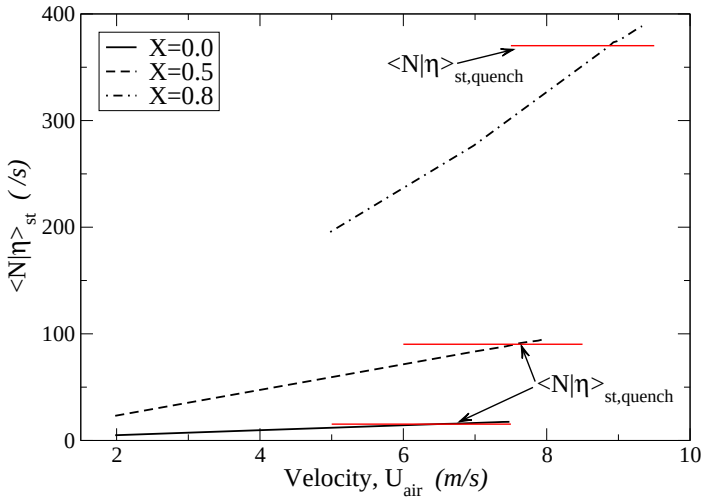

Figure 5.17: Conditional scalar dissipation rate at stoichiometry versus velocity.

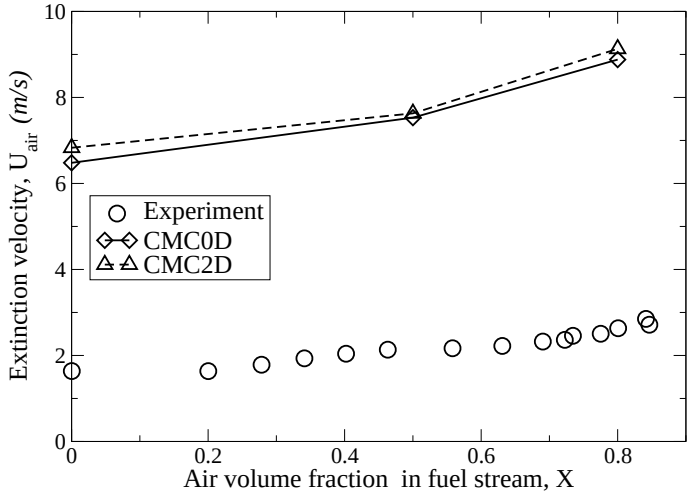

Figure 5.18: Extinction velocity versus air volume fraction in fuel stream.

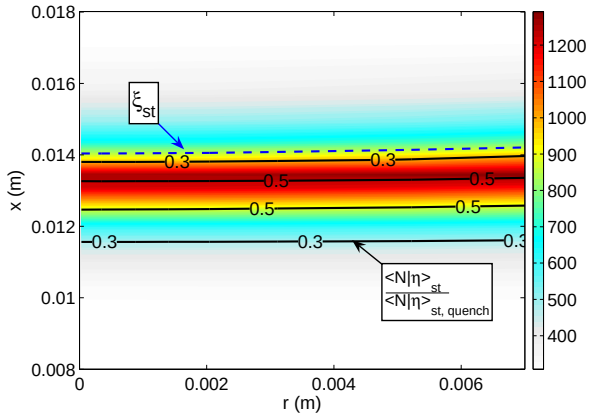

(a) $X = 0.0$ and $U_{air} = 1.98\ m/s$

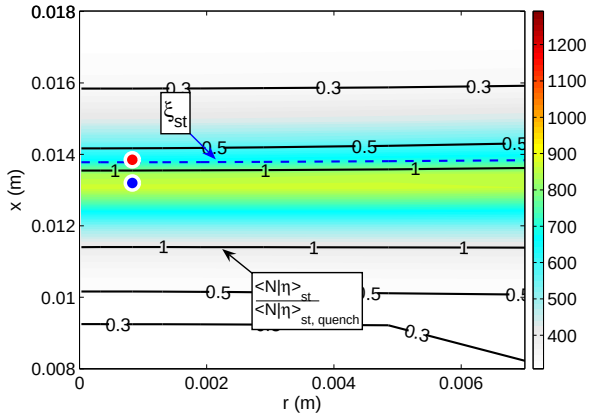

(b) $X = 0.0$ and $U_{air} = 6.48\ m/s$

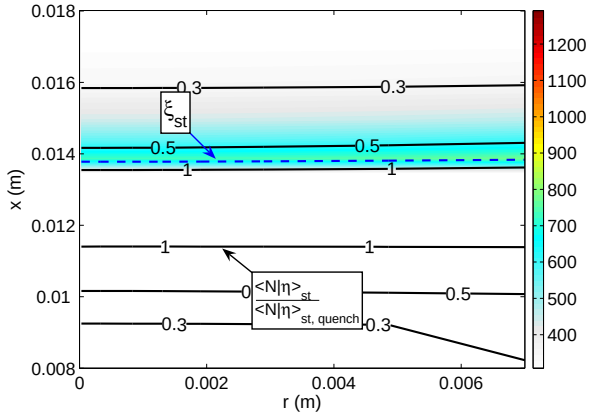

(c) $X = 0.0$ and $U_{air} = 6.48\ m/s$, no spatial terms

Figure 5.19: Mean temperature contours superimposed lines of the normalised conditional scalar dissipation rate and the stoichiometric mixture fraction at $X = 0.0$. CMC2D predicts extinction at 6.83 m/s.

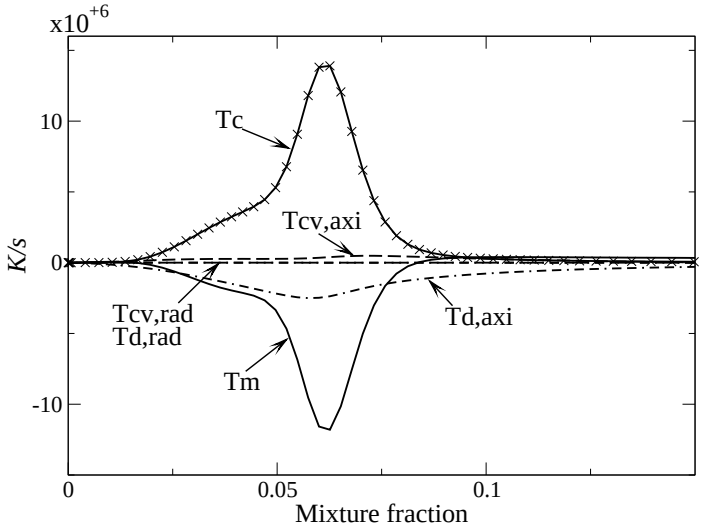

(a) Outside of the quenching zone, red dot in Figure 5.19 (b)

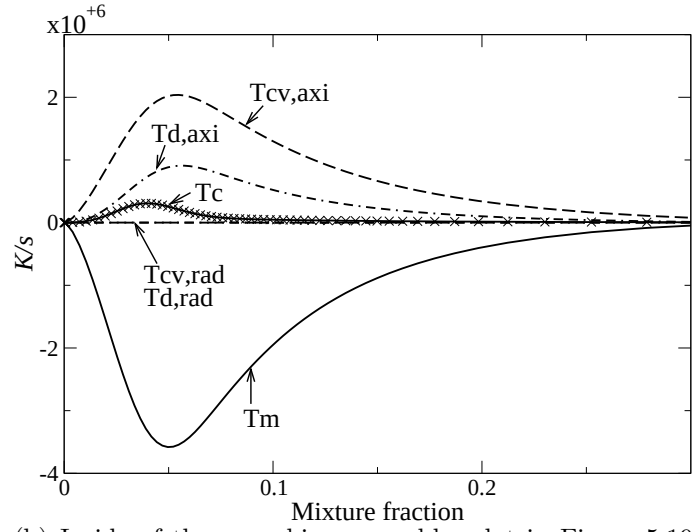

(b) Inside of the quenching zone, blue dot in Figure 5.19 (b)

Figure 5.20: The terms in the CMC equation for the conditional temperature at $X = 0.0$ and $U_{air} = 6.48\ m/s$. The corresponding locations are indicated in Figure 5.19 (b).

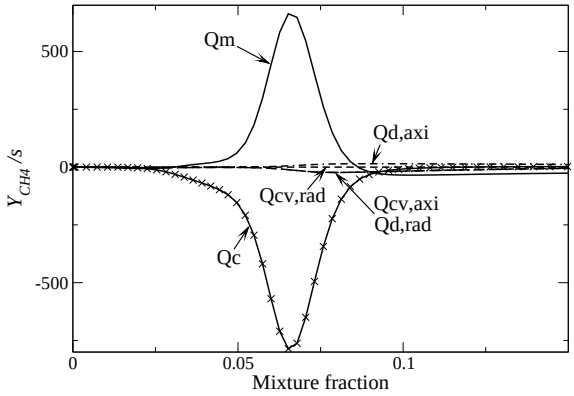

(a) Outside of the quenching zone, red dot in Figure 5.19 (b)

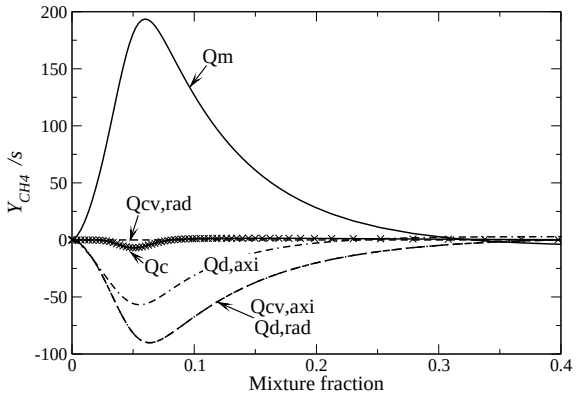

(b) Inside of the quenching zone, blue dot in Figure 5.19 (b)

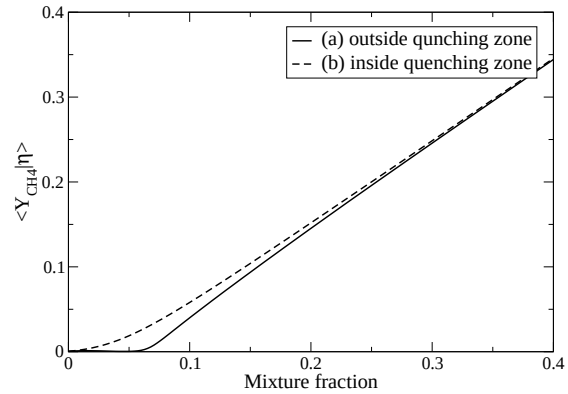

(c) Conditional mean CH_4 mass fraction for (a) and (b)

Figure 5.21: The terms in the CMC equation for the conditional species of CH_4 at $X = 0.0$ and $U_{air} = 6.48\ m/s$. The corresponding locations are indicated in Figure 5.19 (b).

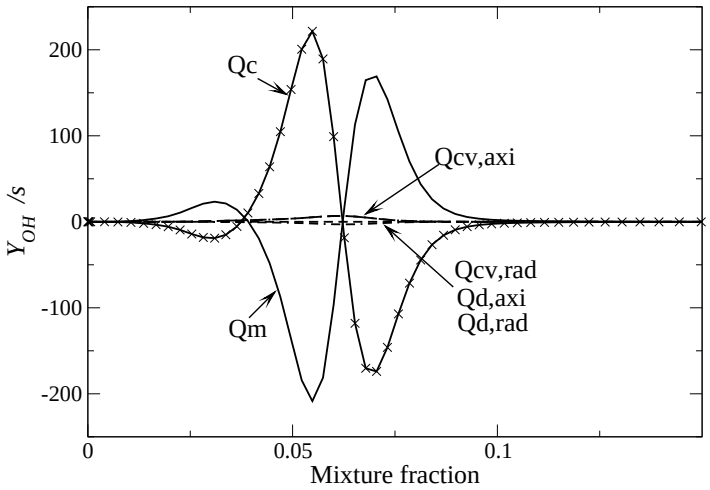

(a) Outside of the quenching zone, red dot in Figure 5.19 (b)

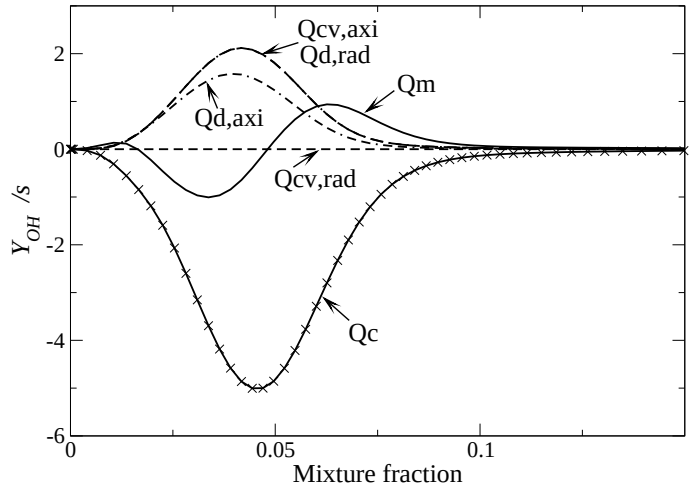

(b) Inside of the quenching zone, blue dot in Figure 5.19 (b)

Figure 5.22: The terms in the CMC equation for the conditional species of OH at $X = 0.0$ and $U_{air} = 6.48\ m/s$. The corresponding locations are indicated in Figure 5.19 (b).

Chapter 6

Conclusions

This thesis described research with the Conditional Moment Closure (CMC) model for turbulent non-premixed combustion and in particular explored the applicability of the first order CMC. The work presented in the previous Chapters contributed to two areas: the first concerns the validation and numerical implementation of CMC, described in Chapter 2, and the second concerns the applicability of the first order two-dimensional CMC in turbulent piloted diffusion jet flame involving local extinction, flame stabilisation in turbulent lifted diffusion jet flames and global extinction limits in turbulent counterflow flames, discussed in Chapter 3, 4 and 5. In the next Section, the main findings are repeated and the thesis closes with suggestions for further research.

6.1 Conclusions from this work

The first order CMC is valid when the conditional fluctuation is small. If the conditional fluctuation is large, then second order moment closure for the chemical reaction is needed.

In the validation of sub-models part, the beta PDF for the mixture fraction and the linear model for the conditional velocity have given the most accurate results compared with the DNS. The beta PDF should not apply when mixture fraction r.m.s. approaches zero and then the Clipped Gaussian PDF is used. The Girimaji model for the conditional scalar dissipation rate have given better predictions in homogeneous mixtures and the AMC model is better in inhomogeneous mixtures, when used with the beta PDF. The gradient diffusion model for the conditional fluxes has provided good agreement in the inhomogeneous case, but not in the homogenous.

Three different stiff/nonstiff ODE solvers have been presented. VODPK was chosen as the main solver for CMC in this research because it allows transformation of the PDE's into a set of ODE's which can avoid the splitting errors. Finite difference discretisation methods (UDS and CDS) in physical and mixture fraction space were examined. Numerical diffusion was large in UDS and small in CDS, however, the CDS generated unrealistic oscillations. The calculation limit by PDF proposed by Devaud and Bray (2003), seems to be too steep and cuts off a lot of information in mixture fraction space. The limit conditions of the conditional scalar dissipation rate in mixture fraction space were used on the spatial space and produce similar effect. Two methods of interfacing between the CFD grid and the CMC grid, one based on using the exact physical location of the CMC grid node and another by integrating over groups of CFD nodes and weighting by the PDF, gave very small differences.

The flow field was determined using FLUENT with a turbulence model,

the Reynolds stress model in Chapter 3 and 5 and the k–ε model in Chapter 4. Various coefficients of the turbulence model for reacting flows were modified to provide correct flow field information to CMC. The modification was made in Sc, C_D and $C_{\varepsilon 2}$ values between $0.4 \leq Sc \leq 0.7$, $1.3 \leq C_D \leq 14$ and $1.77 \leq C_{\varepsilon 2} \leq 2.02$.

A piloted natural gas jet diffusion flame was simulated with the first order two dimensional CMC in Chapter 3. A pilot was used to stabilise the flame and local extinction was observed in this experiment. We observed high scalar dissipation rate near the nozzle in the CMC calculation. The maximum temperature zone was formed along iso-contour line of mixture fraction $\xi = 0.15$, located in rich mixture side, an observation consistent with experiment.

Comparisons between the Girimaji model and AMC model for the conditional scalar dissipation rate were also presented. The two models had small differences in major species and temperature, but the intermediate species predictions showed some sensitivity, with the Girimaji model giving better prediction, especially downstream along the jet. The conditional averages of the species along and across the jet were different, which suggested that a cross-stream averaged CMC should not apply near the nozzle where conditional fluctuations are large.

The experiment shows the existence of local extinction and the CMC calculation could not reproduce this and the mean temperature was hence higher than in the experiment. However, the calculation captured the trend reasonably well. Despite the fact that two dimensional CMC showed a different approach to extinction at different points in the jet, the effect of localized

extinction were not captured.

Simulations of H_2-air turbulent lifted jet flames have been performed with two-dimensional first-order Conditional Moment Closure in Chapter 4. The computed lift-off heights and the Favre-averaged species mole fractions were found to be very close to experimental data for a wide range of jet velocities and dilutions. Simulations were also performed where the initial condition was an attached flame and the jet velocity then gradually increased to magnitudes that otherwise showed a lifted flame with downstream ignition. This did not result in lift-off, fully consistent with experimental observations, hence reproducing the hysteresis behaviour of turbulent lifted flames.

The predictions with different models for the conditional scalar dissipation rate and the presumed PDF of the mixture fraction were very similar, suggesting that this modelling aspect of CMC is not very critical for this problem.

The stabilisation mechanism was explored by quantifying the balance of terms in the 2D-CMC equation in the lift-off region. It was found that, in agreement with experimental data, the conditional scalar dissipation rate at the stabilisation height was well below the extinction value. The heat release term and the axial diffusion balanced axial convection and diffusion in mixture fraction space, with the radial components of convection and diffusion being always very small. This justifies previous approaches with a cross-stream averaged CMC. The present results suggest that first-order CMC is adequate for flame stabilisation problems.

Turbulent counterflow non-premixed and partially premixed flames have been simulated by CMC0D, CMC1D and CMC2D to study the flame structure and extinction limits in Chapter 5. An increase of C_D and a decrease of Sc resulted in a decrease of the mixture fraction r.m.s. and an increase of the scalar dissipation rate. Using high C_D, i.e. increasing the scalar dissipation rate, could capture the mean temperature profile well, however it could not capture the experimental data (Geyer et al., 2005b) in mixture fraction space. The measured scalar dissipation rate was unsymmetrical and locally peaked on the rich mixture side (Geyer et al., 2003, 2005a). The different shape of conditional scalar dissipation rate between the experiment and model gave some difference in quenching conditional scalar dissipation rate at stoichiometry.

The conditional stoichiometric scalar dissipation rate increased as the velocity increased. In CMC0D, the flame was extinguished at a critical condition and this extinction velocity was higher as the air volume fraction in the fuel stream increased, consistent with experiment. Large discrepancies in the extinction velocity were observed in CMC0D, however the trend was captured reasonably well. In simulations where the experimental conditional scalar dissipation rate was used, capturing the extinction velocity limits by CMC0D calculations was still not successful. The high sensitivity of CMC calculation to the conditional scalar dissipation rate was presented and we concluded that predicting the right conditional scalar dissipation rate was the key point to capture the extinction limits. The experimental measurement should also be more accurate.

The flame stayed alight in CMC2D calculations at the critical condition of

the CMC0D. The scalar dissipation rate must be higher than the quenching value across the the whole flame zone to extinguish the flame. The CMC2D calculations showed the same trend of the CMC0D, which implied that the importance of the spatial terms is less than the conditional scalar dissipation rate to extinguish the flame and the spatial terms were important to sustain the flame inside the quenching zone, where the flame received the heat from the outside of quenching zone. Molecular diffusion controlled the extinction in regions where $\langle N|\eta\rangle_{st} > \langle N|\eta\rangle_{st,quench}$. In the critical quenching zone, the heat was provided from outside quenching zone by axial convection and diffusion. Radial diffusion was also important to sustain the flame away from the jet axis.

The two-dimensional CMC has been used for a turbulent piloted jet, a turbulent lifted jet and turbulent counterflow flame. The applications show that the two-dimensional CMC is needed when the conditional averages have variations across the jet and the effect of spatial terms in CMC equation are strong, which are not available in CMC0D and CMC1D (especially regarding radial components).

6.2 Suggestions for further research

Concerning numerical aspects, the discretisation scheme by UDS shows large numerical diffusion. In order to reduce the numerical error, higher order of discretisation should be implemented. The grid independence of the CMC solution should be also checked. Full coupling between CMC and CFD should be made to reduce the error by not including the correct heat release in the

calculation of the flow field.

Large differences of the conditional averages of the species along and across the jet involving local extinction in Chapter 3 suggest that a cross-stream averaged CMC should not apply and hence that a higher dimensional CMC should be used.

An increase of the constant C_D value results in a decrease of the scalar dissipation rate and does not give local extinction phenomena. It seems that a higher value of C_D is needed near the nozzle in Chapter 3. In contrast, high C_D results in increasing scalar dissipation rate to extinguish the flame in Chapter 5, but discrepancies in the conditional scalar dissipation rate were found. Hence, accurate C_D for the mean scalar dissipation rate and conditional scalar dissipation rate modeling are needed to compute correctly the mixing field, especially the r.m.s. of the mixture fraction, the unconditional scalar dissipation, and the micro-mixing term in the CMC equation.

The scatter plots in Chapter 3 show the fluctuations of conditional quantities in mixture fraction, which violate the assumption of the first order CMC and hence significant differences between CMC and experiments are found. Second order moment closure method should be applied for these conditions. Doubly conditioning moment closure is also another way to reduce the fluctuation. We also did not consider differential diffusion, which could be important for the hydrogen flames (Hilbert et al., 2004) in Chapter 4. Including heat release effects on the flow field, differential diffusion and second-order/doubly conditioning closure of the chemistry source term would provide a much more complete description. It would be interesting to see the extent to which these are needed in such problems.

An effort was made in this thesis to analyse the applicability of the first order CMC in problems involving local extinction, flame stabilisation and global extinction and the work shows some success and guides further work in CMC for turbulent combustion. Such a contribution would be, I believe, welcome by combustion engineers.

Appendix A

Relationships between mass and mole fractions

Mole fraction/mass fraction:

$$\begin{aligned} X_i &= \frac{Y_i MW_{mix}}{MW_i} \\ Y_i &= \frac{X_i MW_i}{MW_{mix}} \end{aligned}$$

Molar concentration/mass fraction:

$$\begin{aligned} [X_i] &= \frac{pMW_{mix}Y_i}{R_u T MW_i} = \frac{\rho Y_i}{MW_i} \\ Y_i &= \frac{[X_i]MW_i}{\sum_j [X_j]MW_j} \end{aligned}$$

where R_u is the universal gas constant. Molar concentration/mole fraction:

$$\begin{aligned} [X_i] &= \frac{X_i p}{R_u T} = \frac{\rho X_i}{MW_{mix}} \\ X_i &= \frac{[X_i]}{\sum_j [X_j]} \end{aligned}$$

Mass concentration:

$$\rho_i = \rho Y_i = [X_i]MW_i$$

MW_{mix} defined in terms of mass fractions:

$$MW_{mix} = \frac{1}{\sum_i \frac{Y_i}{MW_i}}$$

MW_{mix} defined in terms of mole fractions:

$$MW_{mix} = \sum_i X_i MW_i$$

MW_{mix} defined in terms of molar concentrations:

$$MW_{mix} = \frac{\sum_i [X_i] MW_i}{\sum_i [X_i]}$$

Appendix B

Derivation of CMC temperature equation

Species mass fraction equation:

$$\frac{\partial\langle Y_\alpha|\eta\rangle}{\partial t}+\langle u_i|\eta\rangle\frac{\partial\langle Y_\alpha|\eta\rangle}{\partial x_i}=\langle N|\eta\rangle\frac{\partial^2\langle Y_\alpha|\eta\rangle}{\partial\eta^2}+\langle\mathcal{W}_\alpha|\eta\rangle+e_Q+e_Y \tag{B.1}$$

Enthalpy equation:

$$\frac{\partial\langle h|\eta\rangle}{\partial t}+\langle u_i|\eta\rangle\frac{\partial\langle h|\eta\rangle}{\partial x_i}=\langle N|\eta\rangle\frac{\partial^2\langle h|\eta\rangle}{\partial\eta^2}+\left\langle\frac{1}{\rho}\frac{\partial p}{\partial t}\Big|\eta\right\rangle-\langle\mathcal{W}_{RAD}|\eta\rangle+e_Q+e_Y \tag{B.2}$$

The enthalpy can be expressed as:

$$h=h(Y_\alpha,T)=\sum_{\alpha=1}^{n}\left(h_{ref,\alpha}+\int_{T_0}^{T}c_{p,\alpha}dT\right)=\sum_{\alpha=1}^{n}h_\alpha Y_\alpha \tag{B.3}$$

$$\begin{aligned}\nabla h &= \sum\nabla h_\alpha Y_\alpha+\sum h_\alpha\nabla Y_\alpha\\ &= c_p\nabla T+\sum h_\alpha\nabla Y_\alpha\end{aligned} \tag{B.4}$$

where $\nabla=\frac{\partial}{\partial x_i}$. Substitute Eq. (B.4) into Eq. (B.2) results in:

$$\left[\langle c_p|\eta\rangle\frac{\partial\langle T|\eta\rangle}{\partial t}+\sum\langle h_\alpha|\eta\rangle\frac{\partial\langle Y_\alpha|\eta\rangle}{\partial t}\right]$$
$$+\langle u_i|\eta\rangle\left[\langle c_p|\eta\rangle\frac{\partial\langle T|\eta\rangle}{\partial x_i}+\sum\langle h_\alpha|\eta\rangle\frac{\partial\langle Y_\alpha|\eta\rangle}{\partial x_i}\right]=$$
$$\langle N|\eta\rangle\frac{\partial}{\partial\eta}\left[\langle c_p|\eta\rangle\frac{\partial\langle T|\eta\rangle}{\partial\eta}+\sum\langle h_\alpha|\eta\rangle\frac{\partial\langle Y_\alpha|\eta\rangle}{\partial\eta}\right]$$
$$+\left\langle\frac{1}{\rho}\frac{\partial p}{\partial t}\Big|\eta\right\rangle-\langle\mathcal{W}_{RAD}|\eta\rangle+e_Q+e_Y \tag{B.5}$$

Eq. (B.5) is rearranged and simplified by Eq. (B.1) :

$$\langle c_p|\eta\rangle\frac{\partial\langle T|\eta\rangle}{\partial t}+\langle u_i|\eta\rangle\langle c_p|\eta\rangle\nabla\langle T|\eta\rangle$$
$$+\sum\langle h_\alpha|\eta\rangle\underbrace{\left[\frac{\partial\langle Y_\alpha|\eta\rangle}{\partial t}+\langle u_i|\eta\rangle\nabla\langle Y_\alpha|\eta\rangle\right]}_{\langle N|\eta\rangle\frac{\partial^2\langle Y_\alpha|\eta\rangle}{\partial\eta^2}+\langle\mathcal{W}_\alpha|\eta\rangle}=$$
$$\langle N|\eta\rangle\underbrace{\frac{\partial}{\partial\eta}\left[\langle c_p|\eta\rangle\frac{\partial\langle T|\eta\rangle}{\partial\eta}+\sum\langle h_\alpha|\eta\rangle\frac{\partial\langle Y_\alpha|\eta\rangle}{\partial\eta}\right]}_{\frac{\partial\langle c_p|\eta\rangle}{\partial\eta}\frac{\partial\langle T|\eta\rangle}{\partial\eta}+\langle c_p|\eta\rangle\frac{\partial^2\langle T|\eta\rangle}{\partial\eta^2}+\sum c_{p,\alpha}\frac{\partial\langle Y_\alpha|\eta\rangle}{\partial\eta}\frac{\partial\langle T|\eta\rangle}{\partial\eta}}$$
$$+\left\langle\frac{1}{\rho}\frac{\partial p}{\partial t}\Big|\eta\right\rangle-\langle\mathcal{W}_{RAD}|\eta\rangle+e_Q+e_Y \tag{B.6}$$

Eq. (B.6) can be divided by $\langle c_p|\eta\rangle$, by rearranging the terms in brackets, and by using the primary closure hypothesis in Section 2.1.3 for the e_Q and e_Y terms, the CMC temperature equation becomes:

$$\frac{\partial\langle T|\eta\rangle}{\partial t}+\langle u_i|\eta\rangle\frac{\partial\langle T|\eta\rangle}{\partial x_i}=\langle N|\eta\rangle\frac{\partial^2\langle T|\eta\rangle}{\partial\eta^2}$$
$$+\langle N|\eta\rangle\left[\frac{1}{\langle c_p|\eta\rangle}\left(\frac{\partial\langle c_p|\eta\rangle}{\partial\eta}+\sum_{\alpha=1}^{n}(c_p)_\alpha\frac{\partial\langle Y_\alpha|\eta\rangle}{\partial\eta}\right)\right]\frac{\partial\langle T|\eta\rangle}{\partial\eta}$$
$$-\frac{1}{\bar\rho\widetilde{P}(\eta)}\frac{\partial}{\partial x_i}\Big(\langle u_i''T''|\eta\rangle\bar\rho\widetilde{P}(\eta)\Big)$$
$$+\frac{1}{\langle c_p|\eta\rangle}\left\langle\frac{1}{\rho}\frac{\partial p}{\partial t}\Big|\eta\right\rangle-\frac{\langle\mathcal{W}_h|\eta\rangle}{\langle c_p|\eta\rangle}-\frac{\langle\mathcal{W}_{RAD}|\eta\rangle}{\langle c_p|\eta\rangle} \tag{B.7}$$

Appendix C

Published work

Portions of this work described in this thesis have appeared in archival literature and below, the reference for the paper is given.

1. I.S. KIM and E. Mastorakos. Simulations of turbulent lifted jet flames with two-dimensional conditional moment closure. In *Proceedings of the Combustion Institute*, Volume 30, pages 905-912. The Combustion Institute, 2005.

Paper (1) is described in Chapter 4.

Bibliography

X-S. Bai and L. Fuchs. Sensitivity study of turbulent reacting flow modeling in gas turbine combustors. *AIAA Journal*, 33(10):1857–1864, 1995.

R.S. Barlow, N.S.A. Smith, J.-Y. Chen, and R.W. Bilger. Nitric oxide formation in dilute hydrogen jet flames: Isolateion of the effects of radiation and turbulence-chemistry submodels. *Combustion and Flame*, 117:4–31, 1999.

H.A. Becker. Effects of concentration fluctuations in turbulent diffusion flames. In *Fifteenth Symposium (International) on Combustion*, volume 15, pages 601–615. The Combustion Institute, 1974.

C. Béguier, I. Dekeyser, and B.E. Launder. Ratio of scalar and velocity dissipation time scales in shear flow turbulence. *Physics of Fluids*, 3:307–310, 1978.

R.W. Bilger. Turbulent jet diffusion flames. *Progress in Energy and Combustion Science*, 1:87–109, 1976.

R.W. Bilger. Turbulent flows with non-premixed reactants. In P.A. Libby and F.A. Williams, editors, *Turbulent reacting flows*, chapter 3. Springer-Verlag, 1980.

R.W. Bilger. Turbulent diffusion flames. *Annual Review of Fluid Mechanics*, 21:101–135, 1989.

R.W. Bilger. Conditional moment closure for turbulent reacting flow. *Physics of Fluids A*, 5(2):436–444, 1993.

R.W. Bilger. The structure of turbulent nonpremixed flames. In *Twenty-Second Symposium (International) on Combustion*, volume 14, pages 475–488. The Combustion Institute, 1988.

R.W. Bilger. Future progress in turbulent combustion research. *Progress in Energy and Combustion Science*, 26:367–380, 2000.

D. Bradley, P.H. Gaskell, and X.J. Gu. The mathematical modeling of liftoff and blowoff of turbulent non-premixed methane jet flames at high strain rates. In *Twenty-Seventh Symposium (International) on Combustion*, volume 27, pages 1199–1206. The Combustion Institute, 1998.

D. Bradley, D.R. Emerson, P.H. Gaskell, and X.J. Gu. Mathematical modeling of turbulent non-premixed piloted-jet flames with local extinctions. In *Proceedings of the Combustion Institute*, volume 29, pages 2155–2162. The Combustion Institute, 2002.

K.N.C. Bray and N. Peters. Laminar flamelets in turbulent flames. In P.A. Libby and F.A. Williams, editors, *Turbulent reacting flows*, chapter 2. Academic press, 1994.

K.N.C. Bray, M. Champion, and P.A. Libby. Premixed flames in stagnating turbulence: Part I. The general formulation for counterflowing streams and gradient models for turbulent transport. *Combustion and Flame*, 84: 391–410, 1991.

K.N.C. Bray, M. Champion, and P.A. Libby. Extinction of premixed flames in turbulent counterflowing streams with unequal enthalpies. *Combustion and Flame*, 107:53–64, 1996.

G. Brethouwer. *Mixing of passive and reactive scalars in turbulent flows*. PhD thesis, Technische University Delft, 2000.

J.E. Broadwell, W.J.A. Dahm, and M.G. Mungal. Blowout of turbulent diffusion flames. In *Twentieth Symposium (International) on Combustion*, volume 20, pages 303–310. The Combustion Institute, 1984.

A. Brockhinke. Private communication, 2003.

A. Brockhinke, P. Andresen, and K. Kohse-Höinghaus. Contribution to the analysis of temporal and spatial structures near the lift-off region of a turbulent hydrogen diffusion flame. In *Twenty-Sixth Sympoisum (International) on Combusiton*, volume 26, pages 153–159. The Combustion Institute, 1996.

A. Brockhinke, S. Haufe, and K. Kohse-Höinghaus. Structural properties of lifted hydrogen jet flames measured by laser spectroscopic techniques. *Combustion and Flame*, 121:367–377, 2000.

J. Buckmaster. Edge-flames. *Progress in Energy and Combustion Science*, 28:435–375, 2002.

S.P. Burke and T.E. Schumann. Diffusion flames. *Industrial and Engineering Chemistry*, 20:998–1004, 1928.

G.D. Byrne. Pragmatic experiments with Krylov methods in the stiff ODE setting. In J. Cash and I. Gladwell, editors, *Computational Ordinary Differential Equations*, pages 323–356. Oxford University Press, Oxford, 1992.

R.S. Cant. FERGUS. Technical report, Engineering Department, University of Cambridge, 2002.

C.M. Cha and H. Pitsch. Higher-order conditional moment closure modelling of local extinction and reignition in turbulent combustion. *Combustion Theory and Modelling*, 6:425–437, 2002.

M. Chen, M. Herrmann, and N. Peters. Flamelet modeling of lifted turbulent methane/air and propane/air jet diffusion flames. In *Proceedings of the Combustion Institute*, volume 28, pages 167–174. The Combustion Institute, 2000.

Y. Chen, C. Chang, K. Pan, and J. Yang. Flame lift-off and stabilization mechanisms of nonpremixed jet flames on a bluff-body burner. *Combustion and Flame*, 115:51–65, 1998.

T.S. Cheng, J.A. Wehrmeyer, and R.W. Pitz. Simultaneous temperature and multispecies measurement in a lifted hydrogen diffusion flame. *Combustion and Flame*, 91:323–345, 1992.

C.-P. Chou, J.-Y. Chen, J. Janicka, and E. Mastorakos. Modeling of turbulent opposed-jet mixing flows with $\tilde{k}$-$\tilde{\varepsilon}$ model and second-order closure. *International Journal of Heat and Mass Transfer*, 47:1023–1035, 2004.

M.J. Cleary and J.H Kent. A numerical method for conditional moment closure. In *2003 Australian Symposium on Combustion and The 8th Australian Flames Days*, 2003.

P.J. Colucci, F.A. Jaberi, P. Givi, and S.B. Pope. Filtered density function for large eddy simulation of turbulent reacting flows. *Physics of Fluids*, 10 (2):499–515, 1998.

C.B. Devaud and K.N.C. Bray. Assessment of the applicability of conditional moment closure to a lifted turbulent flame: first order model. *Combustion and Flame*, 132:102–114, 2003.

C.B. Devaud, J.H. Kent, and R.W. Bilger. Conditional moment closure applied to a lifted turbulent methane-air flame. In *The third Mediterranean Combustion Symposium*. Marrakech, Morocco, June 2003.

C.B. Devaud, R.W. Bilger, and T. Liu. A new method of modeling the conditional scalar dissipation rate. *Physics of Fluids*, 16:2004–2011, 2004.

P. Domingo and L. Vervisch. Triple flames and partially premixed combustion in autoignition of non-premixed turbulent mixtures. In *Twenty-Sixth Symposium (International) on Combustion*, volume 26, pages 233–240. The Combustion Institute, 1996.

P. Domingo, L. Vervisch, and K. Bray. Partially premixed flamelets in les of nonpremixed turbulent combustion. *Combustion Theory Modelling*, 6: 529–551, 2002.

J. Eckstein, J.-Y. Chen, C.-P. Chou, and J. Janicka. Modeling of turbulent mixing in opposed jet configuration: One − dimensional Monte Carlo probability density fuction simulation. In *Proceedings of the Combustion Institute*, volume 28, pages 114–148. The Combustion Institute, 2000.

H. Eickhoff, B. Lenze, and W. Leuckel. Experimental investigation on the stabilization mechanism of jet diffusion flames. In *Twentieth Symposium (International) on Combustion*, volume 20, pages 311–318. The Combustion Institute, 1984.

I. Esquiva-Dano, H.T. Nguyen, and D. Escudie. Influence of a bluff-body's shape on the stabilization regime of non-premixed flames. *Combustion and Flame*, 127:2167–2180, 2001.

V. Eswaran and S.B. Pope. Direct numerical simulations of the turbulent mixing of a passive scalar. *Physics of Fluids*, 31(3):506–520, 1988.

M. Fairweather and R.M. Woolley. First-order conditional moment closure modeling of turbulent, nonpremixed hydrogen flames. *Combustion and Flame*, 133:393–405, 2003.

S.J. Farlow. *Partial differential equations for scientists and engineers*. Dover publications, INC., 1993.

A. Favre. *Statistical equations of turbulent gases*. Problems of hydrodynamics and continuum mechanics, SIAM Philadelphia, 1969.

FLUENT. FLUENT V*6*. FLUENT Inc., http://www.fluent.com, 2003.

J.H. Frank, P.A.M Kalt, and R.W. Bilger. Measurements of conditional velocities in turbulent premixed flames by simultaneous OH PLIF and PIV. *Combustion and Flame*, 116:220–232, 1999.

C.E. Frouzakis, A.G. Tomboulides, J. Lee, and K. Boulouchos. From diffusion to premixed flames in an H_2/air opposed-jet burner: The role of edge flames. *Combustion and Flame*, 130:171–184, 2002.

D. Geyer, A. Dreizler, A. Kempf, Sadiki A., and J. Janicka. Finete chmistry effects in a turbulent opposed-jet burner: 1D − Raman/Rayleigh measurements and large eddy simulations. In *Proceedings of the European Combustion Meeting 2003*, 2003.

D. Geyer, A. Dreizler, and J. Janicka. Scalar dissipation rate in isothermal and reactive turbulent opposed-jets: 1D − Raman/Rayleigh experiments supported by LES. In *Proceedings of the Combustion Institute*, volume 30, page to appear. The Combustion Institute, 2005a.

D. Geyer, A. Dreizler, J. Janicka, Permana A.D., and J.Y. Chen. Finite rate chemistry effects in turbulent opposed flows: Comparison of Raman/Rayeigh measurements and Monte Carlo PDF simulation. In *Proceedings of the Combustion Institute*, volume 30, page to appear. The Combustion Institute, 2005b.

S. Ghoasl and L. Vervisch. Stability diagram for lift-off and blowout of a round jet laminar diffusion flame. *Combustion and Flame*, 123:646–655, 2001.

S.S. Girimaji. On the modeling of scalar diffusion in isotropic turbulence. *Physics of Fluids A*, 4(11):2529–2537, 1992.

S.S. Girimaji. Assumed β-pdf model for turbulent mixing: Vadation and extension to multiple scalar mixing. *Combustion Science and Technology*, 78:177–196, 1991.

P.J. Goix and L. Talbot. Turbulent counterflow diffusion flame structure and dilution effects. *Combustion Science and Technology*, 79:175–194, 1991.

D. Han and M.G. Mungal. Stabilization in turbulent lifted deflected-jet flames. In *Proceedings of the Combustion Institute*, volume 29, pages 1889–1895. The Combustion Institute, 2002.

E.F. Hasselbrink and M.G. Mungal. Characteristics of the velocity field near the instantaneous base of lifted non-premixed turbulent jet flames. In

Twenty-Seventh Symposium (International) on Combustion, volume 27, pages 867–873. The Combustion Institute, 1998.

G-W. He and R. Rubinstein. The mapping closure approximation to the conditional dissipaiton rate for turbulent scalar mixing. *Journal of Turbulence*, 4(029), November 2003.

R. Hilbert, F. Tap, H. El-Rabii, and D. Thévenin. Impact of detailed chemistry and transport models on turbulent combustion simulations. *Progress in Energy and Combustion Science*, 30:61–117, 2004.

A.C. Hindmarsh. ODEPACK, A systematized collection of ODE solvers. In R. S. Stepleman, editor, *Scientific Computing*, pages 55–64. North-Holland, Amsterdam, 1983.

J.O. Hinze. *Turbulence*. McGraw-hill, 2nd edition, 1987.

J. Janicka and N. Peters. Prediction of trubulent jet diffusion flame lift-off using a PDF transport equation. In *Nineteenth Symposium (International) on Combustion*, volume 19, pages 367–374. The Combustion Institute, 1982.

W. Jones and J. Whitelaw. Modelling and measurement in turbulent combustion. *Progress in Energy and Combustion Science*, 20:233, 1985.

W.P. Jones and B.E. Launder. The prediction of laminarisation with a two-equation turbulence model. *International Journal of Heat and Mass Transfer*, 15:301, 1972.

R.J. Kee, F.M. Rupley, and J.A. Miller. Chemkin-II: A Fortran chemical kinetics package for the analysis of gas-phase chemical kinetics. Sandia report sand89-8009.uc-401, Sandia, 1989.

J.H. Kent and R.W. Bilger. Turbulent diffusion flames. In *Fourteenth Symposium (International) on Combustion*, volume 14, pages 615–625. The Combustion Institute, 1973.

I.S. Kim and E. Mastorakos. Simulations of turbulent lifted jet flames with two-dimensional conditional moment closure. In *Proceedings of the Combustion Institute*, volume 30, pages 905–912. The Combustion Institute, 2005.

S.H. Kim and K.Y. Huh. Use of the conditional moment closure model to predict NO formation in a turbulent CH_4/H_2 flame over a bluff-body. *Combustion and Flame*, 130:94–110, 2002a.

S.H. Kim and K.Y. Huh. Second-order conditional moment closure modeling of turbulent piloted jet diffusion flames. *Combustion and Flame*, 138:336–352, 2004.

S.H. Kim, K.Y. Huh, and R.A. Fraser. Modeling autoignition of a turbulent methane jet by the conditional moment closure model. In *Proceedings of the Combustion Institute*, volume 28, pages 185–191. The Combustion Institute, 2000a.

S.H. Kim, K.Y. Huh, and L. Tao. Application of the elliptic conditional moment closure model to a two-dimensional nonpremixed methanol bluff-body flame. *Combustion and Flame*, 120:75–90, 2000b.

W.T. Kim and K.Y. Huh. Numerical simulation of spray autoignition by the first order conditional moment closure model. In *Proceedings of the Combustion Institute*, volume 29, pages 569–576. The Combustion Institute, 2002b.

A. Kitajima, T. Ueda, A. Matsuo, and M. Mizomoto. Experimental investigatioin of the flame structure and extinction of turbulent counterflow non-premixed flames. In *Twenty-Sixth Sympoisum (International) on Combusiton*, volume 26, pages 137–143. The Combustion Institute, 1996.

A. Kitajima, T. Ueda, A. Matsuo, and M. Mizomoto. A comprehensive examination of the structure and extinction of turbulent nonpremixed flames formed in a counterflow. *Combustion and Flame*, 121:301–311, 2000.

A.Y. Klimenko. Multicomponent diffusion of various admixtures in turbulent flow. *Fluid Dynamics*, 25:327–334, 1990.

A.Y. Klimenko. On the relation between the conditional moment closure and unsteady flamelets. *Combustion Theory Modelling*, 5(275-294), 2001.

A.Y. Klimenko and R.W. Bilger. Conditional moment closure for turbulent combustion. *Progress in Energy and Combustion Science*, 25:595–687, 1999.

L.W. Kostiuk, K.N.C. Bray, and T.C. Chew. Premixed turbulent combustion in counterflowing streams. *Combustion Science and Technology*, 64:233–241, 1989.

L.W. Kostiuk, K.N.C. Bray, and R.K. Cheng. Experimental study of premixed turbulent combustion in opposed streams. Part I - nonreacting flow field. *Combustion and Flame*, 92:377–395, 1993a.

L.W. Kostiuk, K.N.C. Bray, and R.K. Cheng. Experimental study of premixed turbulent combustion in opposed streams. Part II - reacting flow field and extinction. *Combustion and Flame*, 92:396–409, 1993b.

L.W. Kostiuk, K.N.C. Bray, and R.K. Cheng. Experimental study of premixed turbulent combustion in opposed streams. Part III - spatial structure of flames. *Combustion and Flame*, 118:129–139, 1999.

A. Kronenburg. Double conditioning of reactive scalar transport equaitons in turbulen nonpremixed flames. *Physics of Fluids*, 16(7):2640–2648, 2004.

K.K. Kuo. *Principles of combustion*. Wiley-interscience, 1986.

B.E. Launder, G.J. Reece, and W. Rodi. Progress in the development of a reynolds stress turbulence closure. *Journal of Fluid Mechanics*, 68:269–289, 1975.

J.D. Li and R.W. Bilger. Measurement and prediction of the conditional variance in a turbulent reactive-scalar mixing layer. *Physics of Fluids A*, 5(12):3255–3264, December 1993.

F. Liu, H. Guo, G.J. Smallwood, Ö.L. Gülder, and M.D. Matovic. A robust and accurate algorithm of the β-pdf integration and its application to turbulent methane-air diffusion combustion in a gas turbine combustor simulator. *International Journal of Thermal Sciences*, 41:763–772, 2002.

F.C. Lockwood and A.S. Naguib. The prediction of the fluctuations in the properties of free, round-jet, turbulent, diffusion flames. *Combustion and Flame*, 24:109–124, 1975.

A.J. Lowe, E. Mastorakos, and R.S. Cant. The Direct Numerical Simulation of auto-ignition in three-dimensional freely decaying turbulence. Technical report, Engineering Department, University of Cambridge, May 2002.

B.F. Magnussen and B.H. Hjertager. On mathematical models of turbulent combustion with special emphasis on soot formation and combustion. In *Sixteenth Symposium (International) on Combustion*, volume 16, pages 719–729. The Combustion Institute, 1977.

E. Mastorakos. *Turbulent combustion in opposed jet flows*. Ph.d. thesis, Imperial College, University of London, 1993.

E. Mastorakos and W. Bilger. Boundary conditions at walls for conditional moment closure modeling. Unpublished, July 2001.

E. Mastorakos and Y.M. Wright. Simulations of turbulent spray auto-ignition with elliptic conditional moment closure. In *Proceedings of the European Combustion Meeting*, 2003.

E. Mastorakos, A.M.K.P. Taylor, and J.H. Whitelaw. Extinction and temperature characteristics of turbulent counterflow diffusion flames with partial premixing. *Combustion and Flame*, 91:40–54, 1992a.

E. Mastorakos, A.M.K.P. Taylor, and J.H. Whitelaw. Scalar dissipation rate at the extinction of turbulent counterflow nonpremixed flames. *Combustion and Flame*, 91:55–64, 1992b.

F.A. Maury and P.A. Libby. Nonpremixed flames in stagnating turbulence part i - the $\widetilde{k}-\widetilde{\varepsilon}$ theory with equilibrium chemistry for the methane-air system. *Combustion and Flame*, 102:341–356, 1995.

W.E. Mell, V. Nilsen, G. Kosály, and J.J. Riley. Investigation of closure models for nonpremixed turbulent reacting flows. *Physics of Fluids*, 6: 1331–1356, 1994.

R.C. Miake-Lye and J.A. Hammer. Lifted turbulent jet flames: A stability criterion based on the jet large-scale structure. In *Twenty-Second Symposium (International) on Combustion*, volume 22, pages 817–824. The Combustion Institute, 1988.

Y. Mizobuchi, S. Tachibana, J. Shinio, S. Ogawa, and T. Takeno. A numerical analysis of the structure of a turbulent hydrogen jet lifted flame. In *Proceedings of the Combustion Institute*, volume 29, pages 2009–2015. The Combustion Institute, 2002.

D.R. Mott and B. Oran, E.S.and van Leer. A quasi-steady-state solver for the stiff ordinary differential equations of reaction kinetics. *Journal of Computational Physics*, 164:407–428, 2000.

C. Mounaïm-Rousselle and I. Gökalp. Strain effects on the structure of counterflowing turbulent premixed flames. In *Twenty-Fifth Sympoisum (International) on Combusiton*, volume 25, pages 1199–1205. The Combustion Institute, 1994.

L. Muñiz and M.G. Mungal. Instantaneous flame-stabilization velocities in lifted-jet diffusion flames. *Combustion and Flame*, 111:16–31, 1997.

C.M. Müller, H. Breitbach, and N. Peters. Partially premixed turbulent flame propagation in jet flames. In *Twenty-Fifth Symposium (International) on Combustion*, volume 25, pages 1099–1106. The Combustion Institute, 1994.

P.A. Nooren, M. Versluis, T.H. van der Meer, R.S. Barlow, and J.H. Frank. Raman – Rayleigh – LIF measurements of temperature and species concentrations in the Delft piloted turbulent jet diffusion flame. *Applied Physics B*, 71:95–111, 2000.

E.E. O'Brien and T. Jiang. The conditional dissipation rate of an initially binary scalar in homogeneous turbulence. *Physics of Fluids A*, 3(12):3121–3123, December 1991.

S.K. Omar, D. Geyer, A. Dreizler, and J. Janicka. Investigation of flame structures in turbulent partially premixed counter-flow flames using planner laser-induced fluorescence. *Progress in Computational Fluid Dynamics*, 4:241–249, 2004.

N. Peters. Laminar diffusion flamelet models in non-premixed turbulent combustion. *Progress in Energy and Combustion Science*, 10:319–339, 1984a.

N. Peters. Laminar flamelet concepts in turbulent combustion. In *Twenty-First Symposium (International) on Combustion*, pages 1231–1250. The Combustion Institute, 1986.

N. Peters. Partially premixed diffusion flamelets in non-premixed turbulent combustion. In *Twentieth Symposium (International) on Combustion*, volume 20, pages 353–360. The Combustion Institute, 1984b.

N. Peters. *Turbulent combustion*. Cambridge University Press, 2000.

N. Peters and F.A. Williams. Liftoff characteristics of turbulent jet diffusion flames. *AIAA*, 21(3):423–429, March 1983.

W.M. Pitts. Assessment of theories for the behavior and blowout of lifted turbulent jet diffusion flame. In *Twenty-Second Symposium (International) on Combustion*, volume 27, pages 809–816. The Combustion Institute, 1988.

S.B. Pope. PDF methods for turbulent reactive flows. *Progress in Energy and Combustion Science*, 11:119–192, 1985.

S.B. Pope. *Turbulent flows*. Cambridge University Press, 2000.

E. Richardson. Implementatioin of CHEMEQ2 for various turbulent combustion simulations. Internal report, Department of Engineering, Univeristy of Cambridge, September 2004.

L.F. Richardson. *Weather prediction by numerical process*. Cambridge University Press, 1922.

M.R. Roomina and R.W. Bilger. Conditional moment closure (CMC) predictions of a turbulent methane-air jet flame. *Combustion and Flame*, 125: 1176–1175, 2001.

Ö. Savas and S.R. Gollahalli. Flow structure in near-nozzle region of gas jet flames. *AIAA*, 24(7):1137–1140, July 1986.

R.W. Schefer and P.J. Goix. Mechanism of flame stabilization in turbulent, lifted-jet flames. *Combuation and Flames*, 112:559–574, 1998.

R.W. Schefer, M. Namazian, E.E.J. Filtopoulos, and J. Kelly. Temporal evolution of turbulent/chemistry interations in lifted, turbulent-jet flames. In *Twenty-Fifth Symposium (International) on Combustion*, volume 25, pages 1223–1231. The Combustion Institute, 1994a.

R.W. Schefer, M. Namazian, and J. Kelly. Stabilization of lifted turbulent-jet flames. *Combustion and Flame*, 99:75–86, 1994b.

G.P. Smith, D.M. Golden, M. Frenklach, N.W. Moriarty, B. Eiteneer, M. Goldenberg, C. T. Bowman, R.K. Hanson, S. Song, W.C. Gardiner, Jr, V.V. Lissianski, and Z. Qin. GRI − Mech 3.0, 1999.

N.S.A. Smith, R.W. Bilger, and J.Y. Chen. Modelling of nonpremixed hydrogen jet flames using a conditional moment closure method. In *Twenty-Fourth Symposium (International) on Combustion*, volume 29, pages 263–269. The Combustion Institute, 1992.

N.S.A. Smith, R.W. Bilger, C.D. Carter, R.S. Barlow, and J.Y. Chen. A comparison of CMC and PDF modelling predictions with experimental nitric oxide LIF/Raman measurements in a turbulent H_2 jet flame. *Combustion Science and Technology*, 105:357–375, 1995.

M.D. Smooke, I.K. Puri, and K. Seshadri. A comparison between numerical calculations and experimental measurement of the structure of a counterflow diffuison flame burning diluted methane in diluted air. In *Twenty-First Symposium (International) on Combustion*, volume 21, pages 1783–1792. The Combustion Institite, 1986.

D.B. Spalding. *Combuston and mass transfer*. Oxford, 1979.

D.B. Spalding. Mixing and chemical reaction in steady confined turbulent flames. In *Thirteenth Symposium (International) on Combustion*, volume 13, pages 649–657. The Combustion Institute, 1971.

C.G. Speziale, S. Sarkar, and T.G. Gatski. Modelling the pressure-strain correlation of turbulence: an invariant dynamical systems approach. *Journal of Fluid Mechanics*, 227:245–272, 1991.

H. Stapountzis, B.L. Sawford, J.C.R. Hunt, and R.E. Britter. Structure of the temperature field downwind of a line source in grid turbulence. *Journal of Fluid Mechanics*, 165:401–424, 1986.

N. Swaminathan and R.W. Bilger. Assessment of combustion submodels for turbulent nonpremixed hydrocarbon flames. *Combustion and Flame*, 116: 519–545, 1999.

N. Swaminathan and R.W. Bilger. Analyses of conditional moment closure for turbulent premixed flames. *Combustion Theory Modelling*, 5:241–260, 2001.

M.M. Tacke, D. Geyer, E.P. Hassel, and J. Janicka. A detailed investigation of the stabilization point of lifted turbulent diffustion flames. In *Twenty-Seventh Symposium (International) on Combustion*, volume 27, pages 1157–1165. The Combustion Institute, 1998.

Tennekes and Lumley. *A first course in turbulence*. The MIT press, 1972.

S.R. Turns. *An introduction to combustion*. McGraw Hill, 2nd edition, 2000.

L. Vanquickenborn and A. van Tiggelen. The stabilization mechanism of lifted diffusion flames. *Combustion and Flame*, 10:59–69, 1966.

L. Vervisch. Using numerics to help the understanding of non-premixed turbulent flames. In *Proceedings of the Combustion Institute*, volume 28, pages 11–24. The Combustion Institute, 2000.

D Veynante and L. Vervisch. Turbulent combustion modeling. *Progress in Energy and Combustion Science*, 28:193–266, 2002.

J. Warnatz, U. Maas, and R.W. Dibble. *Combustion*. Springer, 3rd edition, 2001.

F.A. Williams. *Combustion theory*. Benjamin/Cummings, 2nd edition, 1985.

H. Yamashita, M. Shimada, and T. Takeno. A numerical study on flame stability at the transition point of jet diffusion flames. In *Twenty-Sixth Symposium (International) on Combustion*, volume 26, pages 27–34. The Combustion Institute, 1996.